Cold and Ultra-cold Molecules

Sadiq Rangwala

Raman Research Institute
Bangalore, India

Hydrogen Atom Energy Level Diagram
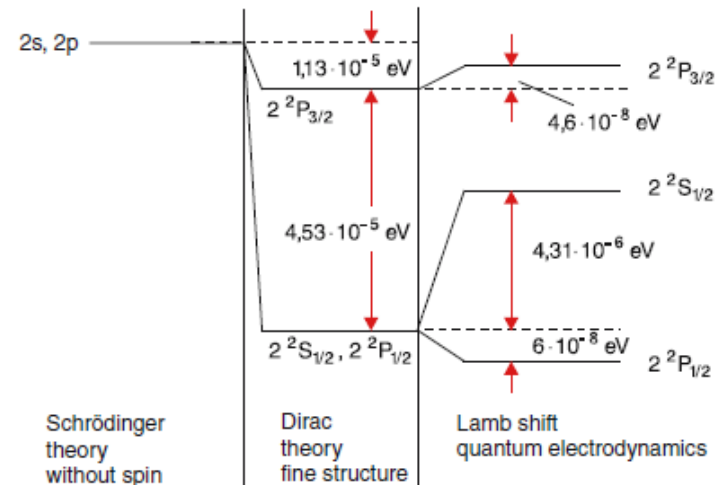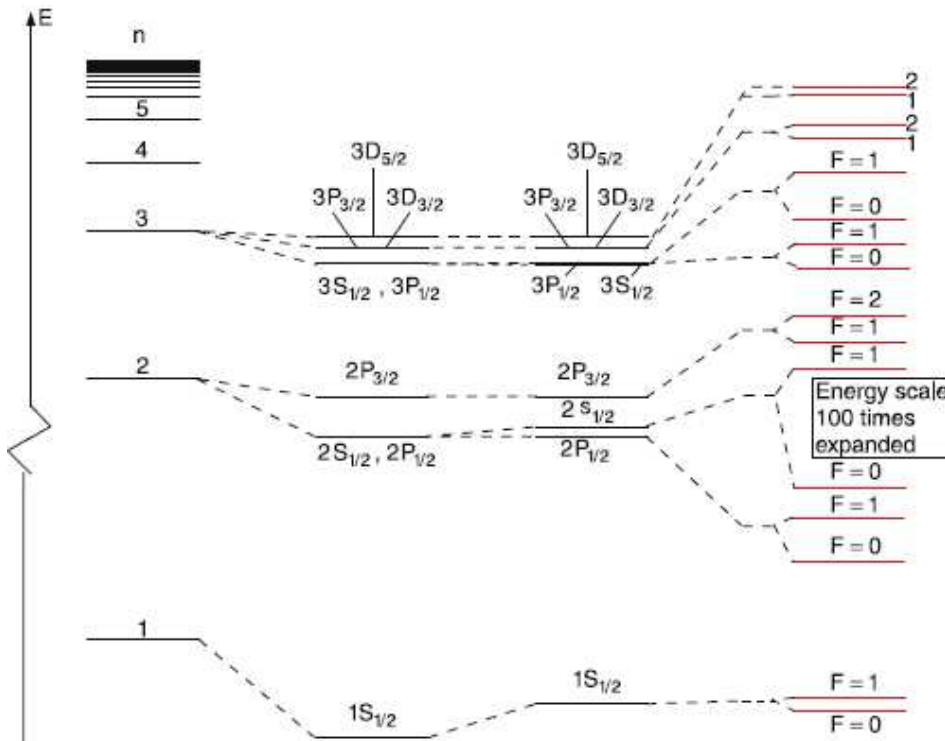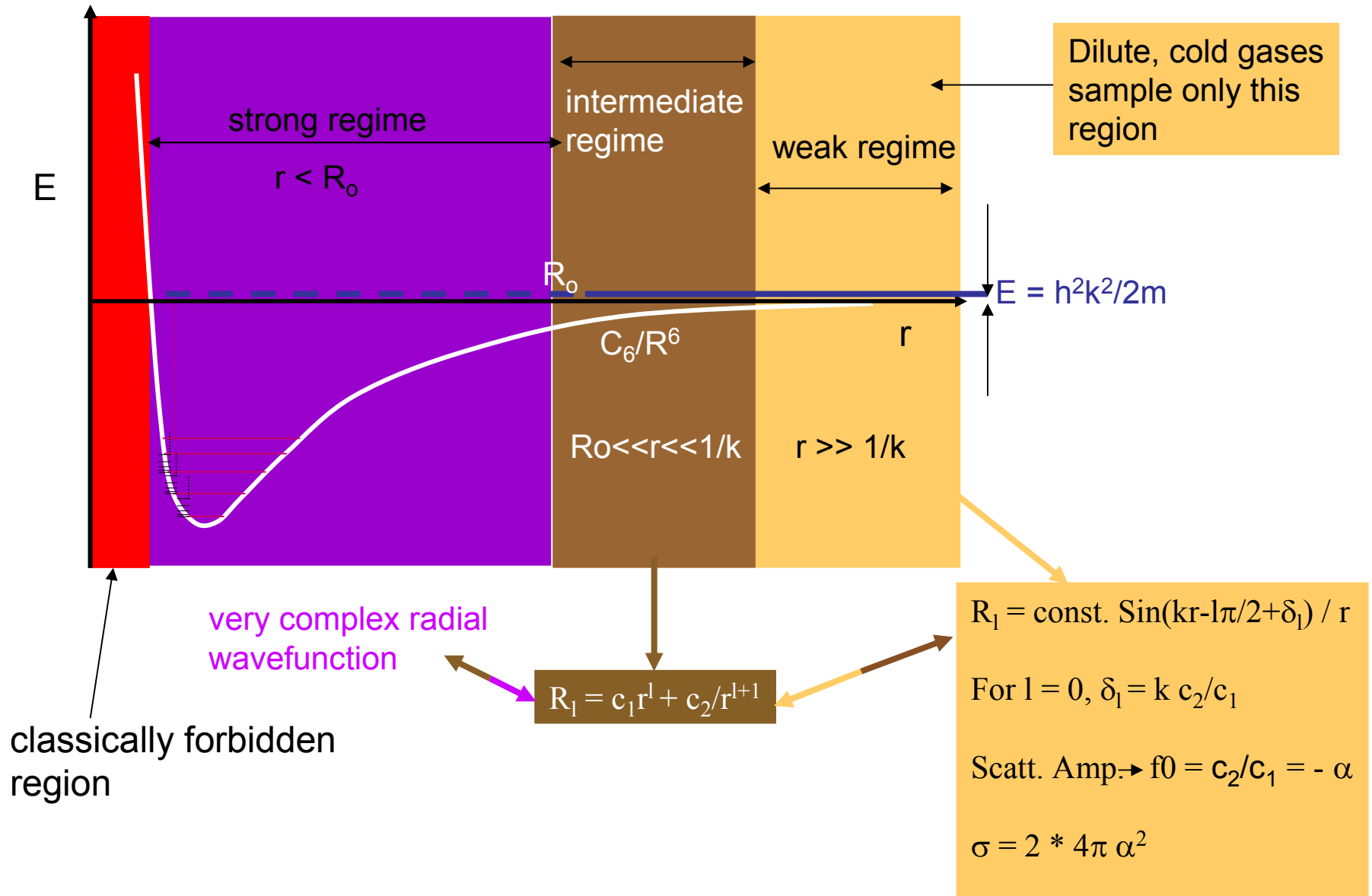

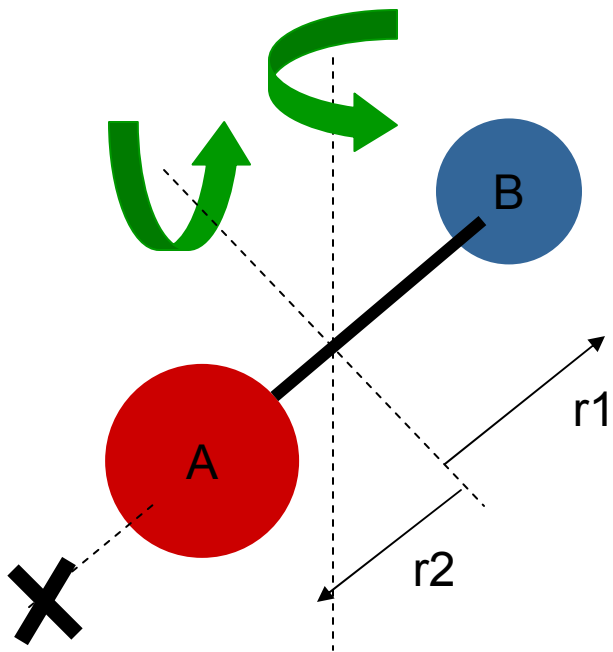Fig. 5.34. Fine structure and Lamb shift of the $n = 2$ level of the H atom

Demtröder
Atoms, Molecules and Photons

Introduction to the Diatomic Molecule

E

strong regime

$r < R_o$

intermediate regime

weak regime

Dilute, cold gases sample only this region

R_o

$E = h^2k^2/2m$

C_6/R^6

r

$R_o \ll r \ll 1/k$

$r \gg 1/k$

very complex radial wavefunction

classically forbidden region

$R_l = c_1 r^l + c_2/r^{l+1}$

$R_l = const. \; Sin(kr - l\pi/2 + \delta_l) \, / \, r$

For $l = 0$, $\delta_l = k \, c_2/c_1$

Scatt. Amp. $\rightarrow f0 = c_2/c_1 = -\alpha$

$\sigma = 2 * 4\pi \, \alpha^2$

Introducing the molecule (I)

Rotation

Vibration
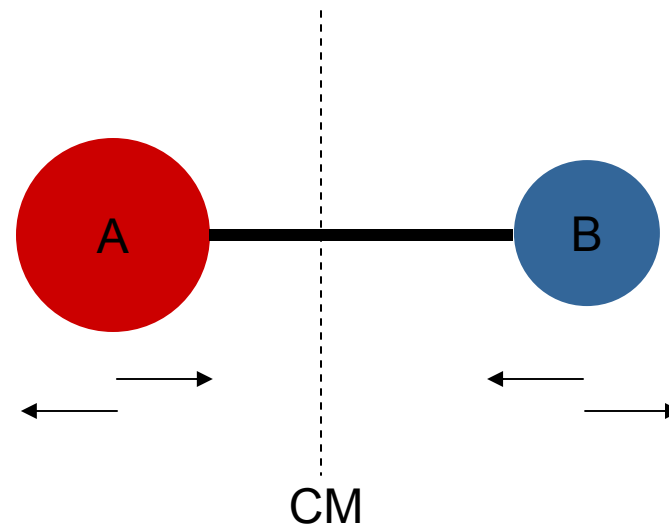
Introducing the molecule (II)

Electronic Energy Levels

Anti-bonding

Bonding
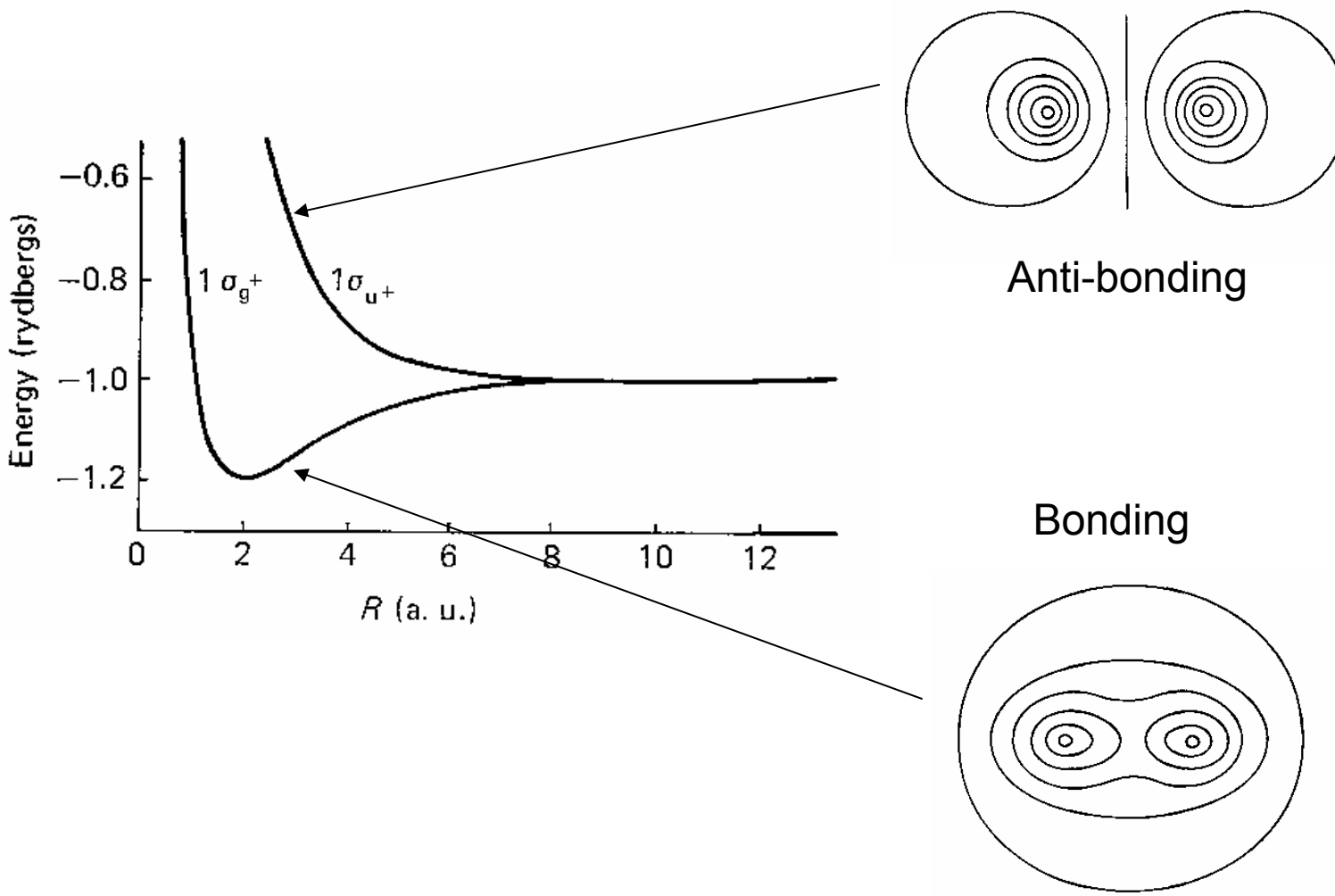
Single Photon Transitions in Molecules I
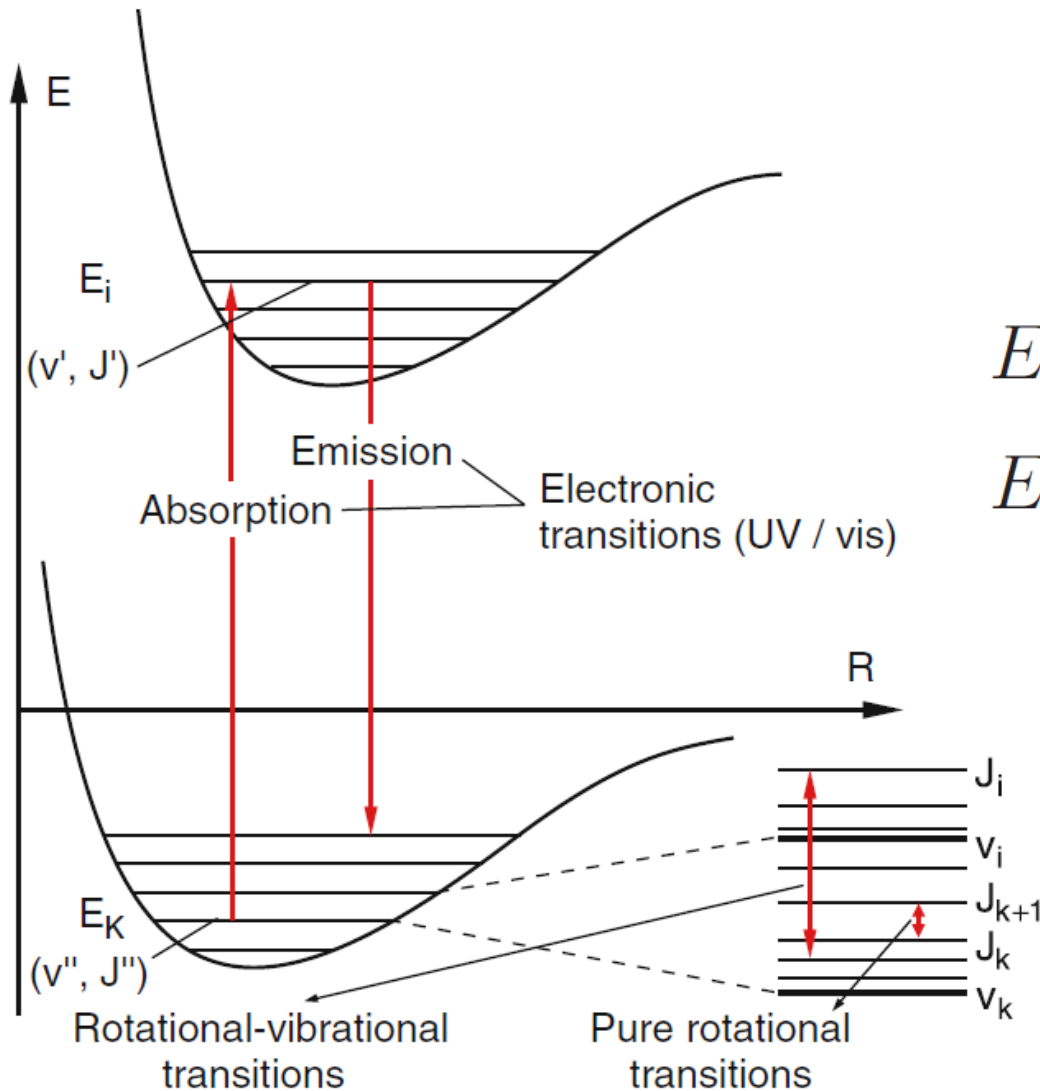
$$E_{\text{el}} \sim e^2/a_0,$$
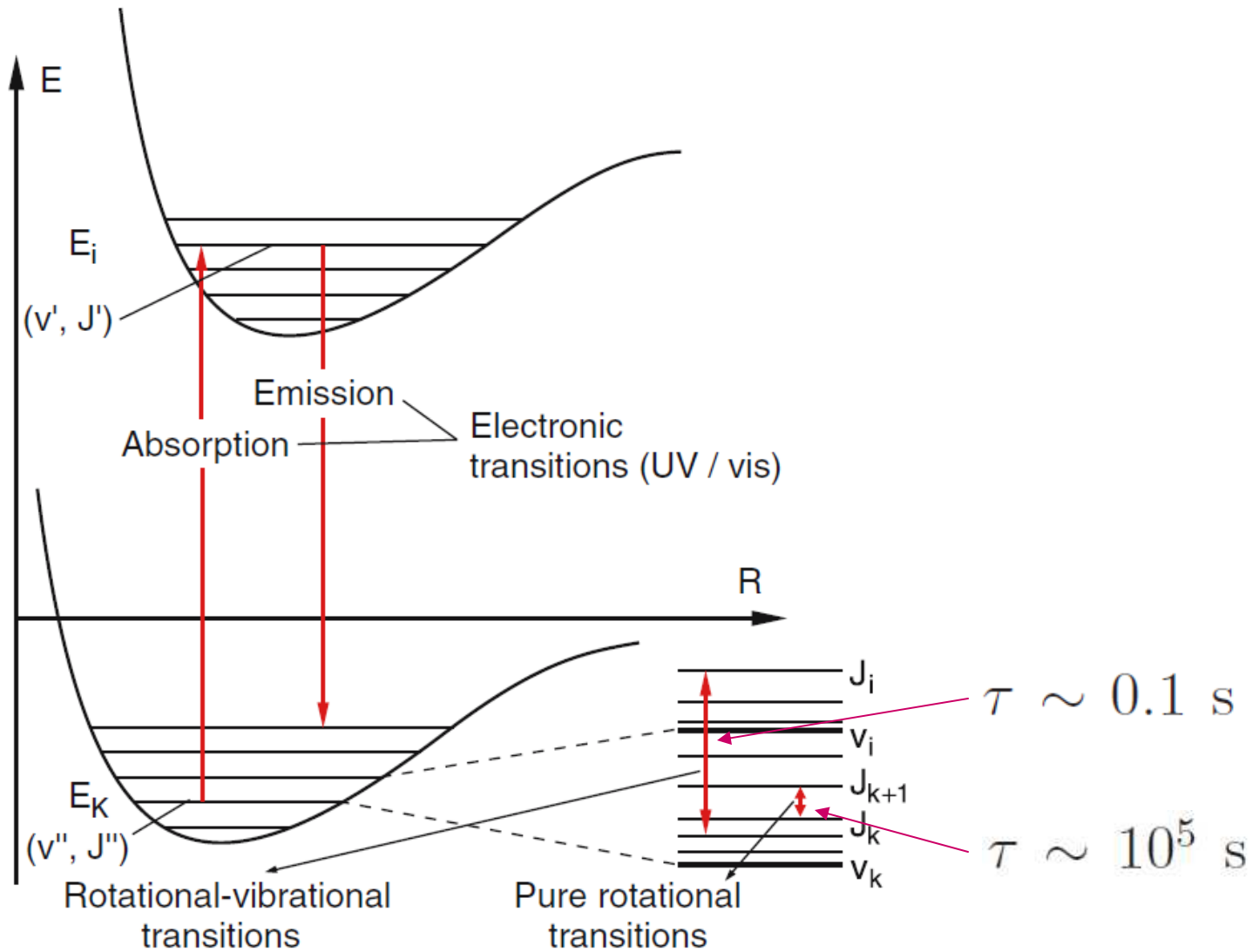$$E_{\text{el}} \sim \text{a few eV}$$

$$E_{\text{vib}} \sim \sqrt{\frac{m_e}{A m_p}} \frac{e^2}{a_0},$$
$$E_{\text{vib}} \sim 10^{-2} E_{\text{el}}.$$

$$E_{\text{rot}} \sim \frac{m_e}{A m_p} \frac{e^2}{a_0}$$
$$E_{\text{rot}} \sim 10^{-4} E_{\text{el}}.$$

Demtröder
Atoms, Molecules and Photons

Single Photon Transitions in Molecules II

Demtröder
Atoms, Molecules and Photons

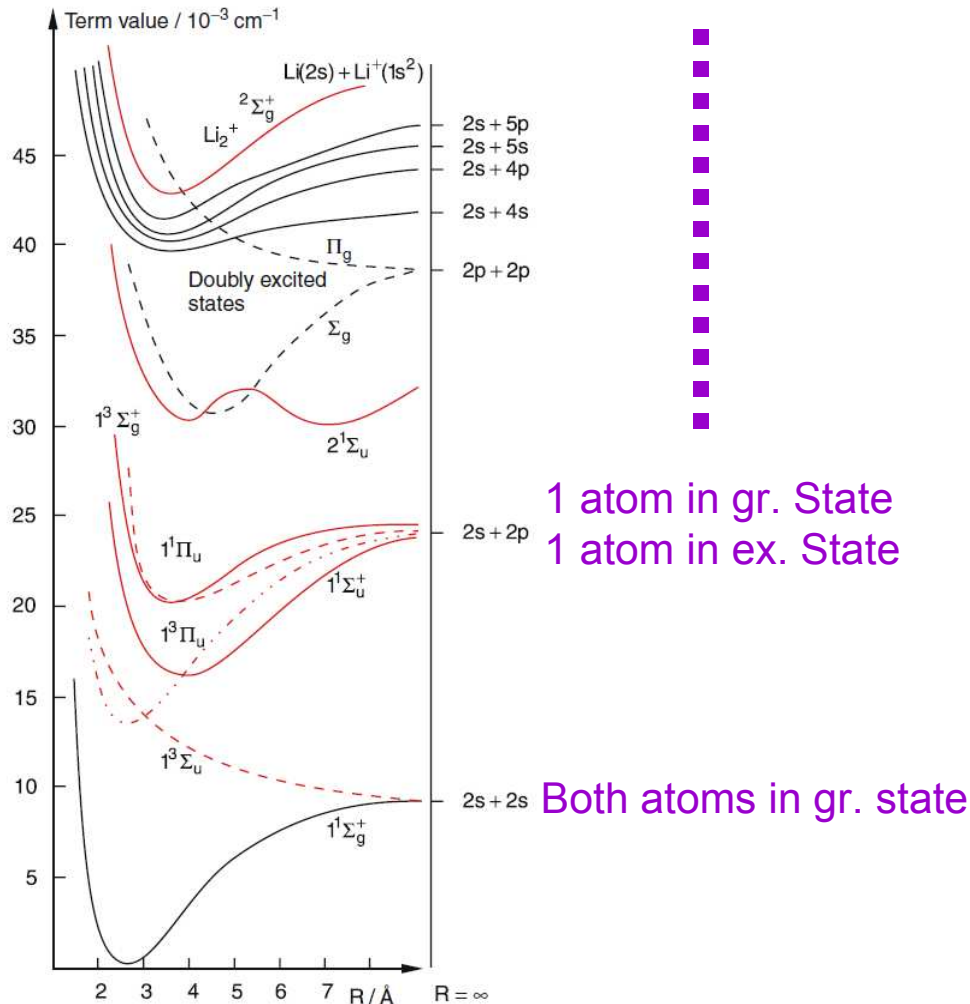# Ground and few excited molecular states of Li₂ dimer and X₂ molecule & X – X sep atoms

Fig. 9.23. Some potential curves of the Li₂ molecule up to the ionization limit, including some doubly excited states (*black dashed curves*)

1 atom in gr. State
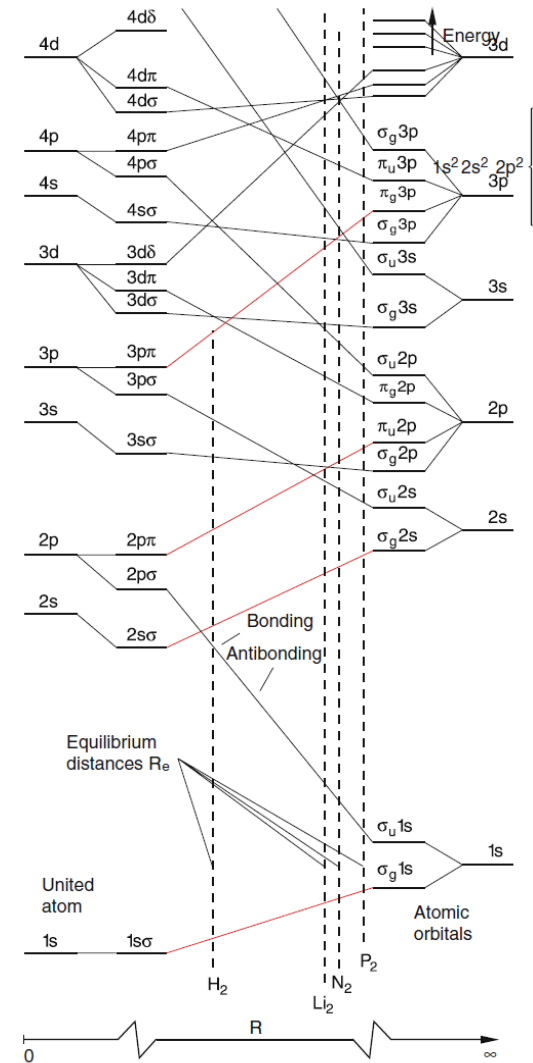1 atom in ex. State

Both atoms in gr. state

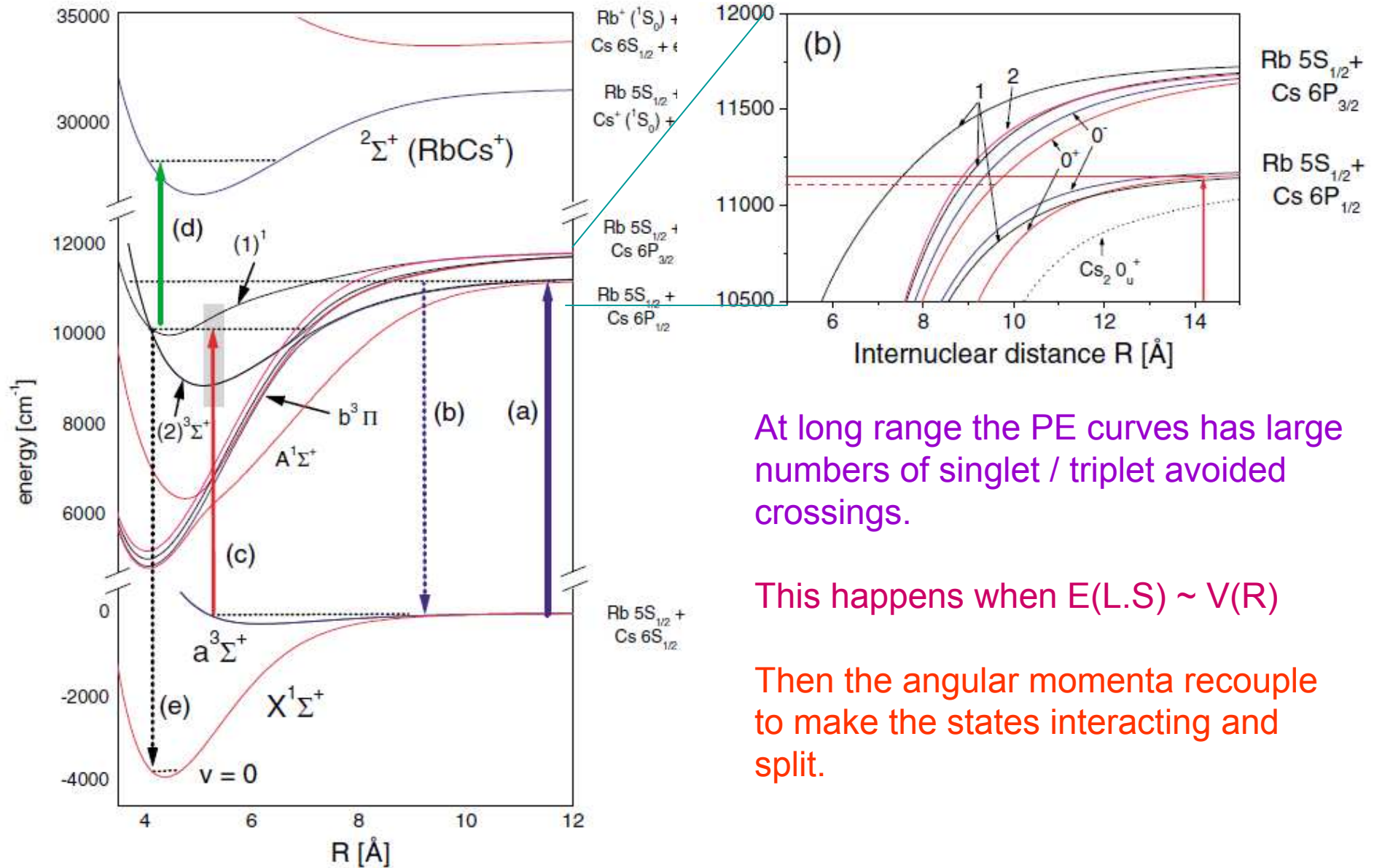**Fig. 9.25.** Correlation diagram of a homonuclear diatomic molecule. On the right side one of the atoms is always in the 1s state, to obtain singly excited molecular states

Ground and few excited molecular states of RbCs dimer and RbCs⁺

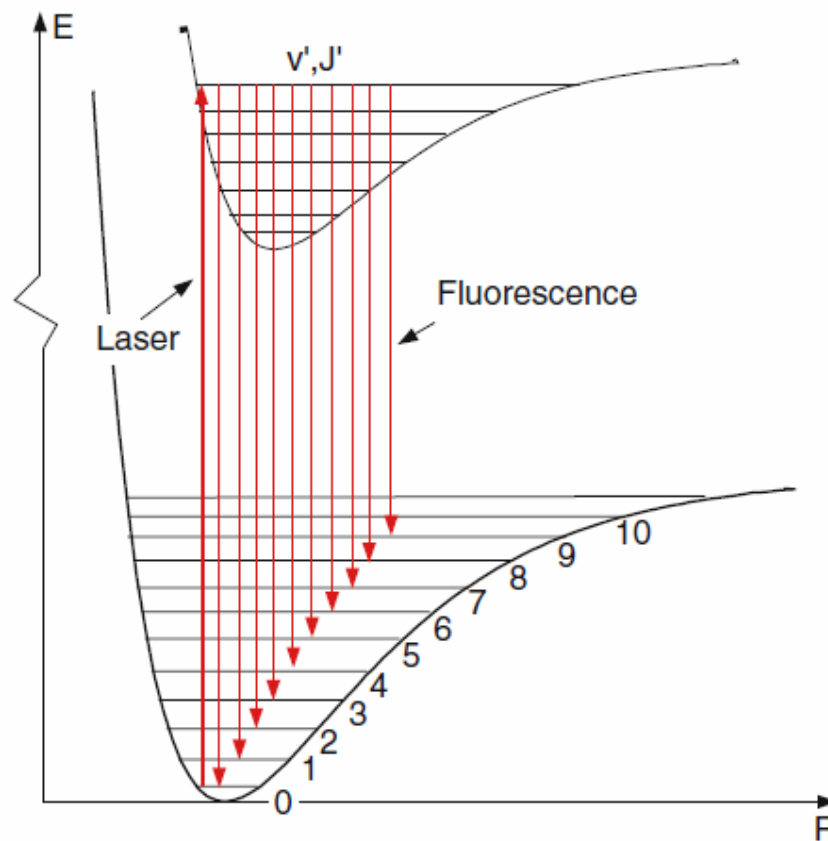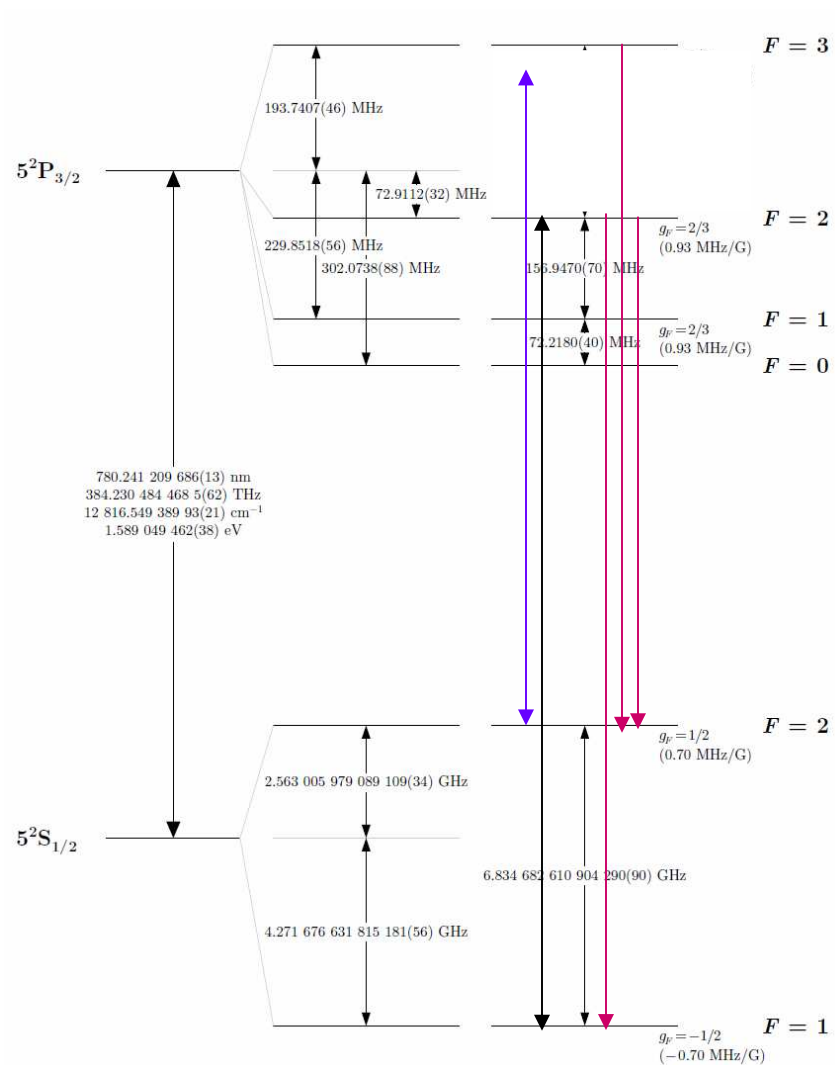At long range the PE curves has large numbers of singlet / triplet avoided crossings.

This happens when E(L.S) ~ V(R)

Then the angular momenta recouple to make the states interacting and split.

Why laser cooling molecules is difficult

The absence of closed transitions means that after a single controlled absorption followed by spontaneous emission the molecule could be in a wide variety of ground electronic states

Distinctions: Cold and Ultracold molecules

Cold molecules	Ultracold molecules
10^{-3} K < T < 1 K Many partial waves	0 < T < 10^{-3} K Single partial wave
Eg. Buffer Gas, Stark Deceleration, Stark Filtering…	Photo association, Feshbach, STIRAP…
Cold reactive chemistry Precision spectroscopy	Novel quantum systems Complex Ordered structure

Distinctions: Radicals and Molecules

| Molecules	Radicals
Bound atomic combination with paired electrons in the valance ground state	Bound atomic combination with unpaired electrons in the valance state. Chemically unstable with itself.
$S = 0$, $\Rightarrow$ not magnetically trappable $\Rightarrow$ needs optical / E field trapping	$S \neq 0$, => Magnetically trappable

Distinctions: Polar and Non-Polar molecules

Dipole Moment

No Dipole Moment

Polar molecules	Non-polar molecules
$10^{-?}$ K $< T < 10^{-2}$ K	$0 < T < 10^{-3}$ K
Diatomic: RbCs, NaCs, RbK, YbF? Polyatomic: NH_3, ND_3, CH_2O, H_2O Radicals: CaH, …	Diatomic: Rb_2, $^{39}K_2$, $^{40}K_2$, Cs_2, Na_2, $^6Li_2$, O_2…
Cold reactive chemistry Precision spectroscopy Novel quantum systems Complex Ordered structure	Ultracold collisions, BEC-BCS Feshbach resonance studies, Mott insulators and optical lattice based work

Distinctions: Diatomic and Polyatomic molecules

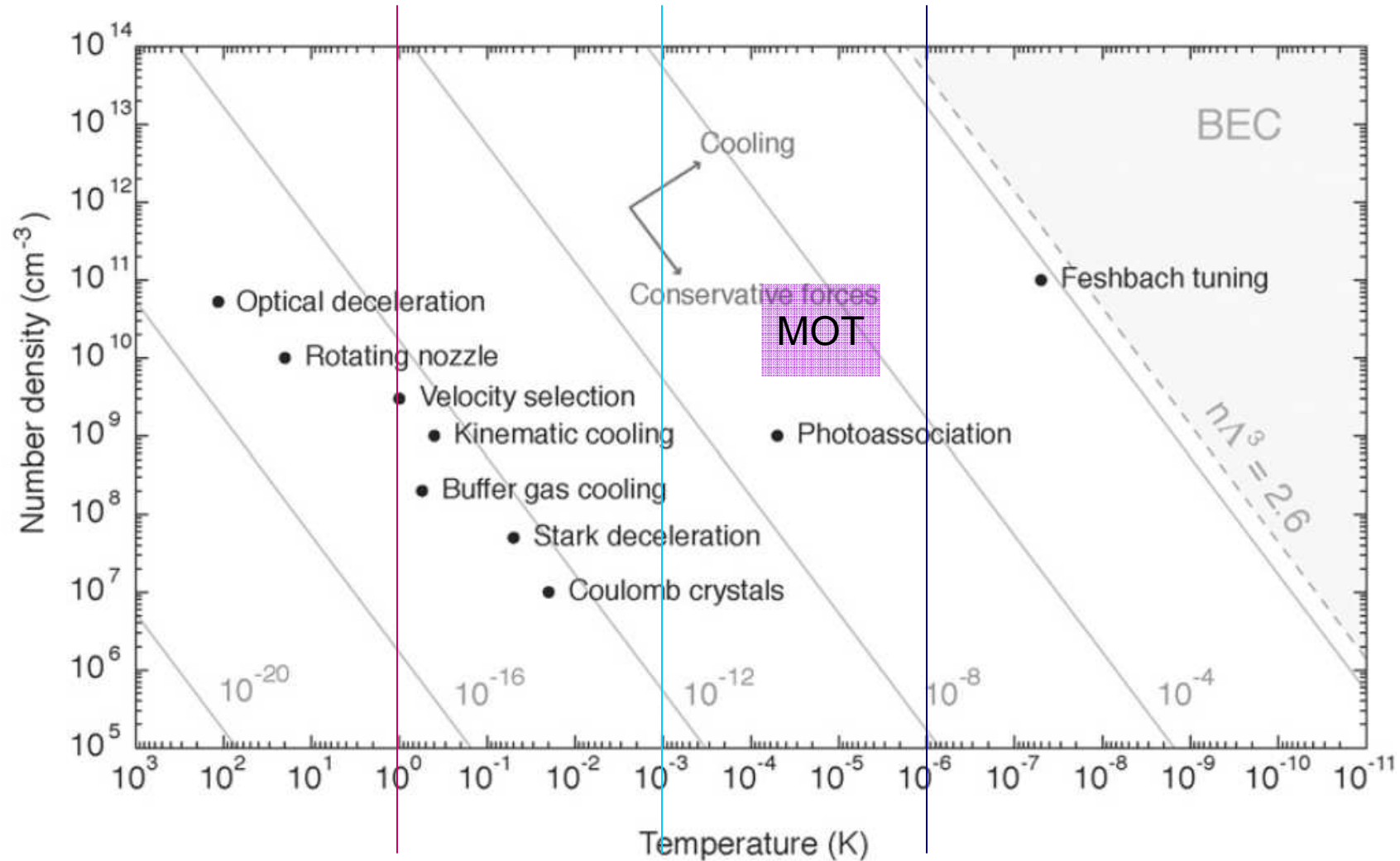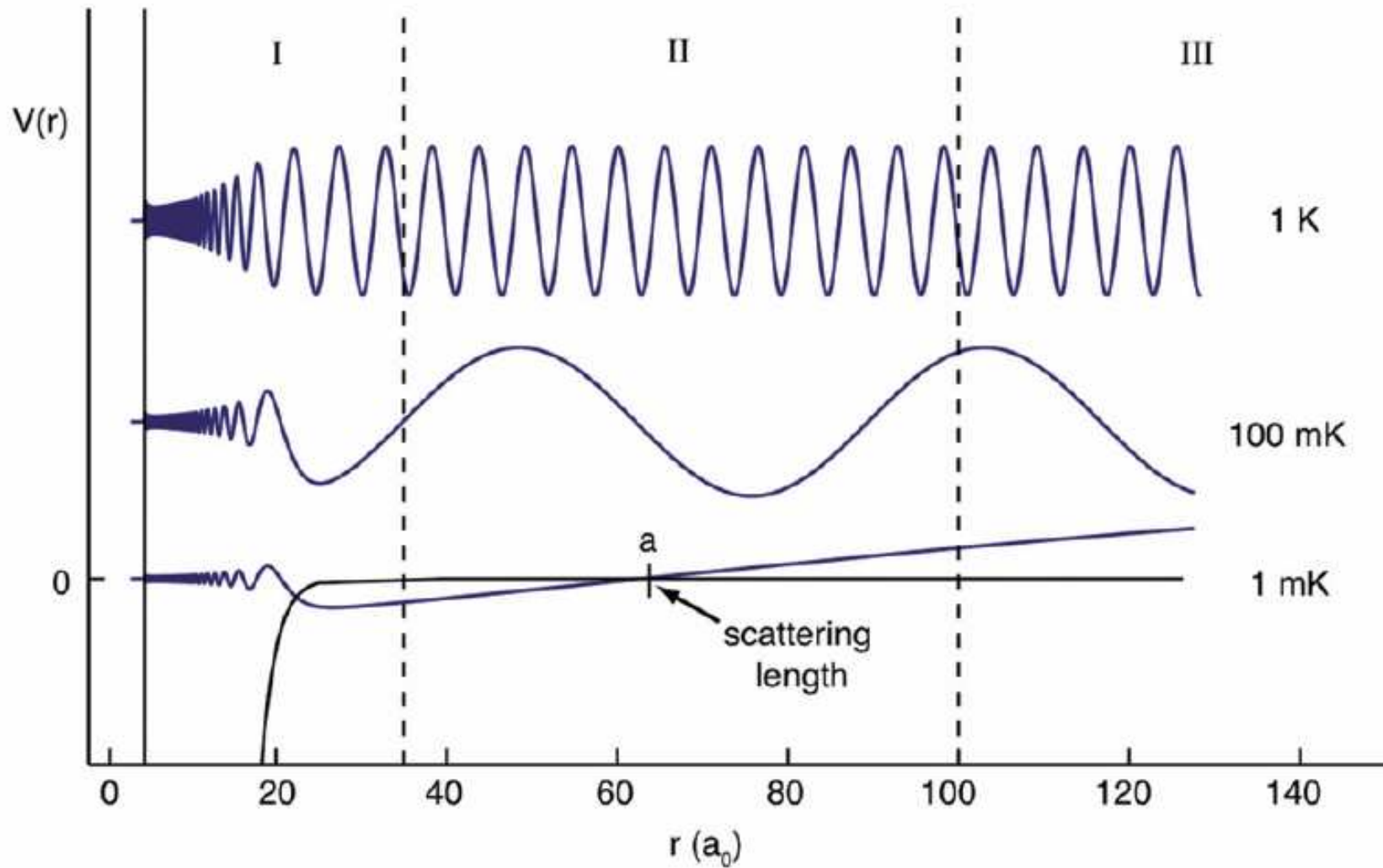| Diatomic	Polyatomic
Structure and dynamics relatively simple	Complex structure and dynamics
Can be synthesized from cold atoms	Complex dissociation dynamics
One vibrational mode	3N-6 vibrational modes
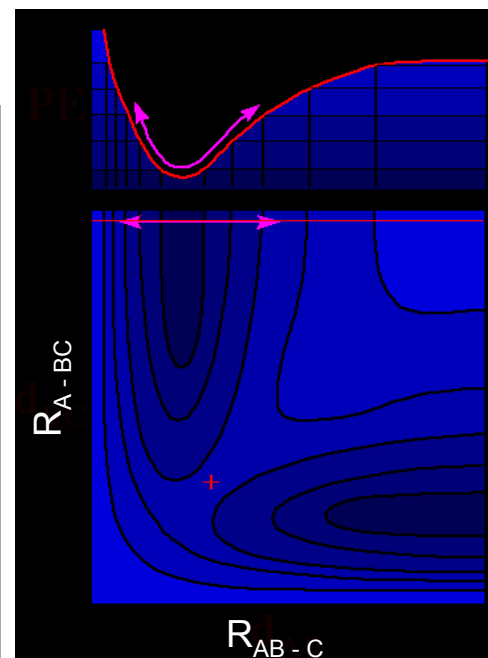
Distinctions: Short and Long Bond Length Polar Molecules

$$\mu = \mu_0 + \mu(q)$$

$$q = R - R_e$$

μ

q

E

R_e

R
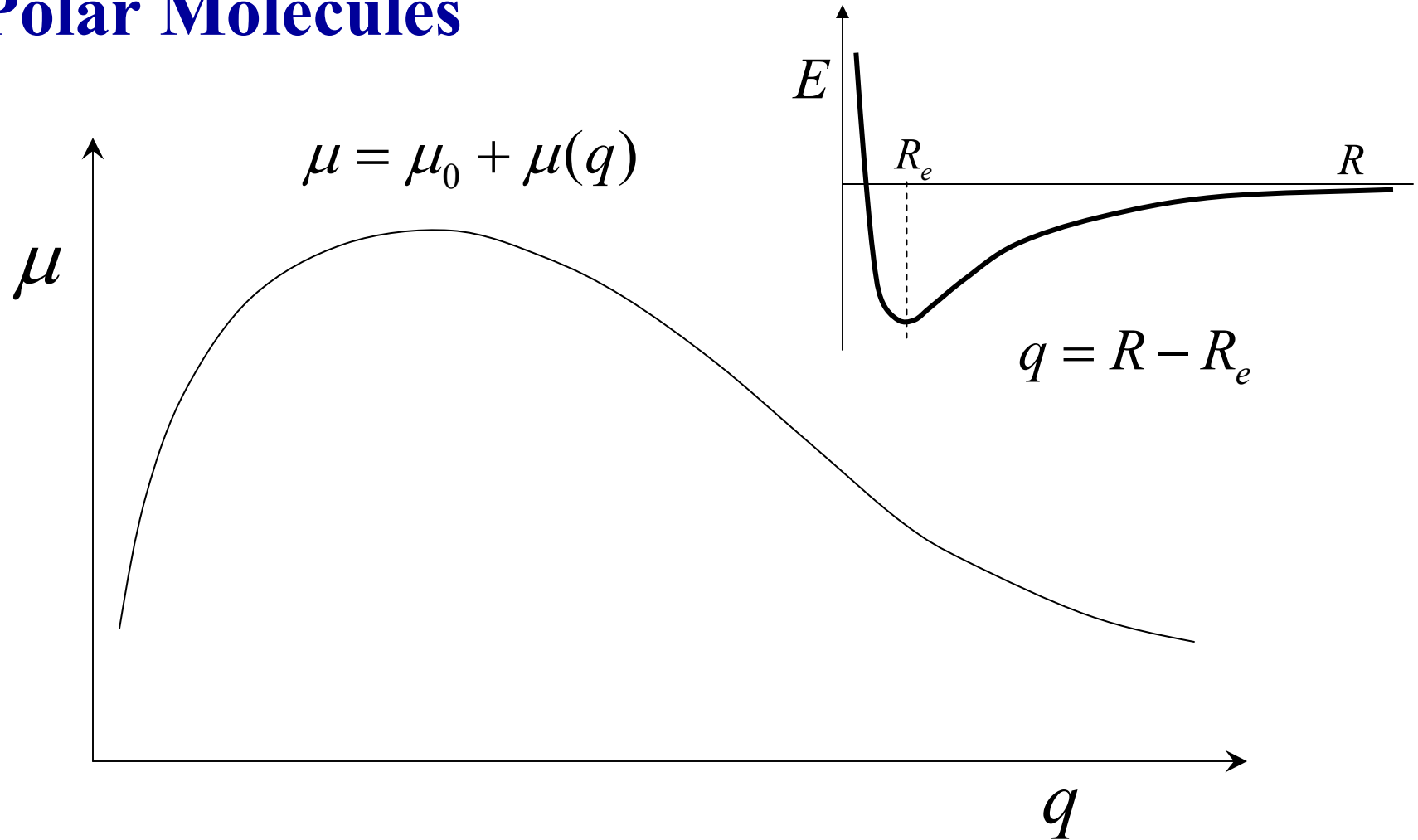
The State of the Art in cold molecules

Effective interaction with cooling

Experimental Challenges: Cold and Ultracold molecules

The formation of ultracold molecules

      We need

      large numbers

      large density

      low temperatures

The trapping of ultracold molecules

      We need

      trap loading mechanisms

      trapping mechanisms

      & often the ability to combine atom and molecule trapping in the same spatial volume

The detection of ultracold molecules

      We need

      new techniques to detect molecules

      direct molecule detection

Present Technological Status: Cold and Ultra-cold molecules

The formation of ultracold molecules

Dominant experimental directions

large numbers: possible @ > mK temp with molecules + radicals

large density: significantly lesser than cold atoms

low temperatures: wide spread of temperatures

The trapping of ultracold molecules

Top of the traps so far

Static field and time varying electric field traps

Optical traps

Magnetic field based traps

The detection of ultracold molecules

Frequently used detection techniques

Resonant multi-photon ionization followed by ion counting

Molecule re-conversion to atoms

Trap loss

The basic template for the experimental discussion: I

1. The formation of ultracold molecules
        Cold molecules from cold atoms
                Homonuclear alkali dimer molecules
                Heteronuclear alkali dimer molecules
        Cold molecules / radicals from hot molecules / radicals

2. The trapping of ultracold molecules
        Cold molecules from cold atoms approach
        Trap atoms and molecules simultaneously with spatial overlap
        Cold molecules from hot molecules approach
        New class of traps required
        Further cooling mechanisms of molecules in these traps

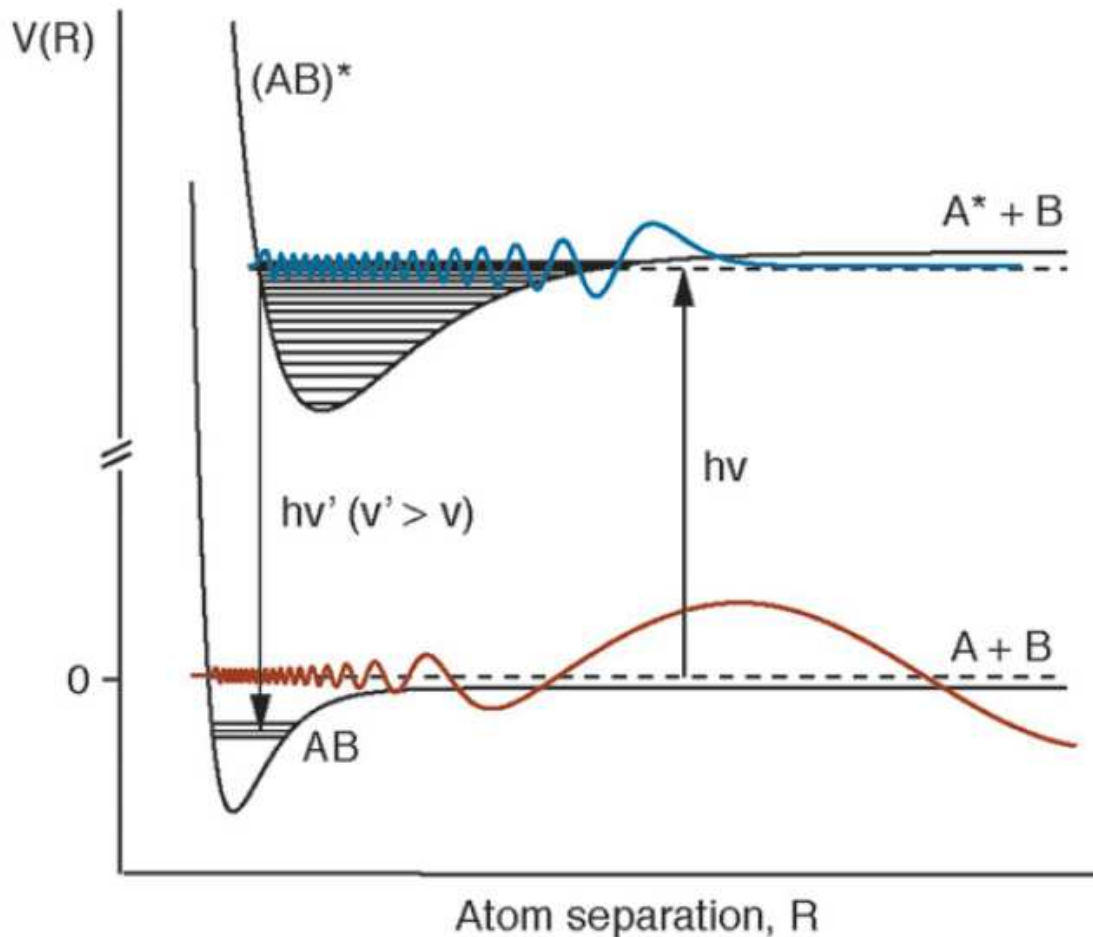3. The detection of ultracold molecules
        Resonant multi-photon ionization followed by ion counting
        Molecule re-conversion to atoms
        Trap loss

Photo-association

2 photon process that converts 2 free atoms into 1 bound molecule

In PA a laser is tuned into resonance between a scattering state of 2 gnd state atoms and a bound level of the excited molecular state.

Thus the laser frequency is red detuned to the atomic transitions
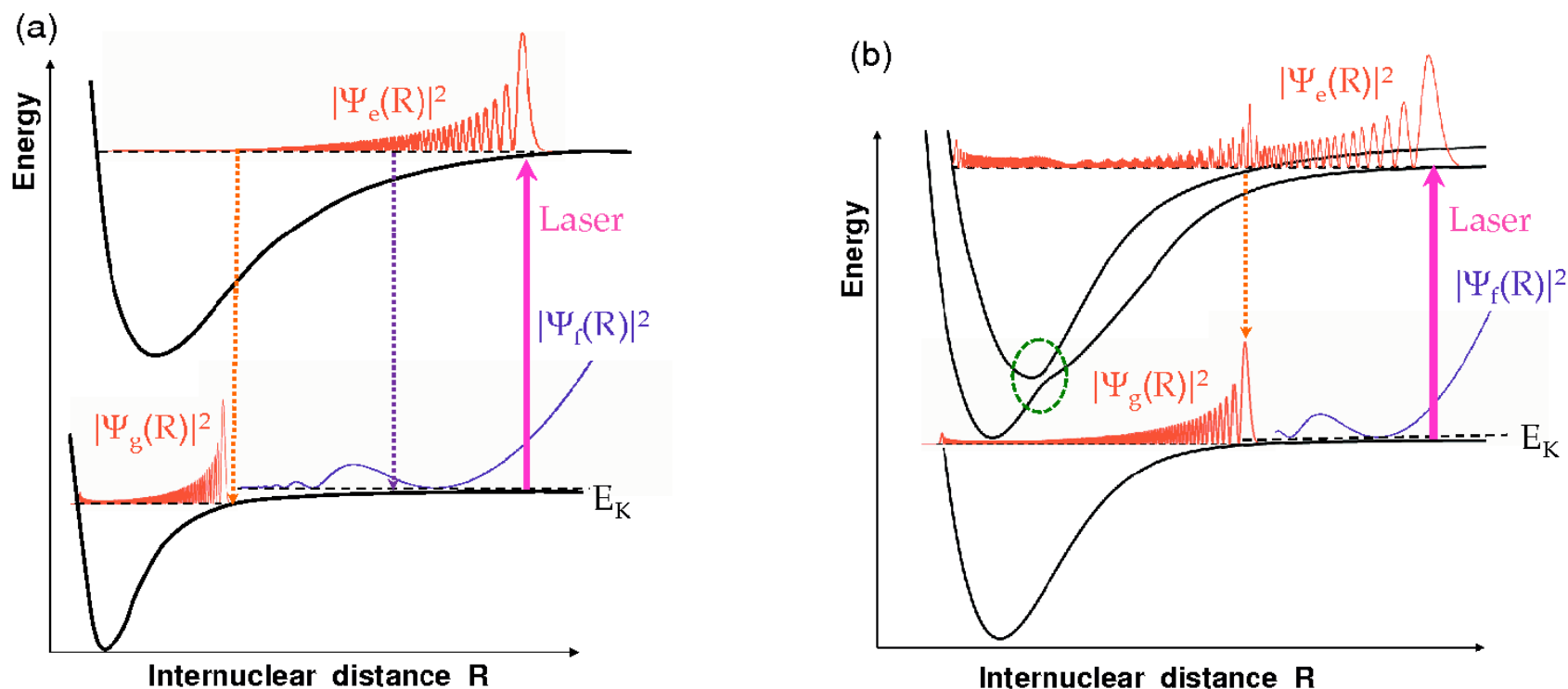
$$R_{\mathrm{PA}} \propto I_{\mathrm{L}} F_{fv'} \Omega T$$

laser intensity I_{L}

$F_{fv'}$ is the Franck–Condon factor

Ω is the phase space density

T is the temperature

Photo-association

(a)

(b)

The transition strengths for both the laser-driven upward transition and the spontaneous downward transition are determined primarily by Franck-Condon overlaps between initial and final states. (a) Simple photoassociation (PA) scheme. Here the Franck-Condon overlap is poor both for free-bound excitation and bound-bound decay, leading to small rates of bound molecule production. (b) Enhanced production of bound molecules via resonant coupling of excited-state potentials. Here the coupling between two excited state potentials (evident from the avoided crossing in the green oval) causes the excited-state vibrational wavefunction to be a mixture of states from the two potentials; one is weakly bound but the other strongly bound. The free-bound transition has strength similar to that of the simple PA scheme, but bound-bound transitions are greatly enhanced by the intermediate- and short-range peaks from the strongly bound state contribution to the excited-state wavefunction.

Photo-association

Basic Difference between Homo and Hetero-nuclear bound states for PA

Homonuclear diatomic molecules

Ground State asymptotic behaviour -> $1/R^6$

The asymptotic excited s + p state behaviour -> $1/R^3$

This makes the PA easier than for

Heteronuclear diatomic molecules where

Ground State asymptotic behaviour -> $1/R^6$

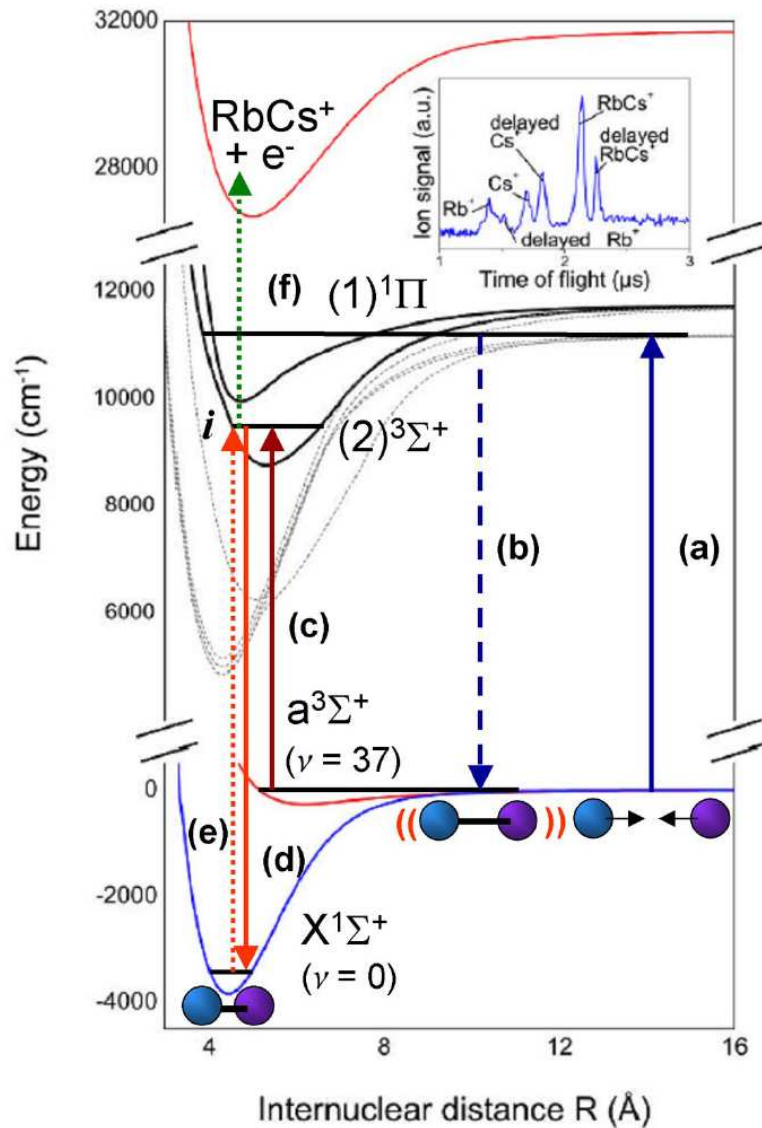and excited state is also -> $1/R^6$

Photo-association: Detection

FIG. 1 (color online). Formation and detection processes for ultracold ground state RbCs. (a) Colliding atom pairs are excited into bound RbCs* molecules, which (b) decay prominently into the $a^3\Sigma^+(v = 37)$ state. (c) Metastable $a(v = 37)$ molecules are excited to level i, then (d) stimulated into the $X^1\Sigma^+(v = 0)$ state. The molecules are detected directly by (e) driving them back to the original excited level and (f) ionizing them, or indirectly by detecting the depletion of the i level population [where only (f) is needed]. Inset: a typical time-of-flight mass spectrum showing the direct detection of $X(v = 0)$ molecules. The ion signal, averaged over 200 shots, is plotted vs delay time after the ionizing pulse. The delayed RbCs$^+$ peak signifies ground state molecule production.
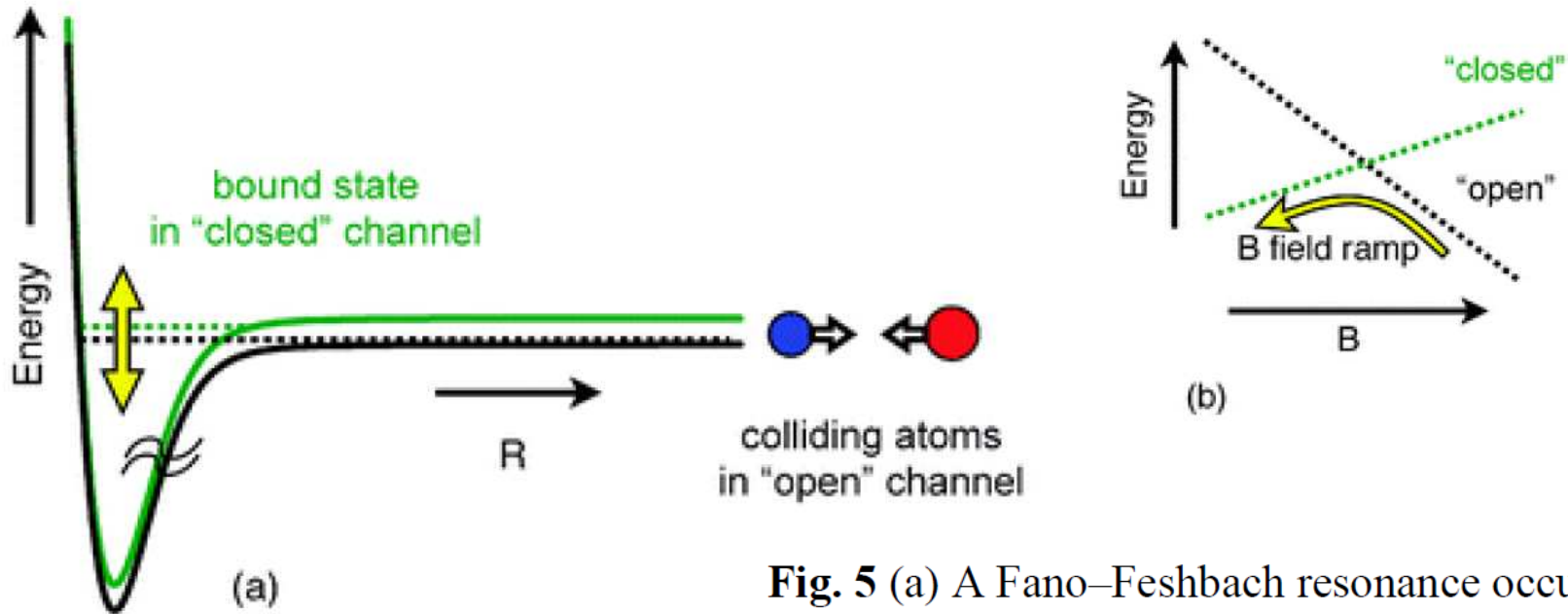
Feshbach resonance

Fig. 5 (a) A Fano–Feshbach resonance occurs when the energy of a pair of atoms in one hyperfine ("open") channel is the same as a molecular bound state in a different hyperfine ("closed") channel. The system can be tuned into and out of resonance by changing the strength of an applied external magnetic field. (b) An appropriate magnetic-field ramp (the arrow) across a Fano–Feshbach resonance can adiabatically convert pairs of atoms into weakly bound Feshbach molecules. (Energy levels are not drawn to scale).
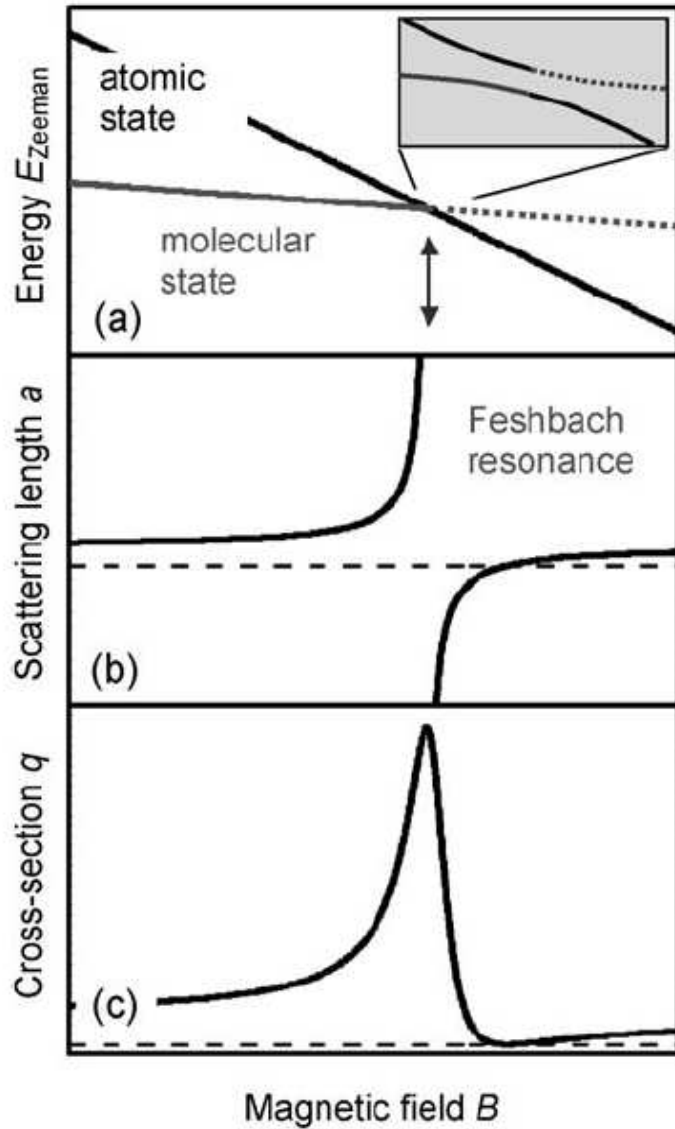
Feshbach Molecules Continued

Figure 2. A Feshbach resonance can arise through coupling between an atomic scattering state and a bound molecular state. In the process, the non-bound atom pair is transferred to the bound molecular state. a) The Zeeman energy E_{Zeeman} of the states as a function of an external magnetic field B. At a particular magnetic field (indicated by the arrow), the states cross. Coupling of the states leads to an "avoided crossing" (see inset). The s-wave scattering length a diverges at this point (b), and the elastic cross-section q (c) shows a strong resonant behavior (reproduced with permission from Ref. [37]).

Low Energy Atom Molecule Cross Sections

At very low energies (up to about 1 mK), the cross sections are dominated by collisions with orbital angular momentum $l = 0$, for which there are no centrifugal barriers. The s-wave cross sections for $^7Li + ^6Li^7Li(v = 0, n = 0)$ are shown as a function of collision energy E in Fig. 1. There is an energetically allowed reactive pathway to form $^7Li_2(v = 0, n = 0) + ^6Li$; at collision energies above 0.477 K the $v = 0$, $n = 2$ state of $^7Li_2$ is also accessible.
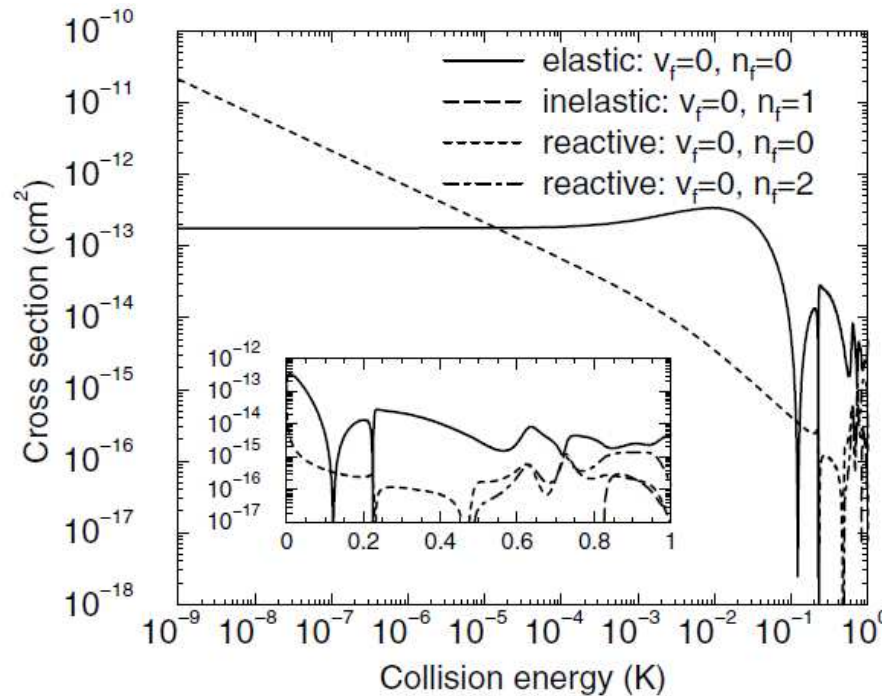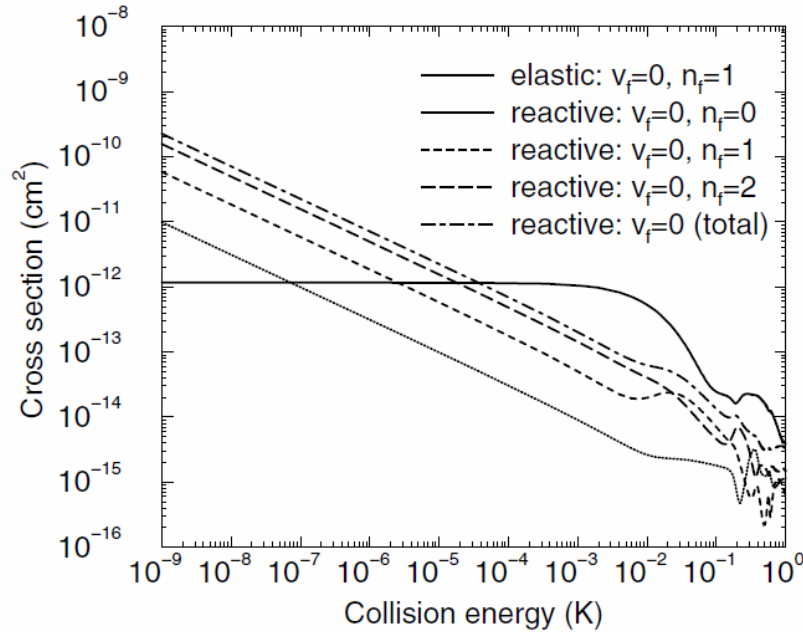
FIG. 1. Elastic and reactive s-wave cross sections for $^7Li + ^6Li^7Li(v = 0, n = 0)$. The inset shows the higher-energy cross sections on a log-linear scale, with axes in the same units as the main plot.

Low Energy Atom Molecule Cross Sections

ultracold regime. For example, in the limit of low collision energies, the cross sections for elastic scattering caused by short-range intermolecular potentials are predicted to vary as

$$\sigma_l^{el}(k) \sim k^{4l}, \qquad (13)$$

where k is the wave-vector associated with the collision energy $E_c = \hbar^2 k^2 / 2\mu$, and l is the orbital angular momentum quantum number of the collision partners. As observed above, elastic cross sections are therefore expected to become constant at low energies.

FIG. 3. Elastic and reactive cross sections for $^7Li + {}^6Li_2(v = 0, n = 1)$ with $J^{II} = 1^-$.
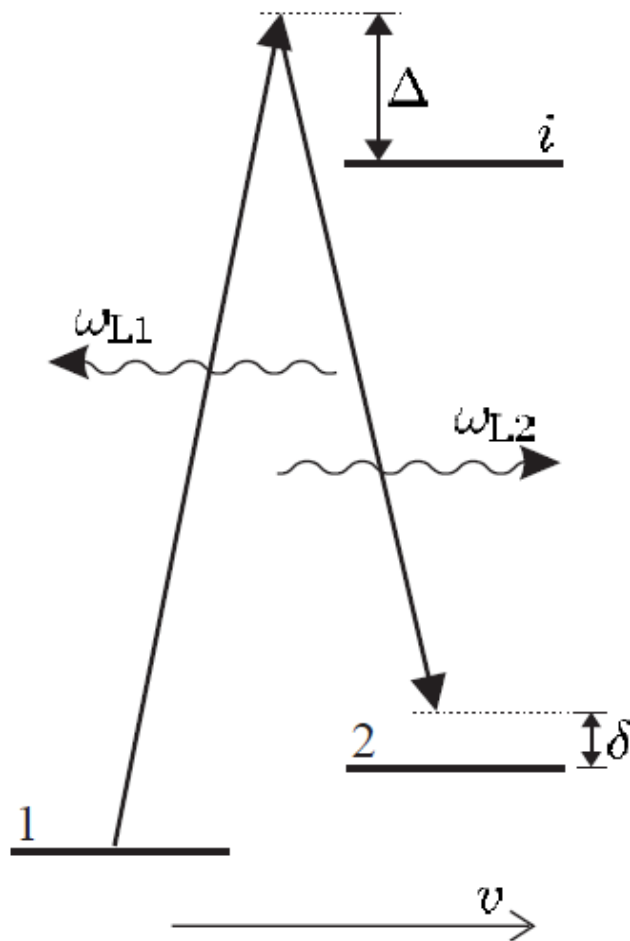
Raman Transitions

Fig. 9.20 A Raman transition between levels 1 and 2 driven by two laser beams of (angular) frequencies ω_{L1} and ω_{L2}. For a resonant Raman process the frequency detuning $\delta \simeq 0$, and the detuning Δ from the intermediate state remains large, so that excitation by single-photon absorption is negligible in comparison to the coherent transfer from $|1\rangle$ to $|2\rangle$. In this example the atom has velocity v along the direction of the laser beam with frequency ω_{L2}, and the laser beam with frequency ω_{L1} propagates in the opposite direction.
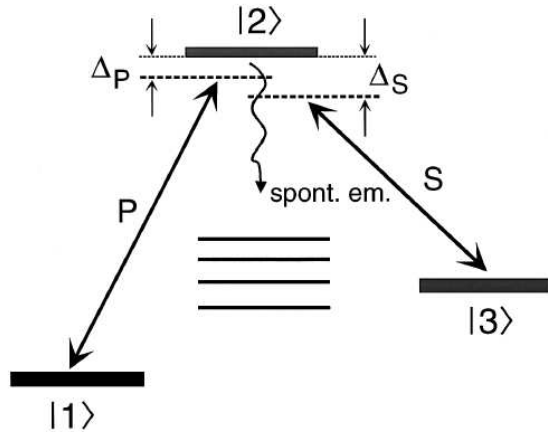
STImulated Raman Adiabatic Passage - I

FIG. 1. Three-level excitation scheme. The initially populated state $|1\rangle$ and the final state $|3\rangle$ are coupled by the Stokes laser S and the pump laser P via an intermediate state $|2\rangle$. This latter state may decay by spontaneous emission to other levels. The detuning of the pump and Stokes laser frequencies from the transition frequency to the intermediate state are Δ_P and Δ_S, respectively.

For the simplest implementation of STIRAP, the Hamiltonian, which describes the coupling of the three states (nondegenerate levels) by two coherent radiation fields within the rotating wave approximation (RWA; Shore, 1990, Sec. 13.7), reads

$$H(t) = \frac{\hbar}{2} \begin{bmatrix} 0 & \Omega_P(t) & 0 \\ \Omega_P(t) & 2\Delta_P & \Omega_S(t) \\ 0 & \Omega_S(t) & 2(\Delta_P - \Delta_S) \end{bmatrix}. \tag{7}$$

The coupling strength between the states is determined by the pulsed Rabi frequencies $\Omega_S(t)$ and $\Omega_P(t)$, while the detuning from the intermediate state or from the two-photon resonance appears as the elements on the diagonal: $\hbar\Delta_P = (E_2 - E_1) - \hbar\omega_P$ is the detuning (energy) of the pump laser from resonance with the $|2\rangle$-$|1\rangle$ transition and $\hbar\Delta_S = (E_2 - E_3) - \hbar\omega_S$ is the detuning of the Stokes laser from the $|2\rangle$-$|3\rangle$ transition. Although the presence of these single-photon detunings does not prevent population transfer, it is essential that the two-photon resonance condition $\Delta_P = \Delta_S$ apply (for a discussion of the two-photon linewidth in this situation, see Romanenko and Yatsenko, 1997).

STImulated Raman Adiabatic Passage - II

In the following, we discuss the dynamics of coherent excitation in the basis of time-dependent eigenstates of the RWA Hamiltonian of Eq. (7). It is straightforward to verify that the following linear combinations of the bare states $|1\rangle$, $|2\rangle$, and $|3\rangle$ are eigenstates of the instantaneous RWA Hamiltonian of Eq. (7):

$$|a^+\rangle = \sin\Theta \, \sin\Phi|1\rangle + \cos\Phi|2\rangle + \cos\Theta \, \sin\Phi|3\rangle,$$

$$|a^0\rangle = \cos\Theta|1\rangle - \sin\Theta|3\rangle,$$

$$|a^-\rangle = \sin\Theta \, \cos\Phi|1\rangle - \sin\Phi|2\rangle + \cos\Theta \, \cos\Phi|3\rangle, \quad (8)$$

where the (time-varying) mixing angle Θ is defined by the relationship

$$\tan\Theta = \frac{\Omega_P(t)}{\Omega_S(t)}. \quad (9)$$

The angle Φ is a known function of the Rabi frequencies and detunings and is of no relevance to the subsequent discussion (Fewell, Shore, and Bergmann, 1997). The eigenstates given by Eq. (8) are valid for the case of

$$\omega^+ = \Delta_P + \sqrt{\Delta_P^2 + \Omega_P^2 + \Omega_S^2}, \quad \omega^0 = 0,$$

$$\omega^- = \Delta_P - \sqrt{\Delta_P^2 + \Omega_P^2 + \Omega_S^2}.$$
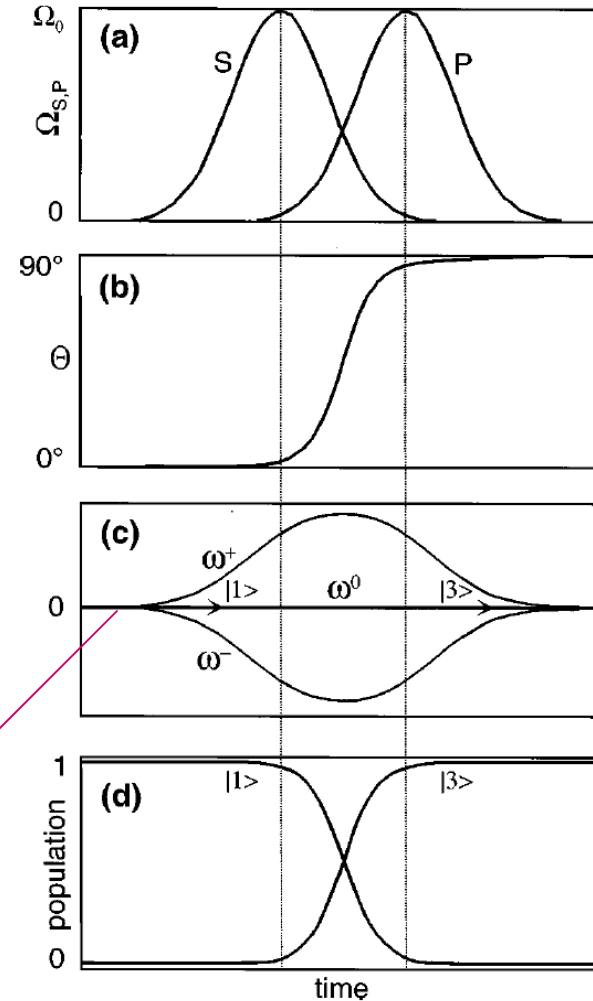
FIG. 3. Time evolution of (a) the Rabi frequencies of the pump and Stokes laser (see Fig. 1); (b) the mixing angle [see Eq. (9)]; (c) the dressed-state eigenvalues [see Eq. (10)]; and (d) the population of the initial level (starting at unity) and the final level (reaching unity).
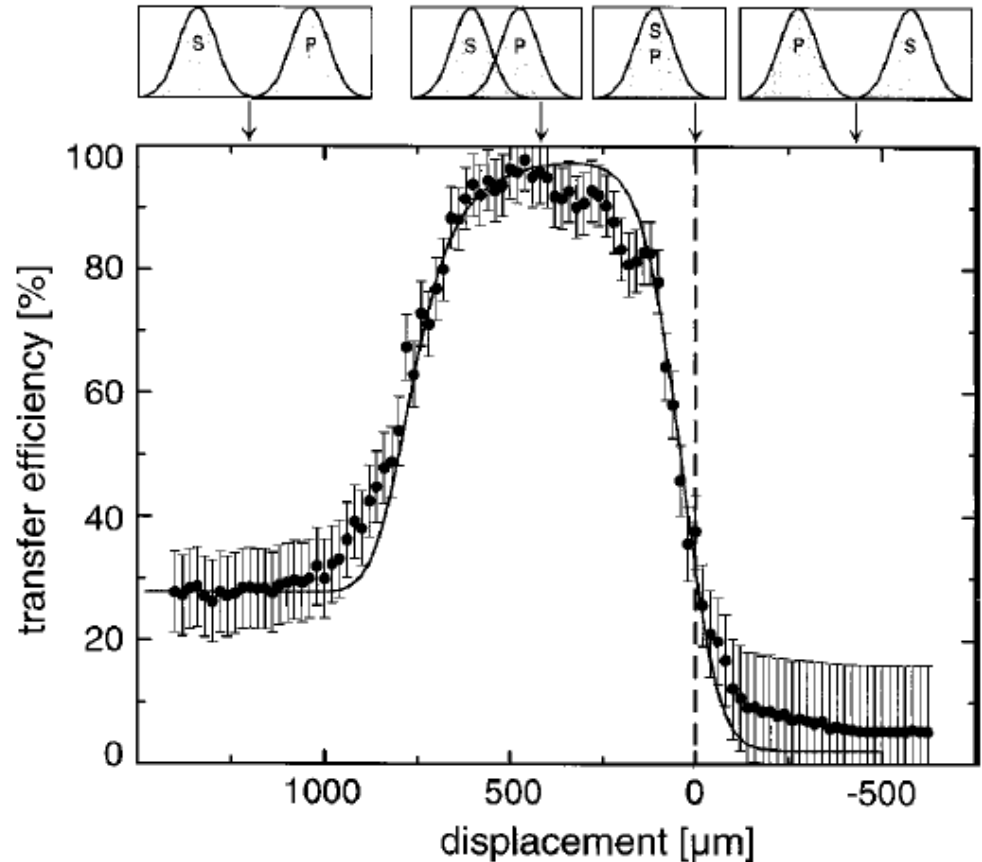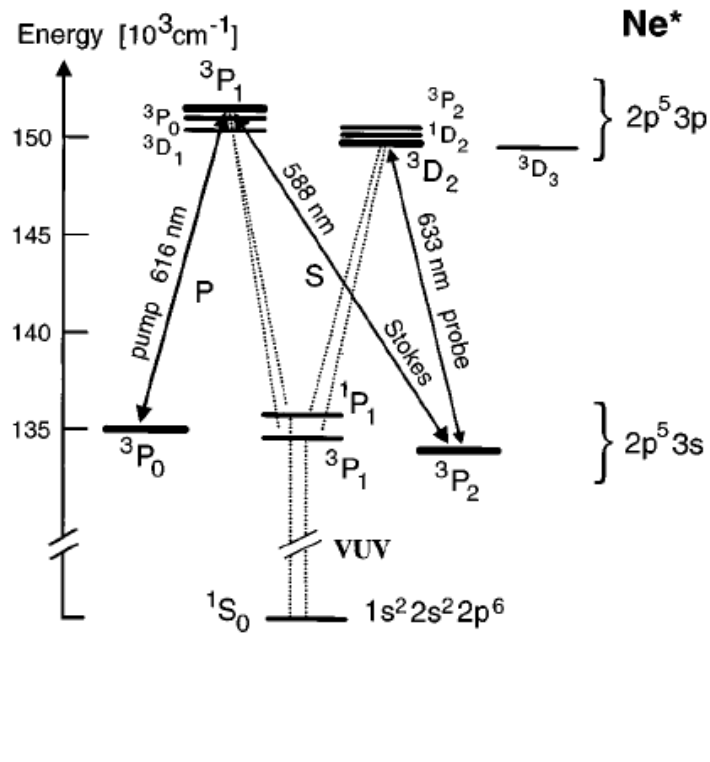
Contents

FIG. 9. Population transfer from the $^3P_0$ state to the $^3P_2$ state (see Fig. 6), induced by a continuous laser, as a function of the overlap between the Stokes and the pump lasers (shown on top).

Dipole Trap in Brief

$$U_{\text{dipole}} \simeq \frac{\hbar \Omega^2}{4\delta} \equiv \frac{\hbar \Gamma}{8} \frac{\Gamma}{\delta} \frac{I}{I_{\text{sat}}}. \tag{9.46}$$

When δ is positive ($\omega > \omega_0$) this potential has a maximum where the intensity is highest—the atom is repelled from regions of high intensity. In the opposite case of frequency detuning to the red (δ negative) the dipole force acts in the direction of increasing I, and U_{dipole} is an attractive potential—atoms in a tightly-focused laser beam are attracted towards the region of high intensity, both in the radial direction and along the axis of the beam. This dipole force confines atoms at the focus of a laser beam in an analogous way to optical tweezers to create a dipole-force trap.[42] Normally, dipole traps operate at large frequency detuning ($|\delta| \gg \Gamma$), where to a good approximation eqn 9.3 becomes

$$R_{\text{scatt}} \simeq \frac{\Gamma}{8} \frac{\Gamma^2}{\delta^2} \frac{I}{I_{\text{sat}}}. \tag{9.47}$$

This scattering rate depends on I/δ^2, whereas the trap depth is proportional to I/δ (in eqn 9.46). Thus working at a sufficiently large frequency detuning reduces the scattering whilst maintaining a reasonable trap depth (for a high intensity at the focus of the laser beam). Usually there are two important criteria in the design of dipole-force traps: (a) the trap must be deep enough to confine the atoms at a certain temperature (that depends on the method of cooling); and (b) the scattering rate must be low to reduce heating.
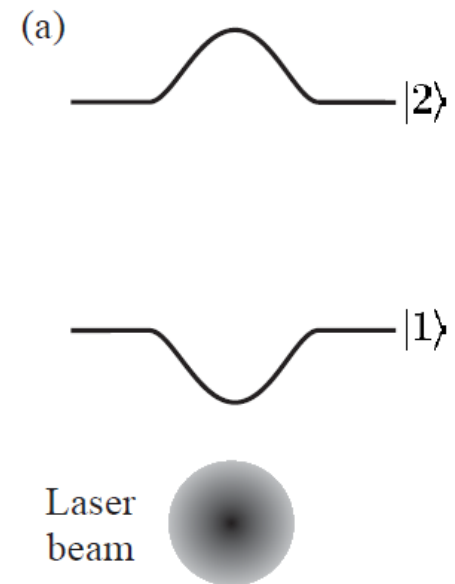
(a)

$|2\rangle$

$|1\rangle$

Laser beam

Fig. 9.14 (a) An intense laser beam alters the energy levels of an atom, as illustrated for a radial direction across a laser beam propagating perpendicular to the plane of the figure. For a laser frequency less than the atomic resonance frequency the a.c. Stark effect forms a potential well in the ground-state energy and atoms are attracted towards regions of high intensity. (b)

Foot: Atomic Physics

Dipole Force: Numbers

Example 9.2 *Dipole trapping of sodium atoms*
The wavelength of the laser light used for a dipole-force trap depends mainly on practical considerations.[43] It is convenient to use a high-power solid-state laser such as a Neodymium:YAG laser that produces continuous-wave radiation at a fixed infra-red wavelength of $\lambda = 1.06\,\mu$m. The frequency detuning of this laser radiation from the sodium resonance at $\lambda_0 = 589\,$nm is

$$\frac{\delta}{\Gamma} = \frac{2\pi}{\Gamma}\left\{\frac{c}{\lambda_0} - \frac{c}{\lambda}\right\} = 2.3 \times 10^7, \qquad (9.48)$$

in units of Γ, where $1/\Gamma = \tau = 16\,$ns.[44] Solid-state lasers can produce powers of many tens of watts, but in this example we use a conservative value of $P = 1\,$W. When focused to a waist of $w_0 = 10\,\mu$m this laser beam has an intensity of $I = 2P/(\pi w_0^2) = 6.4 \times 10^9\,$W m$^{-2} \equiv 1 \times 10^8\,I_{\mathrm{sat}}$. Equation 9.46 gives

$$U_{\mathrm{dipole}} = \frac{\hbar\Gamma}{2} \times 1.1 = 260\,\mu\mathrm{K}. \qquad (9.49)$$

Thus atoms cooled below the Doppler cooling limit $\hbar\Gamma/2$ can be trapped. For this laser intensity and frequency detuning, eqn 9.47 gives

$$R_{\mathrm{scatt}} = 2.4 \times 10^{-8}\,\Gamma = 2\,\mathrm{s}^{-1}. \qquad (9.50)$$

A sodium atom only scatters a few photons per second which gives a low heating rate.[45] The scattering force is negligible for these conditions,[46]

Foot: Atomic Physics

The STIRAP process in RbK: Triplet

Fig. 1. Diagram of the KRb electronic ground and excited molecular potentials and the vibrational levels involved in the two-photon coherent state transfer to the triplet ground state. Here, the intermediate state $|e\rangle$ is the $v' = 10$ level of the electronically excited $2^3\Sigma$ potential. The vertical arrows are placed at the respective Condon points of the up and down transitions. The intermediate state has favorable transition dipole moments for both the up leg ($|i\rangle$ to $|e\rangle$) and the down leg ($|e\rangle$ to $|g\rangle$), where the initial state $|i\rangle$ is a weakly bound Feshbach molecule and the final state $|g\rangle$ is the rovibrational ground state ($v = 0$, $N = 0$) of the triplet electronic ground potential, $a^3\Sigma$.
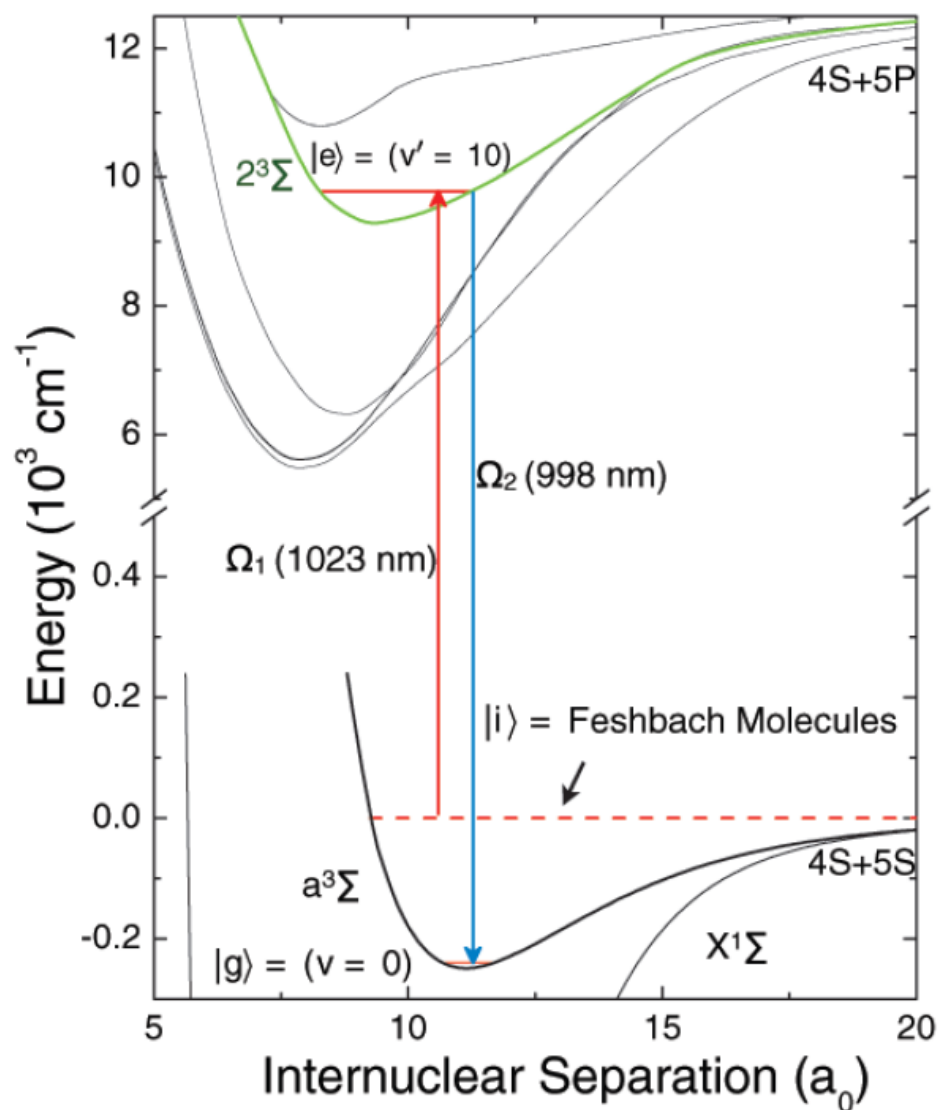
Rotational and Hyperfine states in Ground Triplet

Fig. 2. The $v = 0$ ground-state level of the triplet electronic ground potential, $a^3\Sigma$. (**A**) Hyperfine and rotational states of the $a^3\Sigma$ $v = 0$ ground-state molecule at a magnetic field of 546.94 G, observed using two-photon spectroscopy and scanning the down leg (Ω_2) frequency. The measured number of remaining Feshbach molecules is plotted as a function of the frequency difference of the two laser fields. We show two sets of data, vertically offset for clarity, obtained using two different intermediate states, which are hyperfine and rotational states of the $v' = 10$ level of the electronically excited $2^3\Sigma$ potential. Peaks labeled 1 and 2 correspond to hyperfine states in the rotational ground-state, and peak 3 corresponds to a rotationally excited state. (**B**) We precisely determine the energy and the transition dipole moments for individual states using the two-photon spectroscopy where we scan the up leg (Ω_1) frequency. The measured number of remaining Feshbach molecules is plotted as a function of the two-photon detuning. The dark resonance shown here is for the triplet rovibrational ground state corresponding to peak 2 in (A).
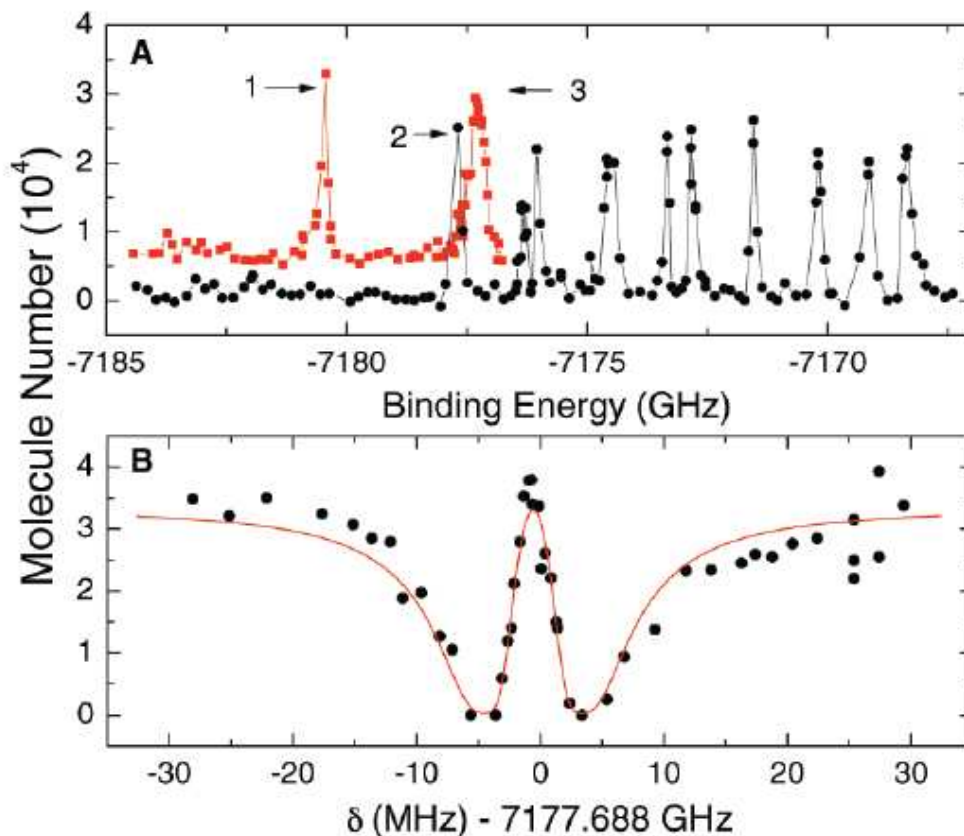
STIRAP efficiency

Fig. 3. Time evolution of the initial state population during STIRAP state transfer and a measurement of the triplet rovibrational ground-state molecule lifetime. (**A**) Here, we monitor the Feshbach molecule population as we apply the STIRAP pulse sequence. Weakly bound Feshbach molecules are coherently transferred into the triplet rovibrational ground state after a 25-μs one-way STIRAP pulse sequence. The measured population completely disappears because the deeply bound molecules are dark to the imaging light. After a 10-μs hold, we then perform the reversed STIRAP pulse sequence that coherently transfers the ground-state molecules back to Feshbach molecules. The molecule number after the round-trip STIRAP is 1.8×10^4. Assuming equal transfer efficiency for the two STIRAP sequences, we obtain one-way transfer efficiency of 56% and an absolute number of triplet rovibrational ground-state polar molecules of 3.2×10^4. (**B**) We measure the triplet $v = 0$ lifetime by varying the hold time after one-way STIRAP before transferring them back to Feshbach molecules for imaging. The lifetime is measured to be 170(30) μs.
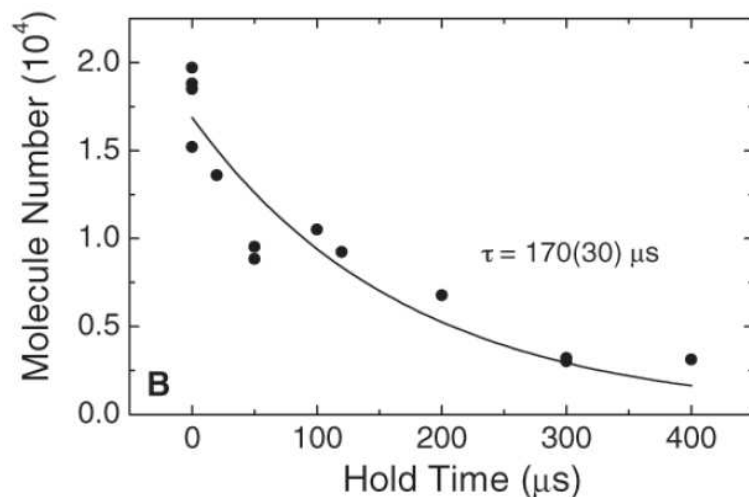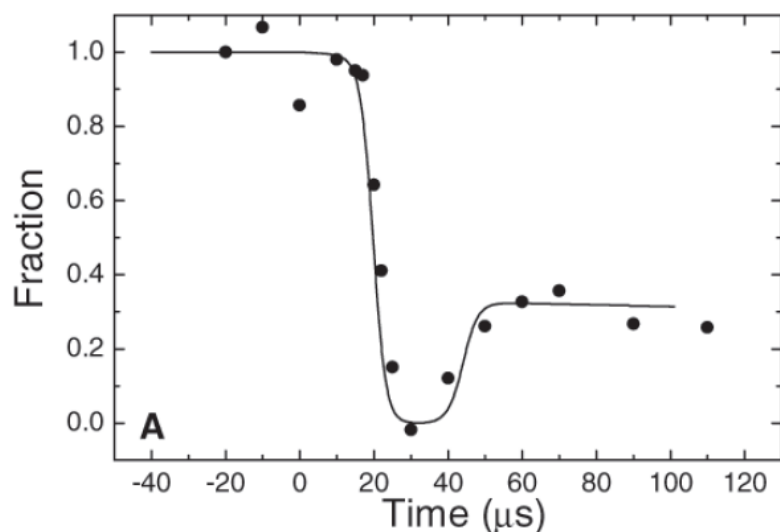
Stark Spectroscopy: Dipole Moment Determination (Triplet)

Fig. 4. Stark spectroscopy of the triplet $v = 0$ molecules. Stark shifts of the lowest three states in the triplet $v = 0$ manifold in Fig. 2A are measured for a dc electric field in the range from 0 to 2 kV/cm. Vertical error bars represent 1 SD error from the determination of the resonance center fitted to a Lorentzian lineshape. The bottom panel shows the Stark shifts of the two lowest energy states, which are $N = 0$. Fits to the shifts of peak 1 (solid circles) and peak 2 (open circles) yield an electric dipole moment and statistical error bar of 0.052106(2) D and 0.052299(8) D respectively. The dominant systematic error in the dipole moment measurement comes from a 3% uncertainty of the electric field (horizontal error bars). A combined fit for shifts of peak 1 and peak 2 is shown as the solid curve in the bottom panel. With the electric field uncertainty, we obtain an electric dipole moment of 0.052(2) D. The top panel shows the Stark shift of peak 3 (squares) and the expected $N = 2$ curves calculated for an electric dipole moment of 0.052 D and different $|m_N\rangle$ projections.

$$\Delta E \propto \frac{(\vec{\mu} \cdot \vec{E})^2}{hBJ(J+1)}$$

The STIRAP process in RbK: Singlet
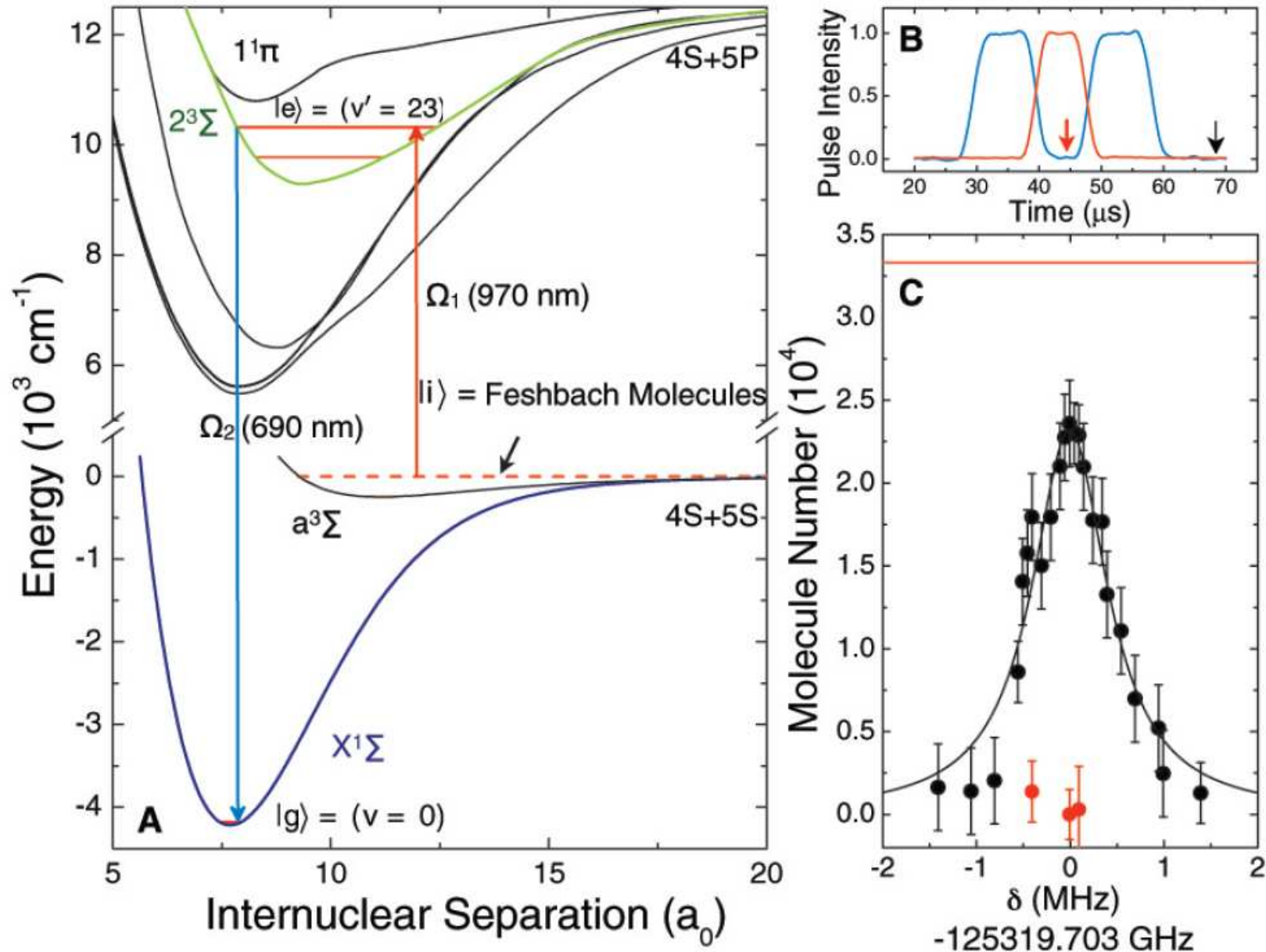
Fig. 5. Two-photon coherent state transfer from weakly bound Feshbach molecules $|i\rangle$ to the absolute molecular ground state $|g\rangle$ ($v = 0$, $N = 0$ of $X^1\Sigma$). (**A**) Transfer scheme. Here, the intermediate state $|e\rangle$ is the $v' = 23$ level of the $\Omega = 1$ component of the electronically excited $2^3\Sigma$ potential. The chosen intermediate state lies just below the $1^1\Pi$ excited electronic potential, which provides the necessary triplet-singlet spin mixing to transfer predominantly triplet character Feshbach molecules to the ro-vibrational ground state of the singlet electronic ground potential, $X^1\Sigma$. The vertical arrows are placed at the respective Condon points of the up and down transitions. (**B**) Normalized Raman laser intensities versus time for the round-trip STIRAP pulse sequence. We performed a 4 μs STIRAP transfer each way using a maximum Rabi frequency of $2\pi \times 7$ MHz for the downward transition (blue line) and a maximum Rabi frequency of $2\pi \times 4$ MHz for the upward transition (red line). (**C**) STIRAP lineshape. The number of Feshbach molecules returned after a round-trip STIRAP transfer is plotted as a function of the two-photon Raman laser detuning. The error bars represent the standard deviation of the measurements. The round-trip data were taken at the time indicated by the black arrow in (B). The red data points show the remaining Feshbach molecule number when only one-way STIRAP is performed [at the time indicated by the red arrow in (B)], where all Feshbach molecules are transferred to the ground state and are dark to the imaging light. The initial Feshbach molecule number is $3.3(4) \times 10^4$ (red solid line), and the number after round-trip STIRAP is 2.3×10^4. The round-trip efficiency is 69%, which suggests the one-way transfer efficiency is 83% and the number of the absolute ground-state polar molecules is 2.7×10^4. Error bars represent 1 SD error in the molecule number.

Stark Spectroscopy: Dipole Moment Determination (Singlet)

Fig. 6. Stark spectroscopy of the singlet $v = 0$ molecules. The bottom panel shows the Stark shift of the rovibrational ground-state of the singlet potential ($v = 0$, $N = 0$ of $X^1\Sigma$), and the top panel shows the shift of the $v = 0$, $N = 2$ state. The systematic error in the applied electric field is 3% (horizontal error bars). The level difference between $N = 0$ and $N = 2$ is 6.6836(5) GHz, which yields a rotational constant B of 1.1139(1) GHz. Given the measured B, the fit of the Stark shift (line in lower panel) gives a permanent electric dipole moment of 0.566(17) D. The theory curves for $N = 2$ for different $|m_N\rangle$ projections (lines in upper panel) are calculated using the measured B and the dipole moment derived from the $N = 0$ fit.
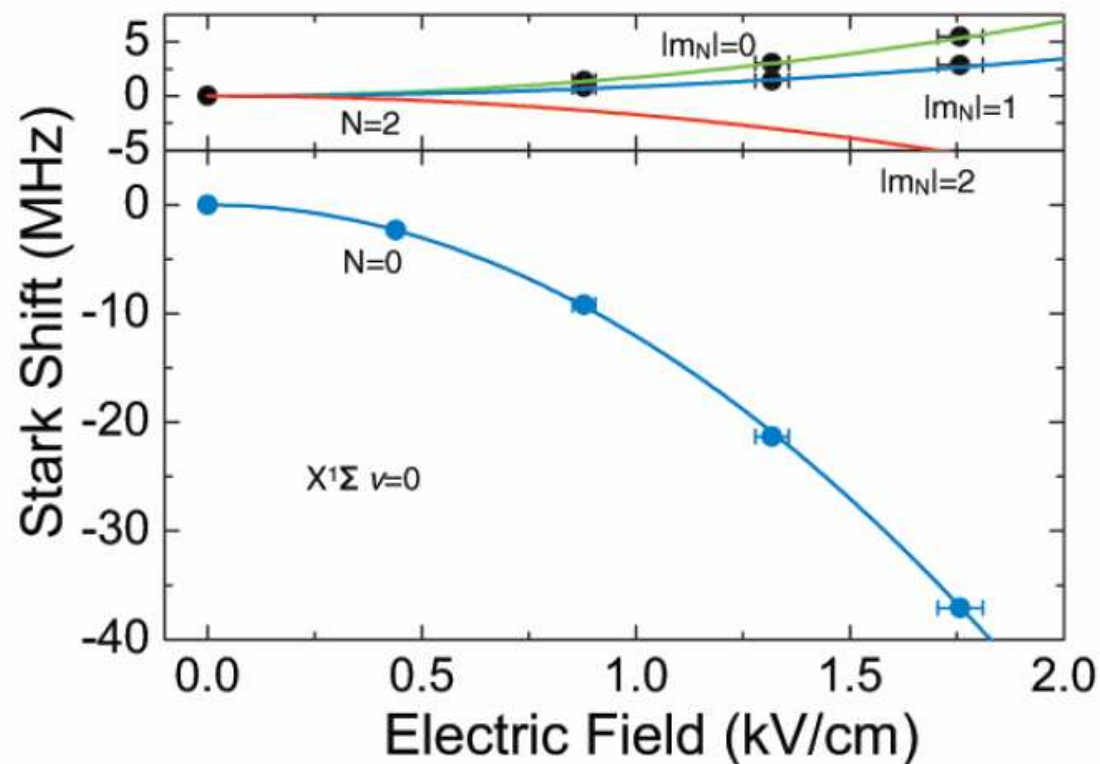
Lifetime of KRb Molecules
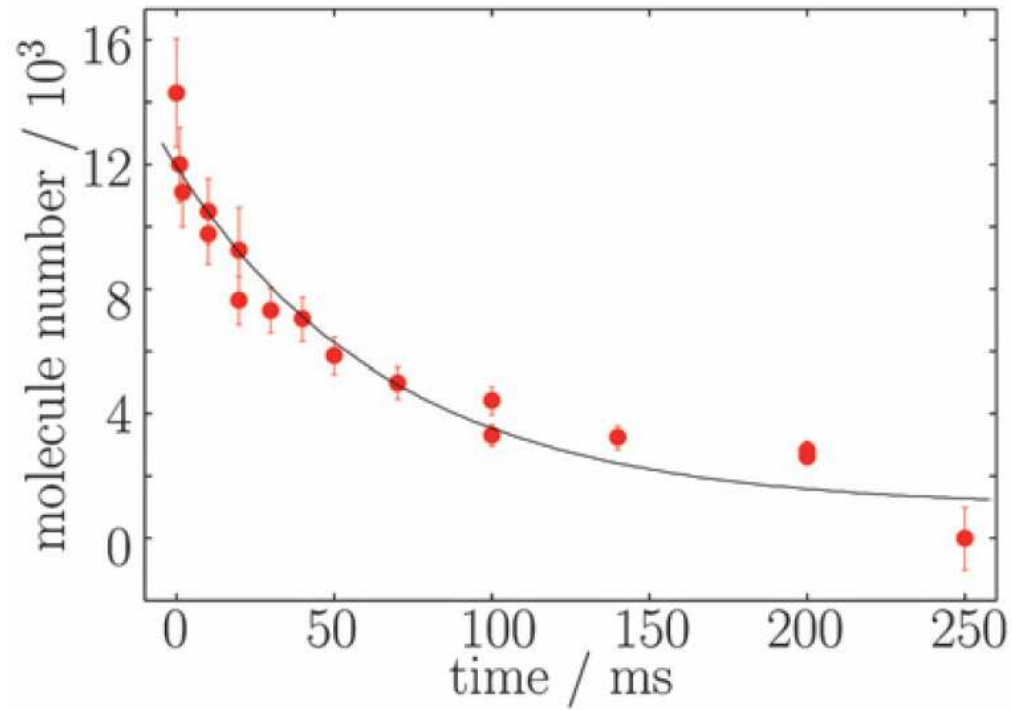
Fig. 6 Lifetime of ground-state polar molecules in the optical dipole trap. We extract $\tau = 70(8)$ ms.

KRb Molecules in Ground Hyperfine states - I

The lowest energy electronic potential for heteronuclear bialkali molecules, such as KRb molecules, is a spin singlet state ($X^1\Sigma^+$) that has zero electronic angular momentum and spin. Therefore, the hyperfine structure reduces to a nuclear substructure due to the nuclear magnetic moments of the constituent atoms. Fig-
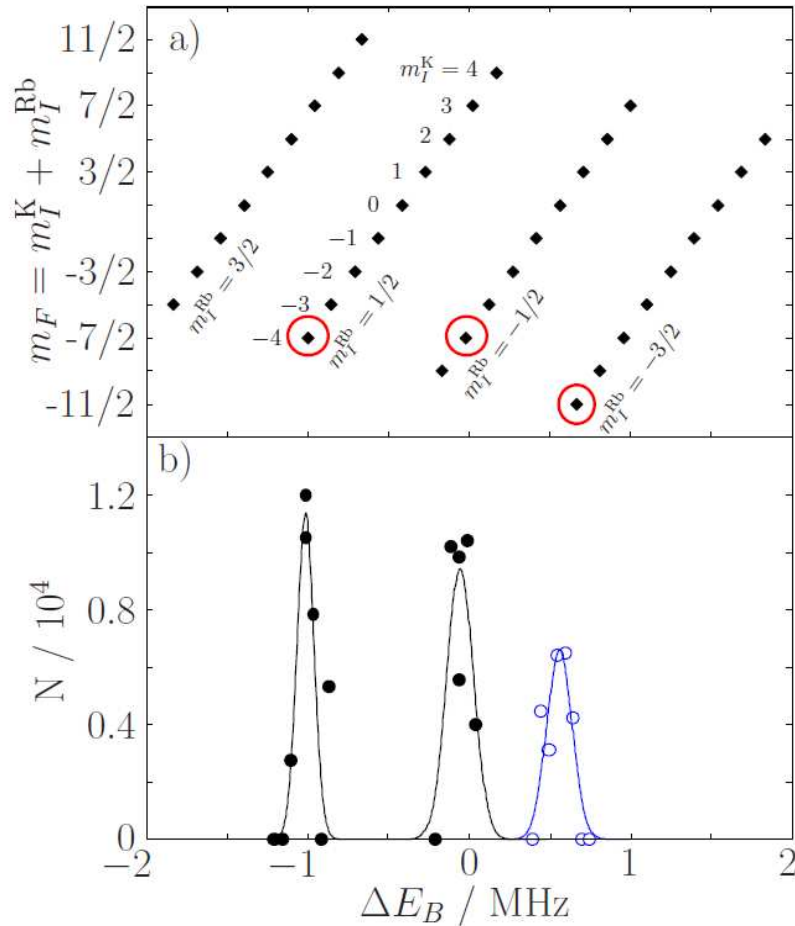
FIG. 1: (**color online**) (a) Hyperfine structure of $^{40}\mathrm{K}^{87}\mathrm{Rb}$ molecules in their rotational ($N = 0$) and vibrational ($v = 0$) ground state of the electronic ground molecular potential ($X^1\Sigma^+$) at $B = 545.9\,\mathrm{G}$. The rovibrational ground state splits into to 36 hyperfine states corresponding to the different projections of the nuclear spins of the constituent atoms $^{40}\mathrm{K}$ ($I^K = 4$) and $^{87}\mathrm{Rb}$ ($I^{Rb} = 3/2$). The circled quantum states can be directly populated via STIRAP in our experiment. (b) Optical two-photon spectroscopy of the rovibrational ground-state manifold of $^{40}\mathrm{K}^{87}\mathrm{Rb}$ molecules (see text). We observe three hyperfine states, which are characterized by $m_F = -7/2$ (black points) and $m_F = -11/2$ (blue open points). Here, ΔE_B is the binding energy of the hyperfine states at $B = 546.9\,\mathrm{G}$ relative to the binding energy of the rovibrational ground state at zero magnetic field. Negative ΔE_B indicates a more deeply bound state and positive ΔE_B a less deeply bound state

KRb Molecules in Ground Hyperfine states - II
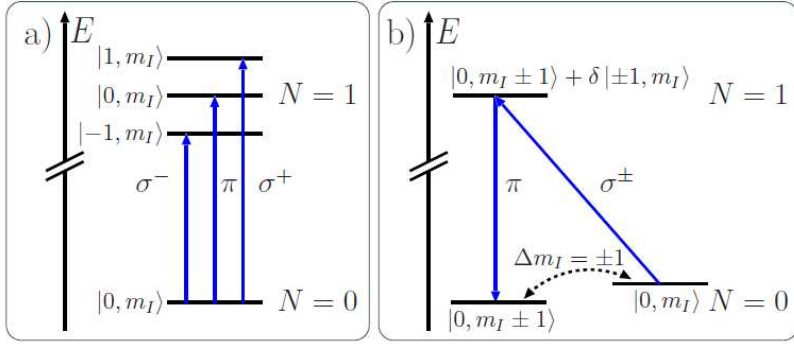
FIG. 2: (**color online**) (a) Electric dipole transitions between the rotational ground state $N = 0$ and the first rotationally excited state $N = 1$. To first order, electric dipole transitions will keep the hyperfine state unchanged $\Delta m_I = 0$. (b) Controlling the hyperfine state within the rotational and vibrational ground state. The interaction between the nuclear electric-quadrupole moment of ^{40}K / ^{87}Rb and the electric field gradient of the electronic cloud mixes quantum states with different nuclear spin quantum number $m_I^{K/Rb}$ in $N = 1$. This allows the implementation of a two-photon scheme to transfer molecules between different hyperfine states within the rovibrational ground state ($\Delta m_I^{K/Rb} = \pm 1$). To simplify the notation, we abbreviate $|N, m_N, m_I^K, m_I^{Rb}\rangle$ by N $|m_N, m_I\rangle$. Here m_I refers to the changing hyperfine quantum number m_I of K or Rb.

main state	admixed state	$|\delta_{th}|^2$	$|\delta_{exp}|^2$
$|1\ 0\ -4\ 3/2\rangle$	$|1\ 1\ -4\ 1/2\rangle$	0.045	≈ 0.1
$|1\ 0\ -3\ 1/2\rangle$	$|1\ 1\ -4\ 1/2\rangle$	0.0085	≈ 0.0064

TABLE I: Mixing of different hyperfine states in the rotationally excited state $N = 1$ at $B = 545.9$ G. We compare the theoretically calculated admixture $|\delta_{th}|^2$ to the experimentally measured admixture $|\delta_{exp}|^2$.
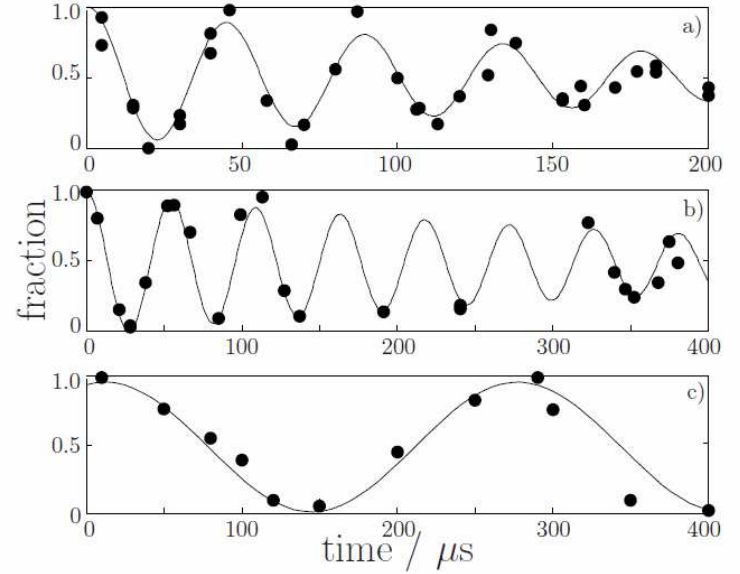
FIG. 3: Rabi oscillations on a (a) hyperfine preserving microwave transition $|0, 0, -4, 1/2\rangle \rightarrow |1, 1, -4, 1/2\rangle$ (b) Rb hyperfine changing transition $|0, 0, -4, 1/2\rangle \rightarrow |1, 0, -4, 3/2\rangle + \delta|1, 1, -4, 1/2\rangle$ (c) K hyperfine changing transition $|0, 0, -4, 1/2\rangle \rightarrow |1, 0, -3, 1/2\rangle + \delta|1, 1, -4, 1/2\rangle$. Note the different time axis in panel (a). The microwave power was reduced by a factor of 4 for the data in (a) resulting in an effective decrease of the Rabi frequency by a factor of 2.

And now for something completely different

Cold molecules from hot molecules

Buffer Gas Cooling: Harvard

Principle and Key Innovations

Universal technique for atoms and molecules

Uses magnetic trapping, so requires unpaired valance electrons

Cooling by collision with He buffer gas

Cooling happens within the trap volume, so the trap loading is dissipative

Large numbers loaded at X00 mK temperatures

Evaporative cooling beyond temperatures below the X00 mK

BEC with Na atoms recently realized with this techniques

Molecule cooling -> Work in progress

Buffer Gas Cooling: Harvard
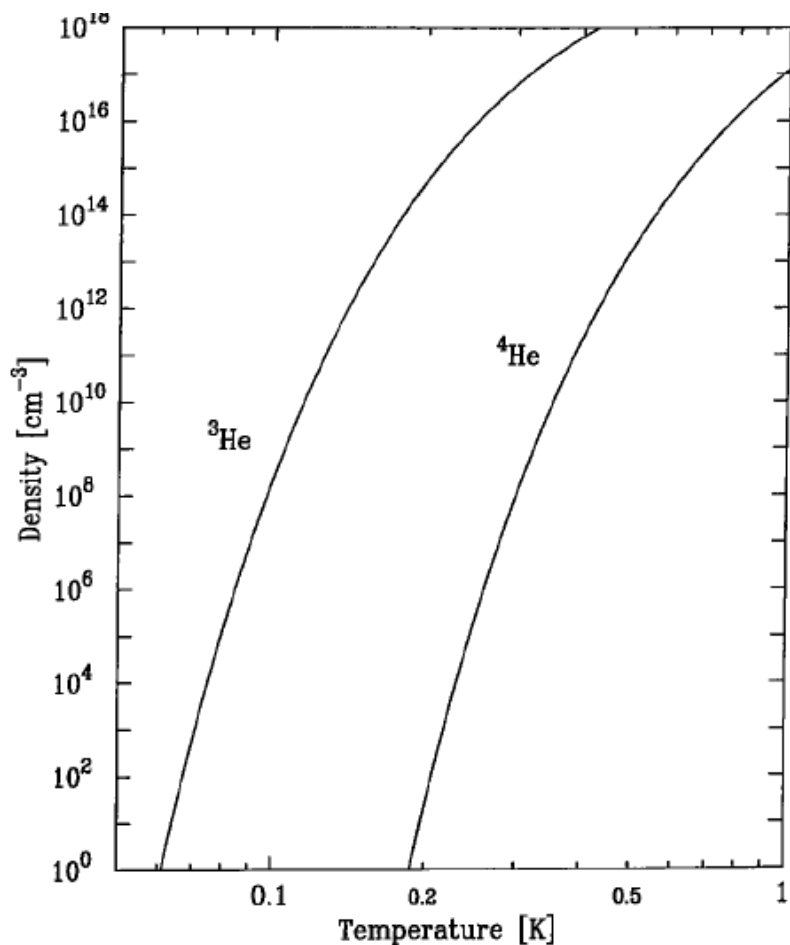
Fig. 2. Low-temperature number density curves of ^{3}He and ^{4}He. Note that the minimum number density of about 10^{16} cm^{-3} required for buffer-gas loading is attained at 240 mK in ^{3}He and 800 mK in ^{4}He.
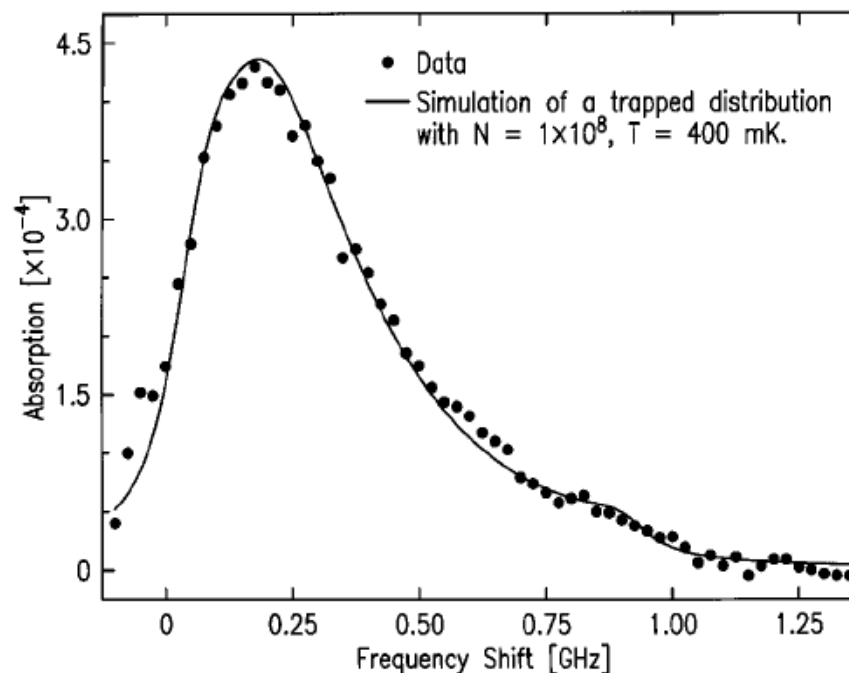
Fig. 15. Fit of CaH spectrum to a thermal distribution of trapped molecules. Data were taken with a 3 T trap depth and a cell temperature of 300 mK before ablation, and were integrated from 200 ms to 300 ms after the ablation pulse. This fit determines the number and the temperature of trapped CaH molecules to be $N = 1 \times 10^8$ and $T = 400$ mK.

Buffer Gas Cooling: Harvard
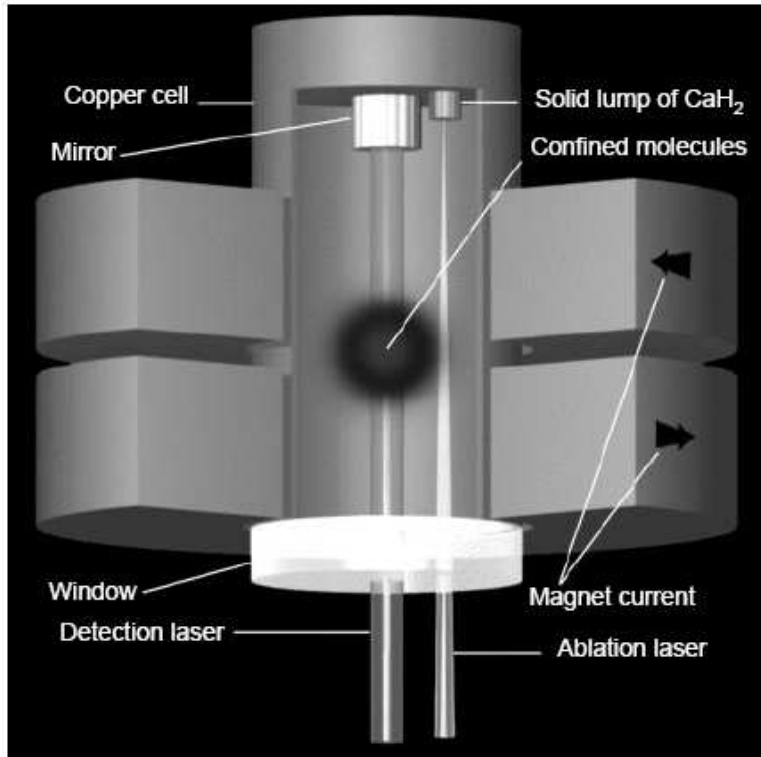
Copper cell — Solid lump of CaH_2
Mirror — Confined molecules
Window — Magnet current
Detection laser — Ablation laser

Universal technique for atoms and molecules

Uses magnetic trapping, so requires unpaired valance electrons

Cooling by collision with He buffer gas

Cooling happens within the trap volume

Species	State	Buffer gas	T [mK]	κ	$\langle\mu\rangle$ [μ_B]	$\mathcal{H}_{edge}$ [T]	η	N
^{52}Cr	$^7S_3$	^3He	300	~ 10	~ 6	0.7	~ 9	$\sim 10^{11}$
		^4He	1,400	~ 8	~ 6	2.4	~ 7	$\sim 10^{11}$
$^{151,153}Eu$	$^8S_{7/2}$	^3He	250	~ 26	~ 7	0.6	~ 11	$\sim 10^{12}$
		^4He	800	~ 20	~ 7	2.0	~ 12	$\sim 10^{12}$
$^{40}Ca^1H$	$^2\Sigma^+$	^3He	400	~ 8	~ 1	3.0	~ 5	$\sim 10^8$

Buffer Gas Cooling: NH
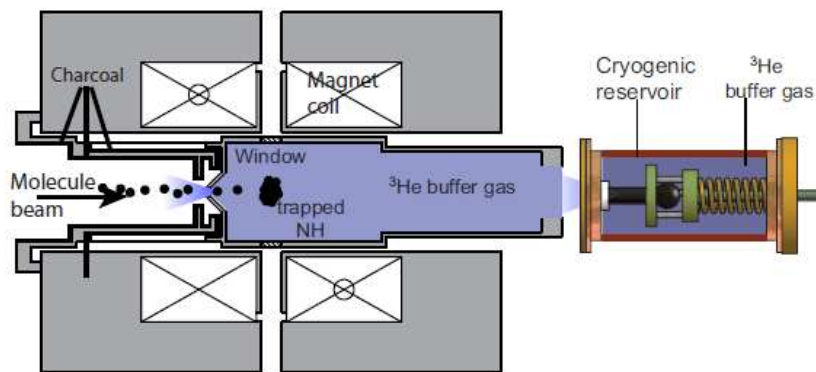
Figure 2. Schematic drawing of the experimental apparatus. The molecule beam propagates through the vacuum space to enter the cell, housed in the bore of the trapping magnet. Buffer gas, supplied by the pulsed reservoir, fills the cell and allows the molecules to thermalize to the cell temperature. The molecules are detected with laser light that passes through window ports in the magnet midplane.
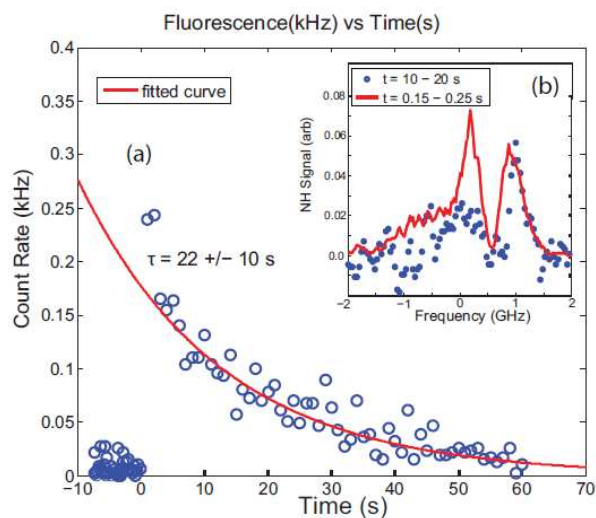
Figure 4. (a)Temporal decay of molecule fluorescence. The fit is performed after 10 s to reduce the effect of cell cooling on the lifetime. (b) NH spectra taken at different time intervals. The spectrum recorded between 0.15 s and 0.25 after the triggering of the molecular beam is given by the red trace. The spectrum recorded between 10 s and 20 s is shown by the blue circles. The fluorescence intensities of the two spectra are scaled for comparison - the signal at 10 s is 300 times weaker than at 0.15 s. The difference in the relative heights of the spectral features is currently unexplained.
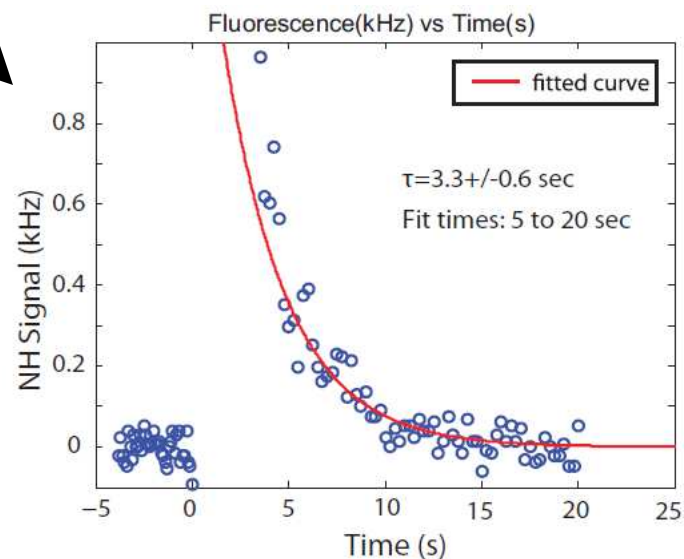
Time domain measurements

The $v = 1 \rightarrow 0$ radiative lifetime of $NH(X^3\Sigma^-, v = 1, N = 0)$ is determined to be $\tau_{rad,exp.} = 37.0 \pm 0.5_{stat}{}^{+2.0}_{-0.8syst}$ ms, corresponding to a transition dipole moment of $|\mu_{10}| = 0.0540^{+0.0009}_{-0.0018}$ D. To achieve sufficiently long observation times, $NH(X^3\Sigma^-, v = 1)$ radicals are magnetically trapped using helium buffer-gas loading. The rate constant for background helium-induced collisional quenching was determined to be $k_{v=1} < 3.9 \times 10^{-15}$ cm^3 s^{-1}, which yields the quoted systematic uncertainty on $\tau_{rad,exp.}$. With a new *ab initio* dipole moment function and a Rydberg-Klein-Rees potential, we calculate a lifetime of 36.99 ms, in agreement with our experimental value.

Fluorescence(kHz) vs Time(s)
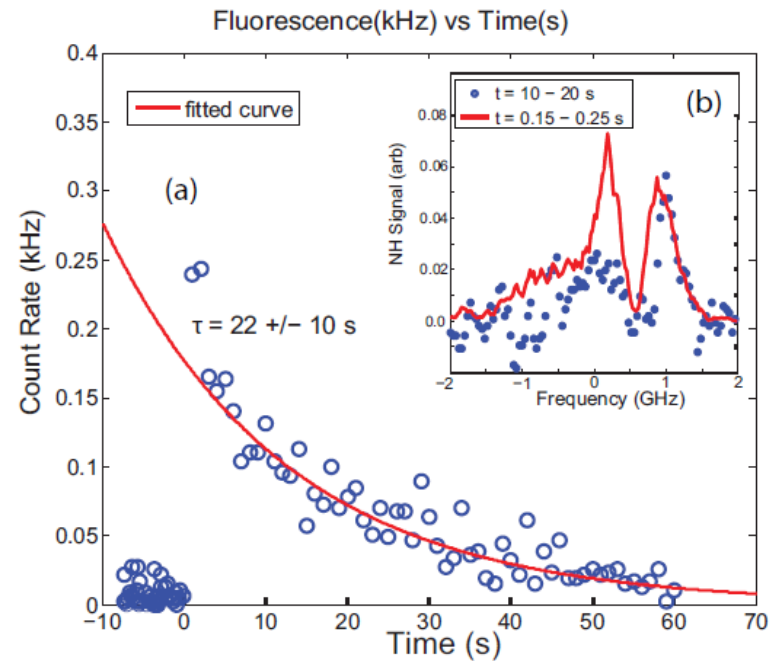
Contents

Metastable helium (^{4}He*) is buffer-gas cooled

magnetically trapped

evaporatively cooled to quantum degeneracy

10^{11} atoms are initially trapped

condensation at a critical temperature of 5 μK

threshold atom number of 1.1×10^6
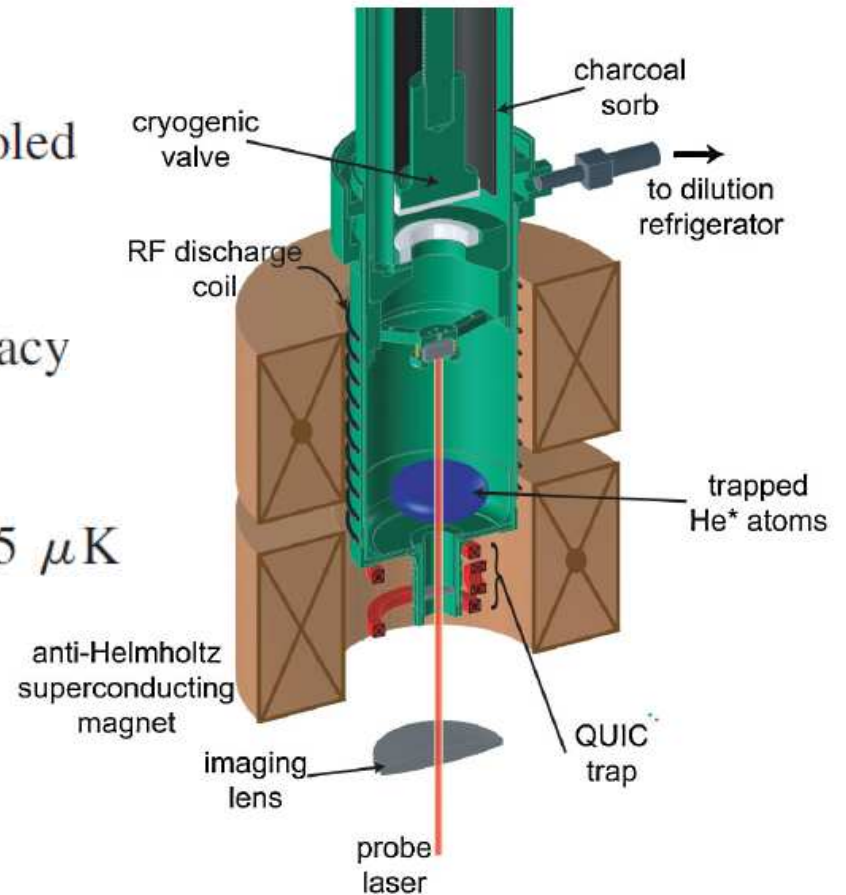
FIG. 1 (color).   Schematic of the experimental apparatus.

Orifice

Oven

Test chamber

L > d

Pump   Pump

Conventional oven beam

Skimmer

Nozzle

Test chamber

L << d

Pump   Pump   Pump

Supersonic nozzle beam
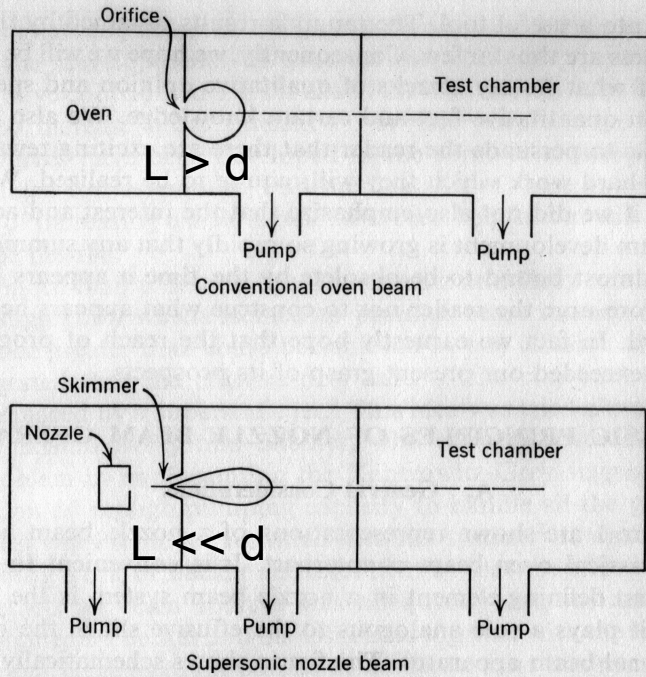
Fig. 1. Schematic representation of oven beam and nozzle beam systems. Th closed curves downstream of the slit and skimmer represent the relative intensit distributions.

M = 0

M = 10

M = 25

Relative intensity

Relative velocity, $v / \left(\frac{2kT_0}{m} \right)^{\frac{1}{2}}$
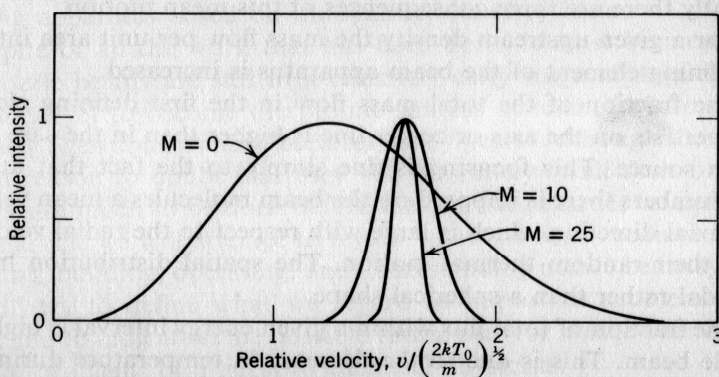
Fig. 2. Theoretical axial velocity distributions for nozzle source beams of mon atomic gases with Mach number at the skimmer entrance as indicated. The distribu tion for an oven beam is also shown ($M = 0$).

In addition, U_{rot} and U_{vib} also go down in temperature because the cross sections for

el. ($U_{tr} \rightarrow U_{tr}$) >> inel.($U_{rot} \rightarrow U_{tr}$) >> inel.($U_{vib} \rightarrow U_{trans}$)

$N = N_0 \exp\left(-\frac{m}{2kT_0} v^2\right)$

$N = N_0 \exp\left(-\frac{m}{2kT}(v_z - u)^2\right)$
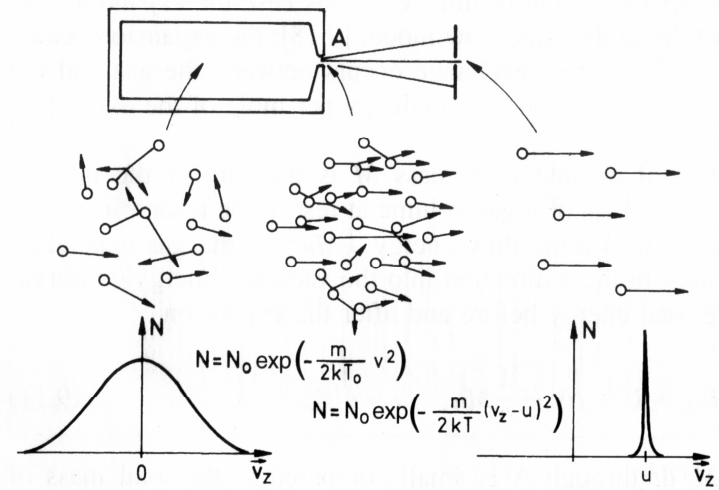
$$v_\infty = \sqrt{\frac{2R}{W}\left(\frac{\gamma}{\gamma-1}\right)T_0} ; \qquad \frac{v_{\infty,\gamma=11/9}}{v_{\infty,\gamma=5/3}} \cong 1.5$$

$$M = v_{jet}/a$$

$$a = \sqrt{\gamma R T / W}$$

$$\frac{T}{T_0} = \left(1 + \frac{\gamma-1}{2}M^2\right)^{-1}$$

$\gamma = 5/3$

Mach Number (M) vs axial dist. / nozzle diameter

T (K) vs Mach Number (M)
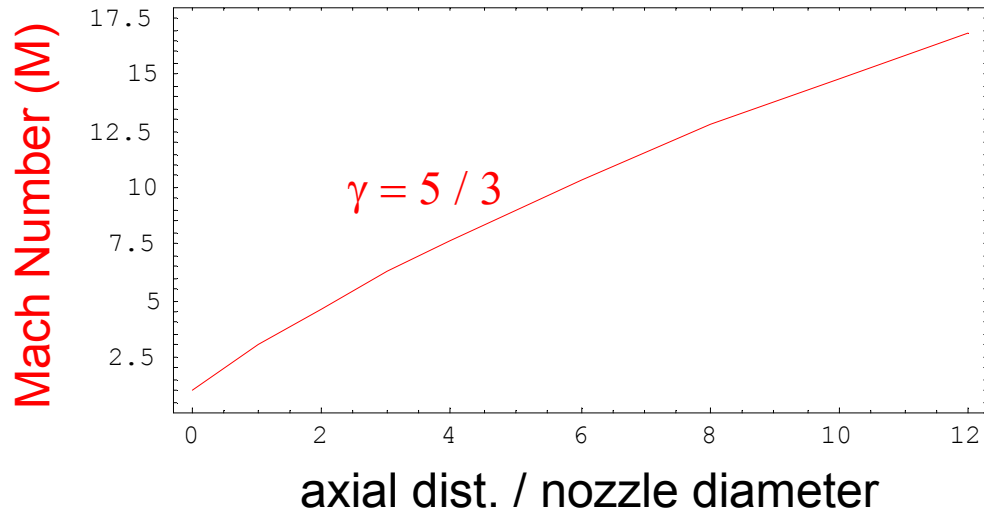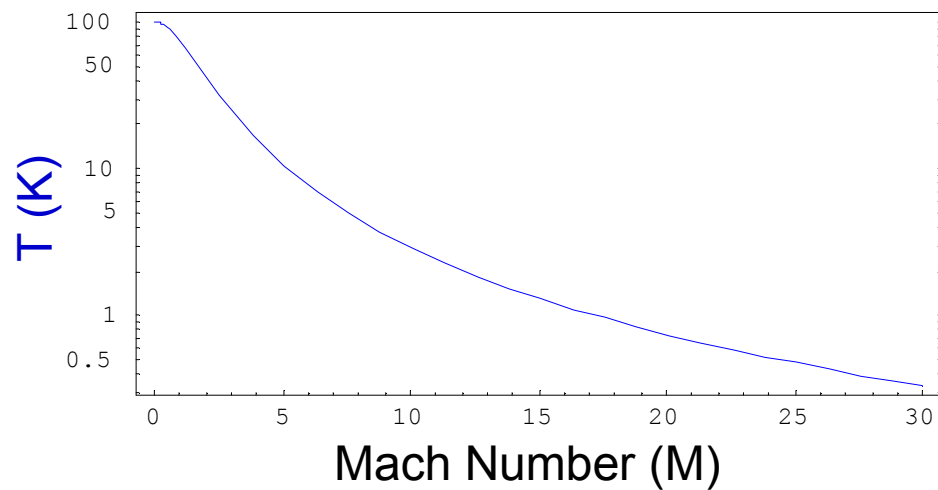
equilibrium position for a
dipole in an electric field

$\overset{\cup}{E}$

$+$

$\overset{\cup}{\mu}$

$-$

$+$
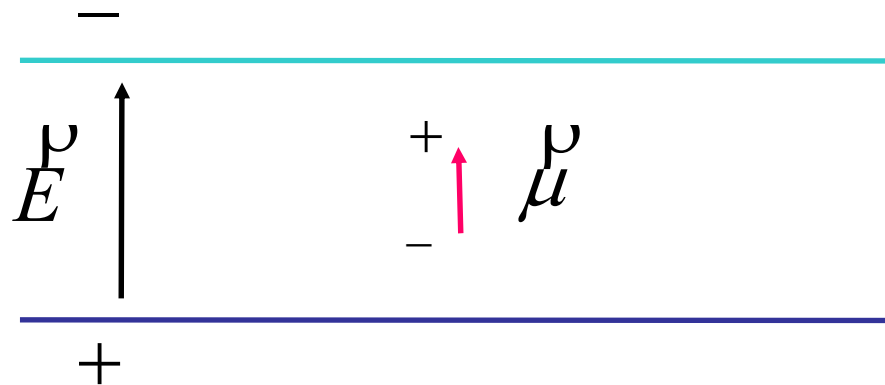
probable position for a
rotating dipole in an
electric field
axis of rotation is perp.
to the dipole and electric
field.

$\overset{\cup}{E}$

$-$

$\overset{\cup}{\mu}$

$+$

$+$
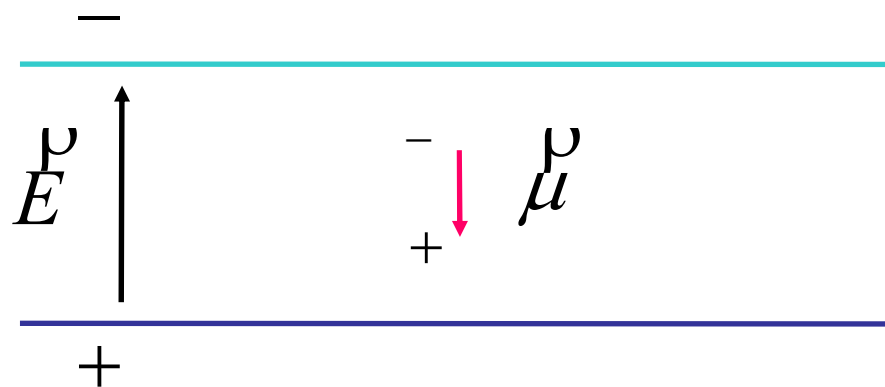
J=0, M=0 case
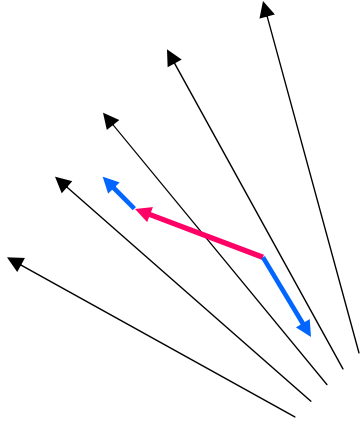
High-field seeker

J=1, M=0: small
E field case
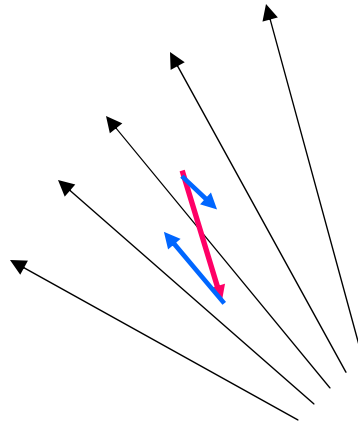
Low-field seeker

J=1, M=0: large
E field case
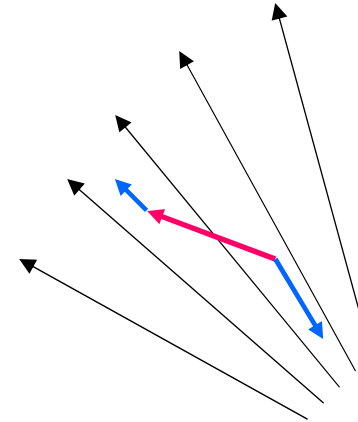
therefore, this limit
gives a high-field seeker

$-$

E

$F-$

J

$F+$ μ

$+$

$+$
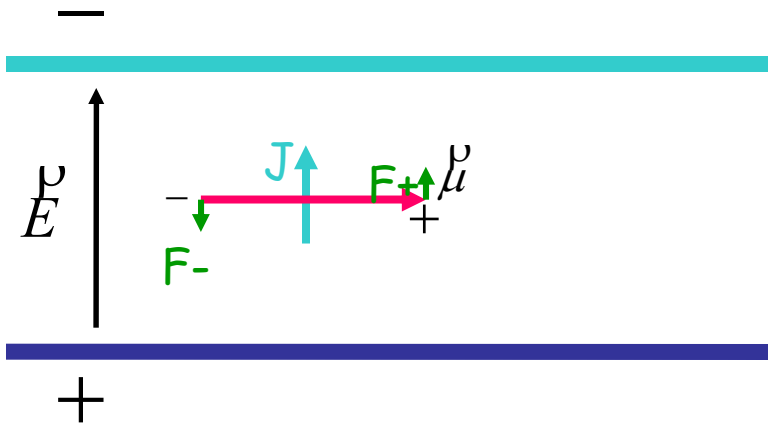
J = 1, M = +1 & M = -1 cases

...are both high-field
seeking and degenerate

J
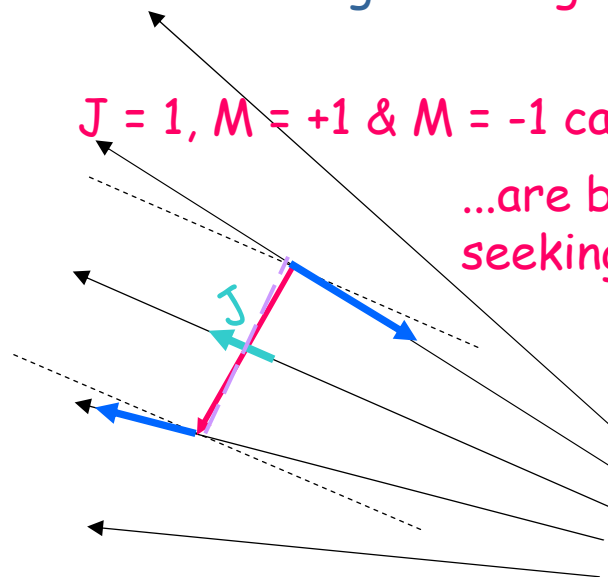
Stark Energy levels for the Rigid Rotor Dipolar Molecules
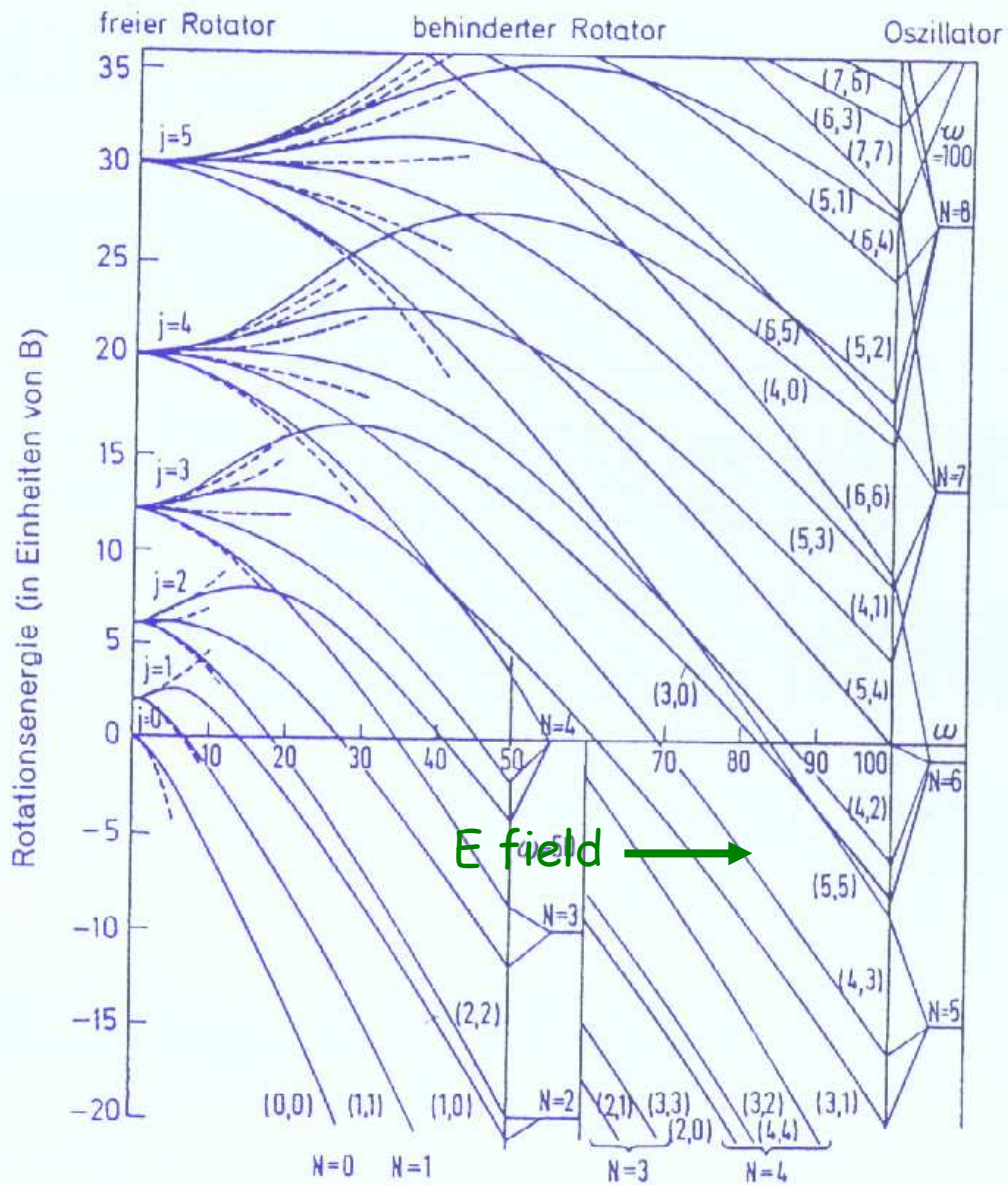
Stark Deceleration
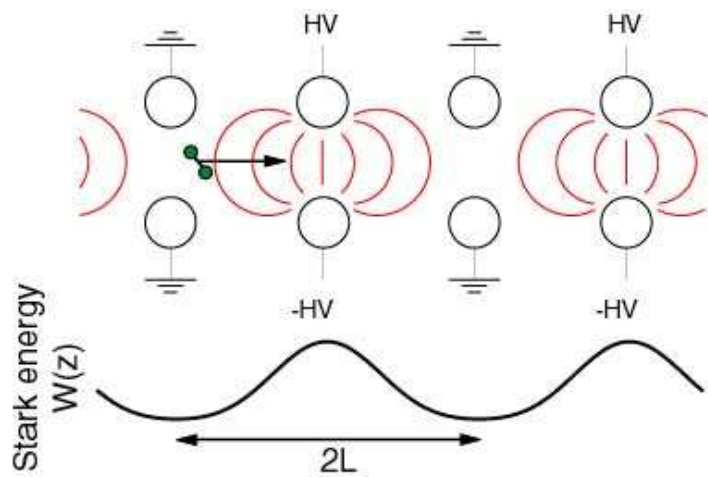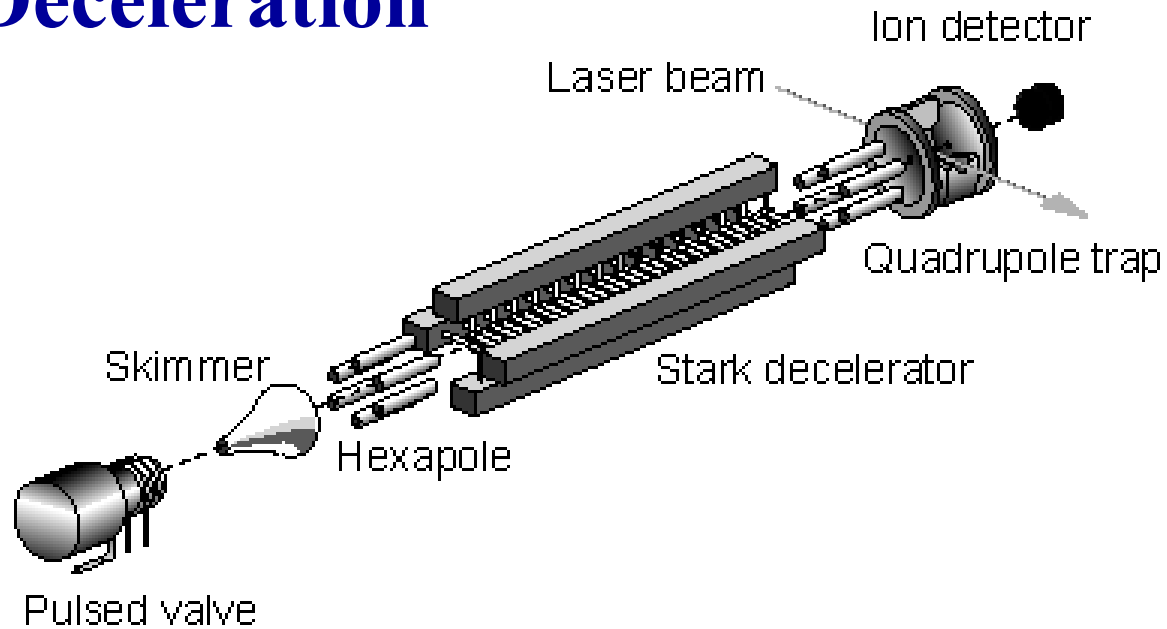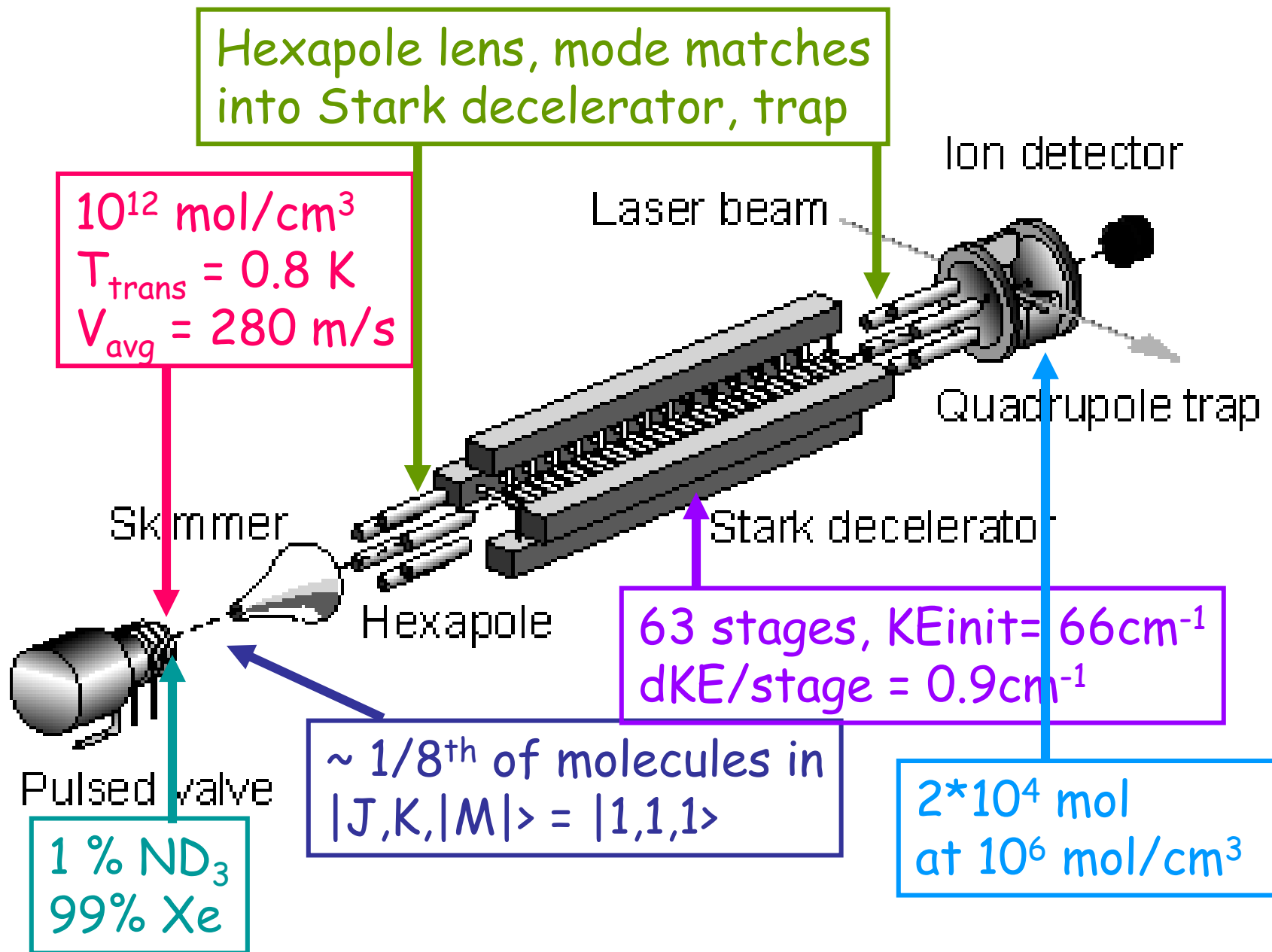
Hexapole lens, mode matches
into Stark decelerator, trap

10^{12} mol/cm^3
T_{trans} = 0.8 K
V_{avg} = 280 m/s

Laser beam

Ion detector

Quadrupole trap

Skimmer

Stark decelerator

Hexapole

63 stages, KEinit= 66cm^{-1}
dKE/stage = 0.9cm^{-1}

~ 1/8th of molecules in
$|J,K,|M|\rangle = |1,1,1\rangle$

Pulsed valve

1 % ND$_3$
99% Xe

$2*10^4$ mol
at 10^6 mol/cm^3
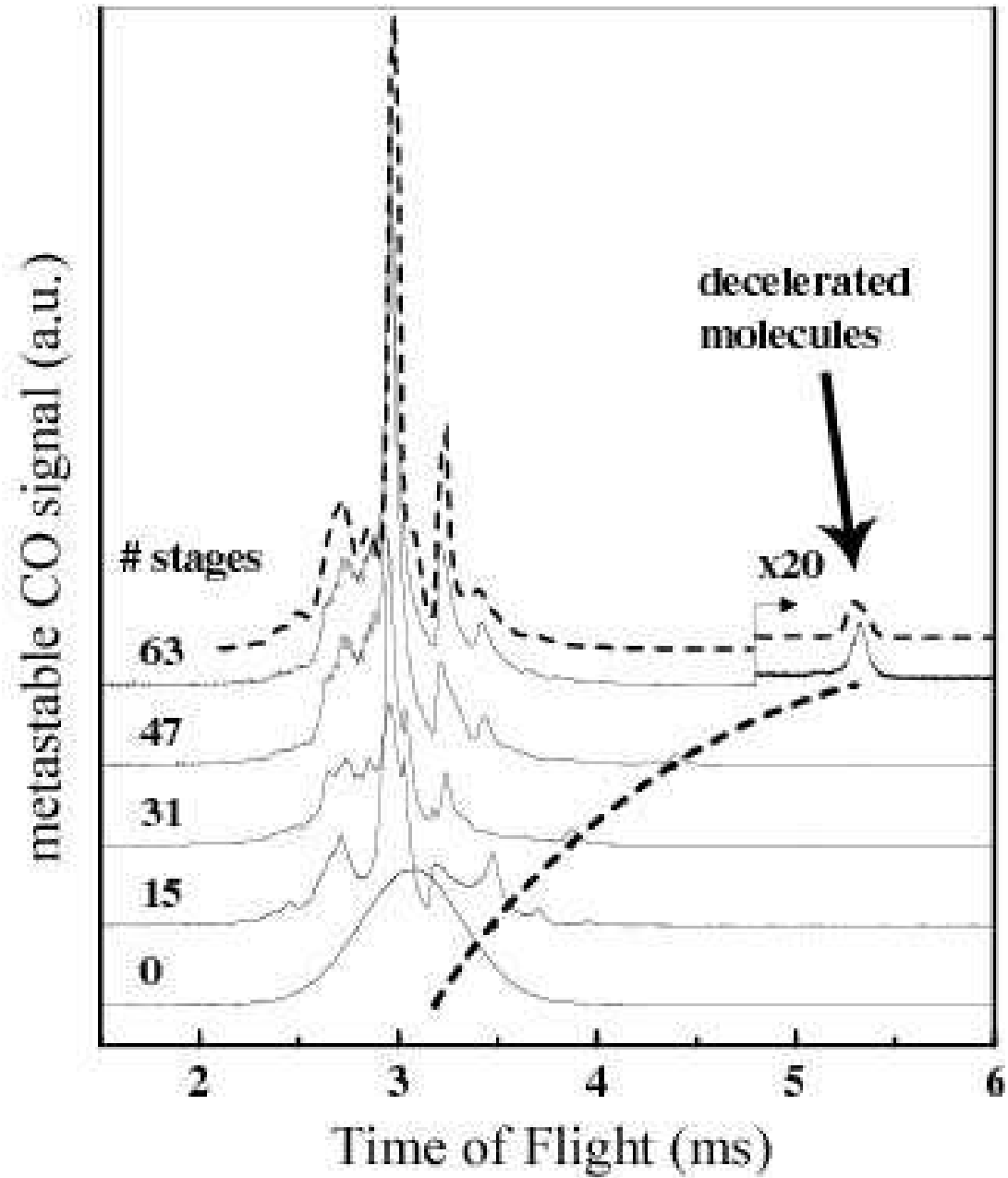
Loading
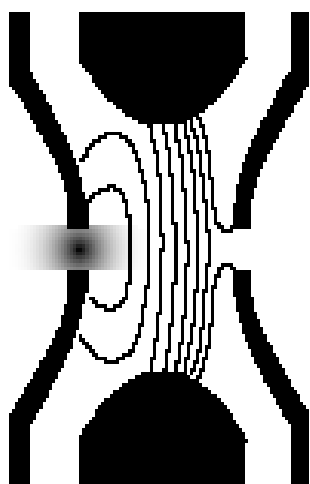
Trapping

Trap decay time
1/e => 240ms

10 kV 12 kV -400 V

0 V 12 kV -400 V

Energy (cm^{-1})

Position (mm)

ND$_3$ Density (a.u.)

Trap on

t(s)

t (ms)
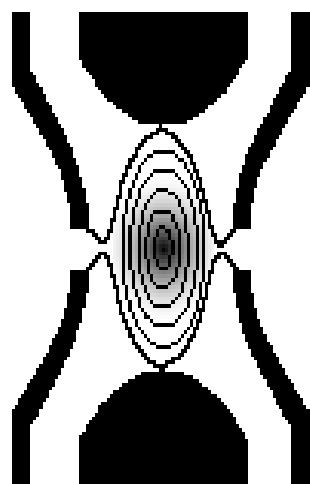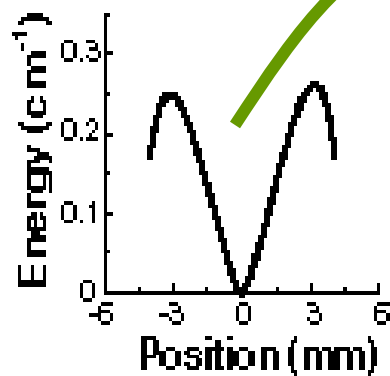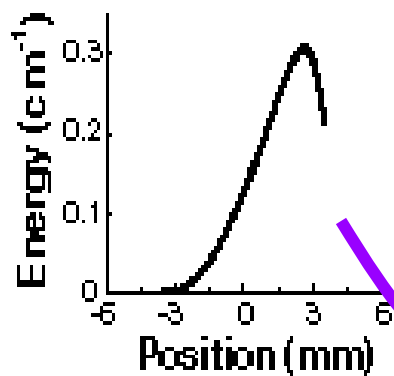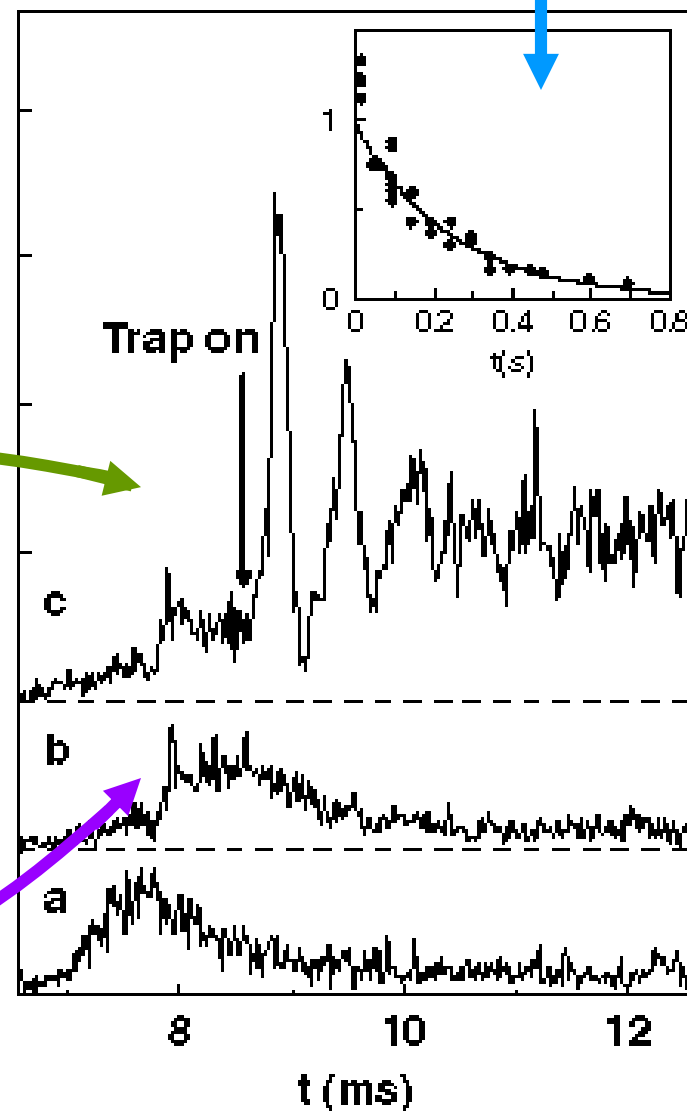
Heating Rates for "State Selected Molecules"

TABLE I. Pumping rates due to blackbody radiation at two different temperatures, out of the specified initial state, for a number of polar molecules.

System	Initial state	Pumping rate (s^{-1})	
		295 K	77 K
OH/OD	$X^2\Pi_{3/2}, J = \frac{3}{2}$	0.49/0.16	0.058/0.027
NH/ND	$a^1\Delta, J = 2$	0.36/0.12	0.042/0.021
NH/ND	$X^3\Sigma^-, N = 0, J = 1$	0.12/0.036	0.025/0.0083
NH_3/ND_3	$\tilde{X}^1A_1', J = 1, |K| = 1$	0.23/0.14	0.019/0.0063
SO	$X^3\Sigma^-, N = 0, J = 1$	0.01	$<10^{-3}$
^{6}LiH/^{6}LiD	$X^1\Sigma^+, J = 1$	1.64/0.81	0.31/0.11
CaH/CaD	$X^2\Sigma^+, N = 0, J = \frac{1}{2}$	0.048/0.063	$0.0032/<10^{-3}$
RbCs	$X^1\Sigma^+, J = 0$	$<10^{-3}$	$<10^{-3}$
KRb	$X^1\Sigma^+, J = 0$	$<10^{-3}$	$<10^{-3}$
CO	$a^3\Pi_{1,2}, J = 1, 2$	0.014/0.014	$<10^{-3}/<10^{-3}$

DC and AC trap configurations for Stk. Decel.
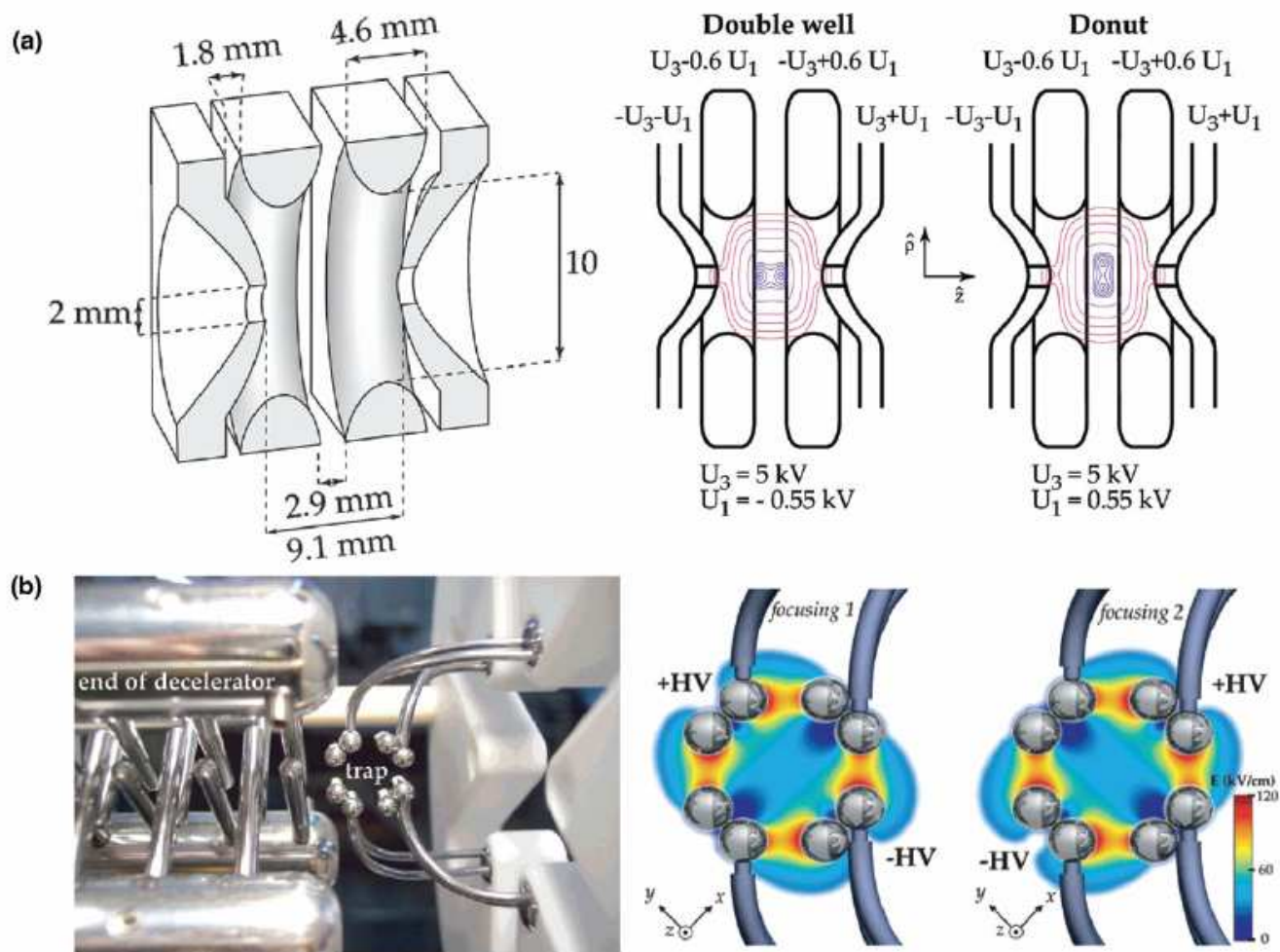
Figure 9. Electric trapping of polar molecules. (a) Electrostatic trap for confining low-field seeking molecules in various trapping geometries. (b) Linear AC trap for high-field and low-field molecules, showing the two electric field configurations used for electrodynamic trapping. Adapted with permission from [80] and [181]. Copyright © (2007) American Chemical Society; and (2006) American Physical Society, respectively.

Molecules in E Fields

cm^{-1}

50

low field seeking state

high field seeking state

lowest lying rotational states of formaldehyde and their Stark shifts

kV/cm

50 100 150

E [kV/cm]

100
80
60
40
20
0

y[mm]

2

0

-2

+   −

−   +

-2   0   2

x [mm]
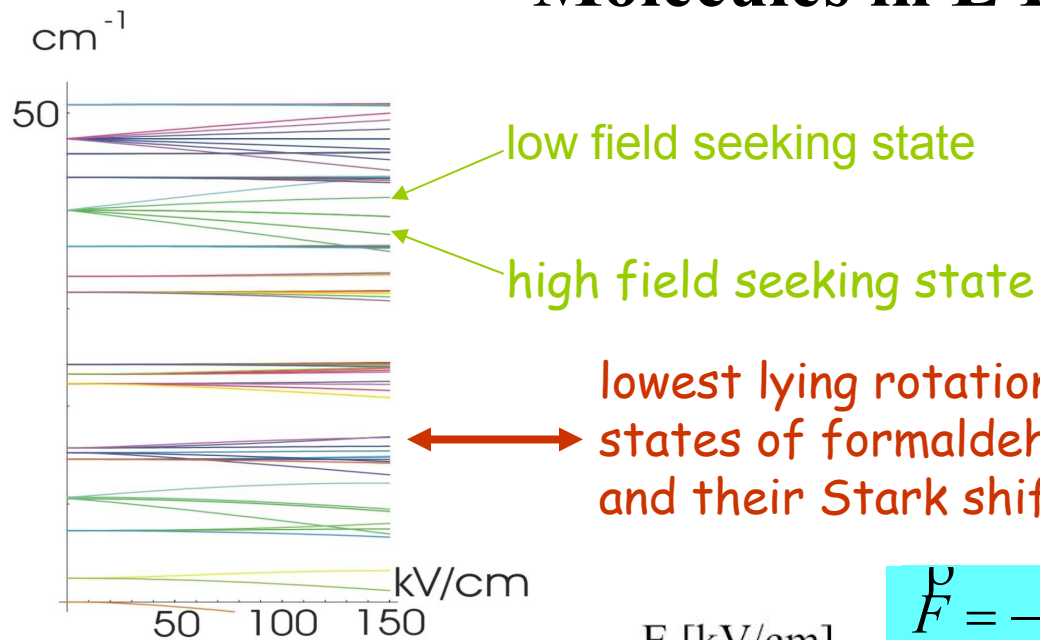
$$\vec{F} = -\nabla W_S(E)$$

J=1, M=0: small E field case
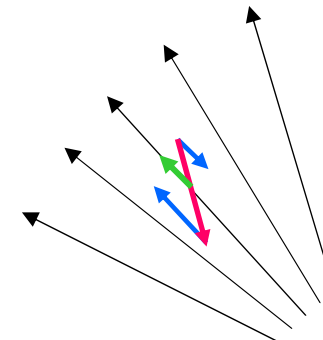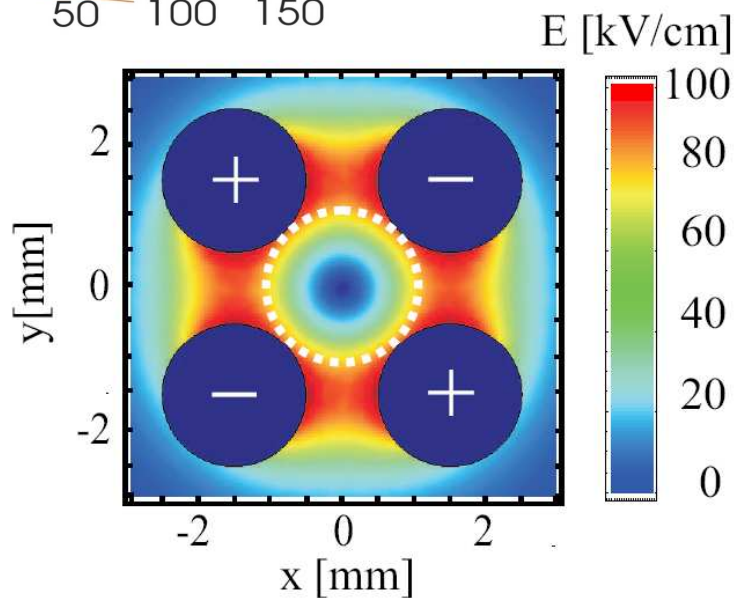
low field seeker

J=0, M=0 case
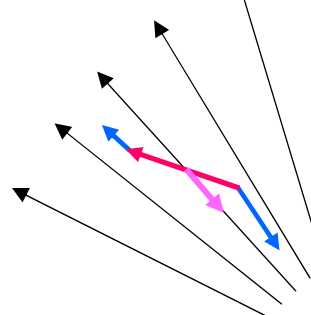
high field seeker

"Filtering the Tail"

$$f(v)dv = \frac{1}{\sqrt{\pi}\alpha}\exp(-\frac{v^2}{\alpha^2})dv$$

$$f(v_z)dv = \frac{2}{\sqrt{\pi}\alpha^2}v_z\exp(-\frac{v_z^2}{\alpha^2})dv_z$$

slow molecules

quadrupole

diff. pumping

effusive source

fast molecules
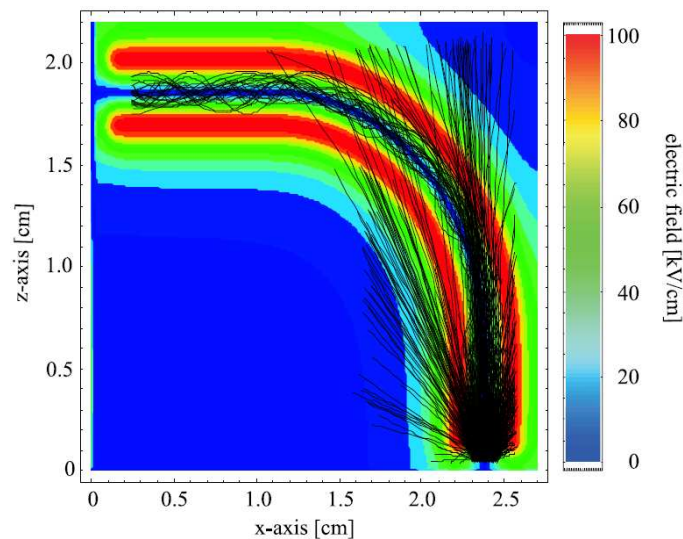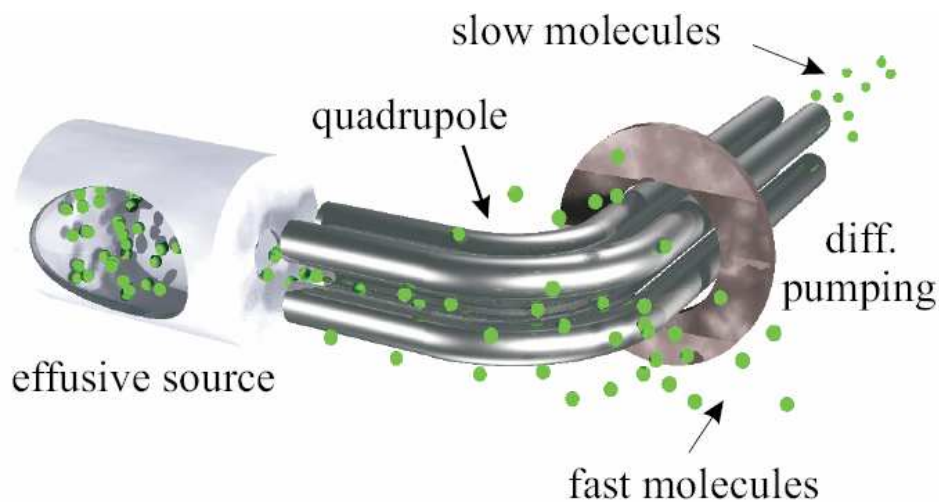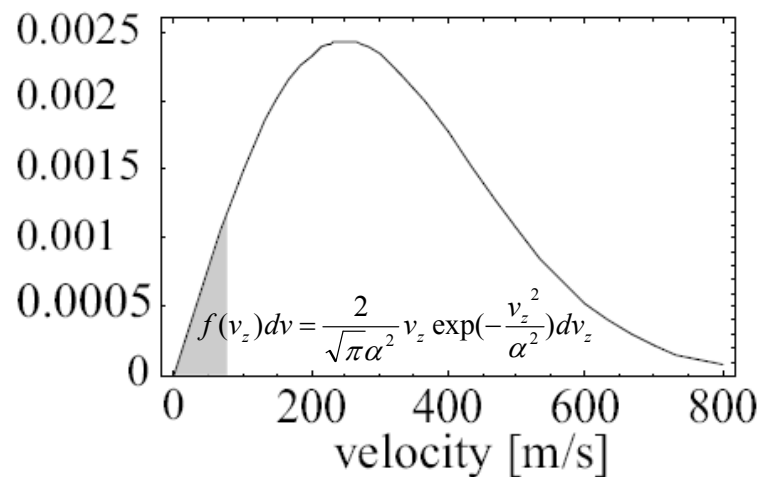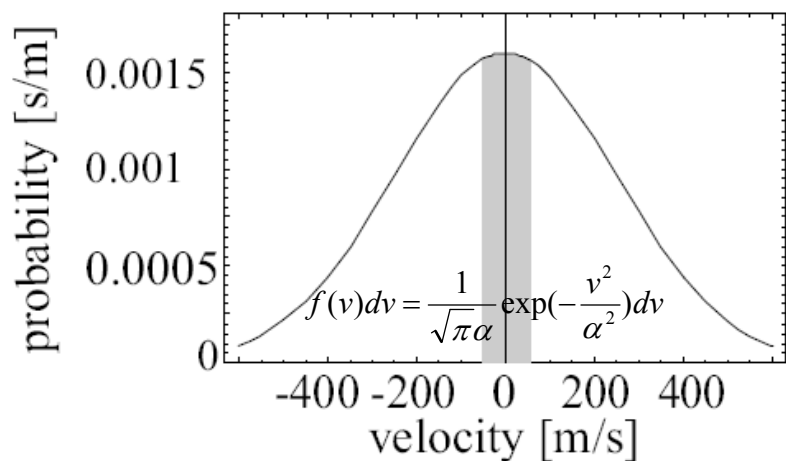
The basic filtering experimental setup
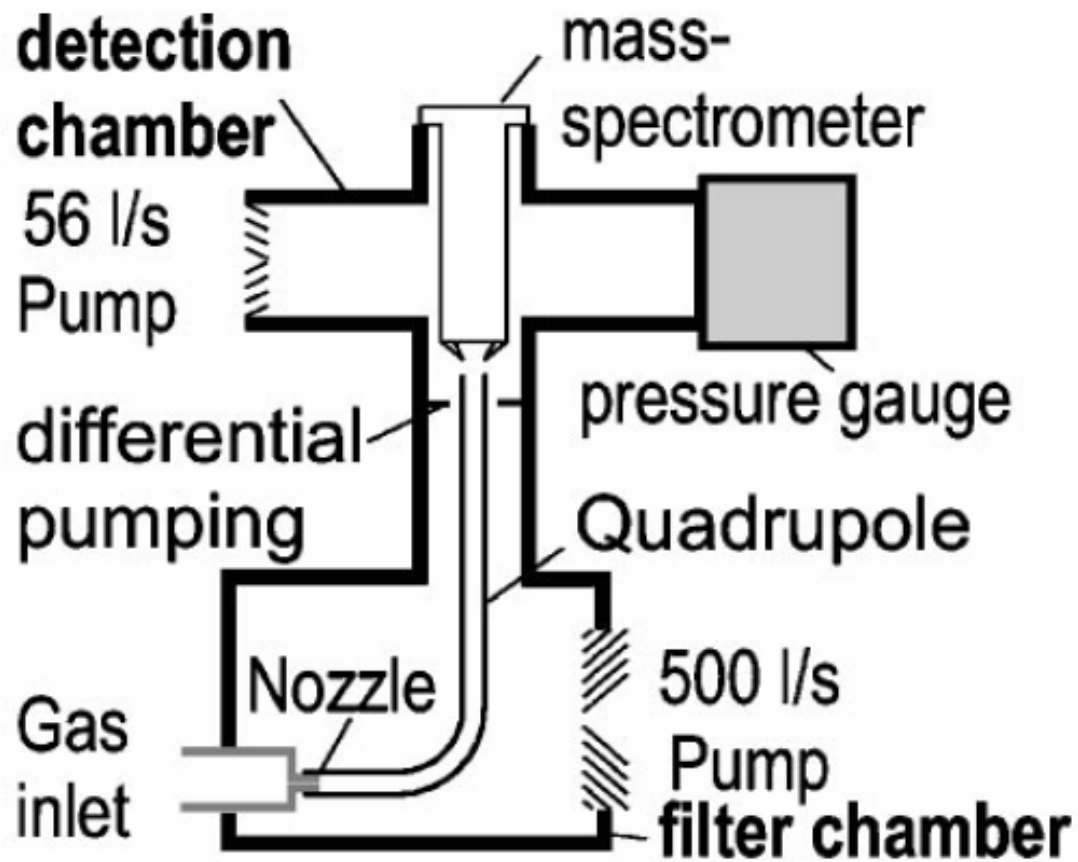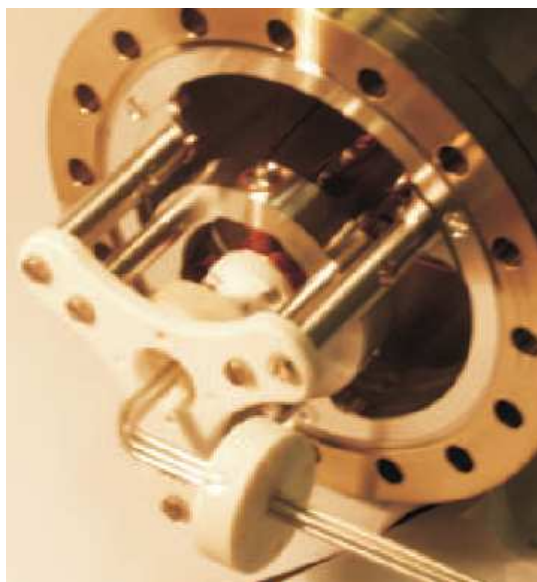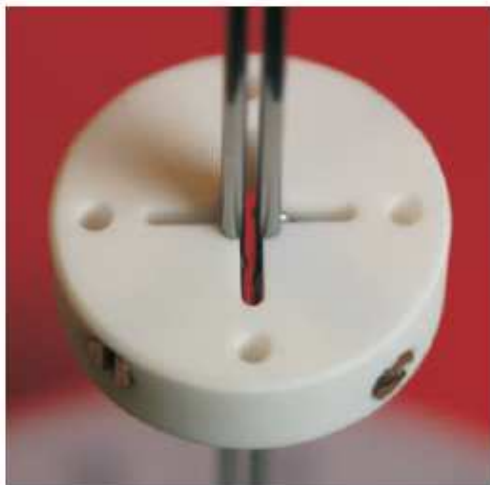
Results with CH$_2$O; and What they Imply (I)
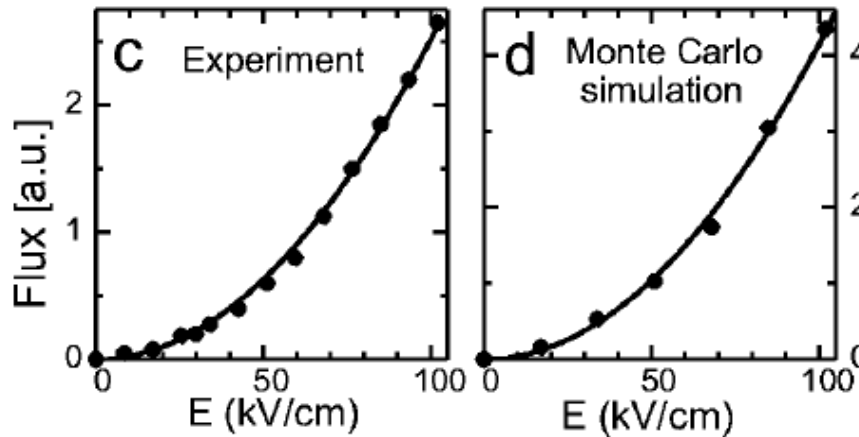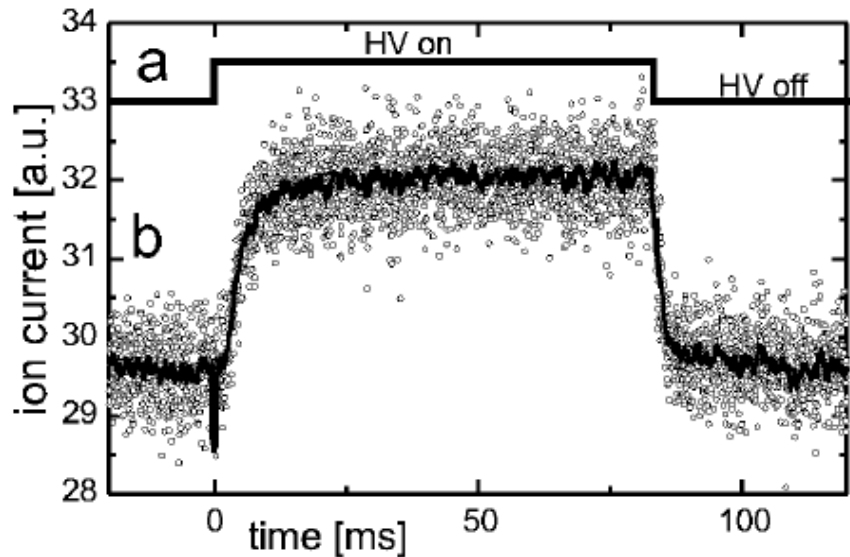
Velocity distribution in 1D

$$f(v)dv = \frac{1}{\sqrt{\pi}\alpha}\exp(-\frac{v^2}{\alpha^2})dv$$

Velocity distribution through a hole

$$f(v_z)dv = \frac{2}{\sqrt{\pi}\alpha^2}v_z\exp(-\frac{v_z^2}{\alpha^2})dv_z$$

$$\alpha = \sqrt{\frac{2k_BT}{m}} >> v_x, v_y, v_z ; v_z > v_x, v_y$$

Therefore, we get...

$$\Phi \propto \int_0^{v_{x\,max}}dv_x \int_0^{v_{y\,max}}dv_y \int_0^{v_{z\,max}}v_z dv_z$$

$$\Phi \propto v_x v_y v_z^2 \propto KE^2$$

Linear Stark Shifts =>

$$KE \propto StarkEnergy \propto HV$$

$$\Phi \propto HV^2$$

Results with CH$_2$O; and What they Imply (II)
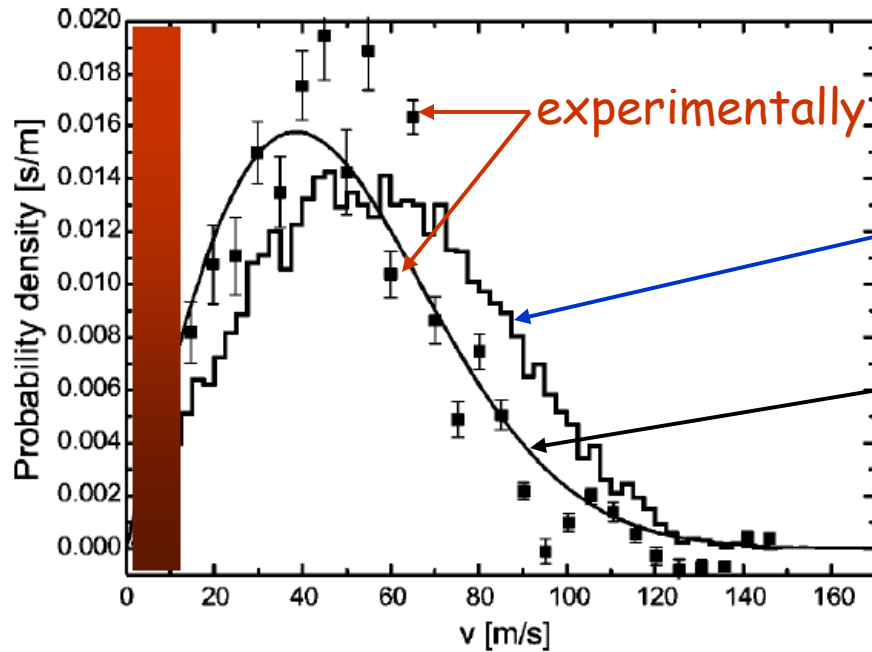
experimentally derived velocity distribution

Monte Carlo simulations

$$f(v_z)dv = \frac{2}{\sqrt{\pi}\alpha^2} v_z \exp(-\frac{v_z^2}{\alpha^2})dv_z$$

$$\alpha = \sqrt{\frac{2k_B T}{m}} >> v_x, v_y, v_z ; v_z > v_x, v_y$$

Molecular flow regime

maximum flux

Flux = 10^9 s^{-1}

Peak density in guide $\approx 10^8$ cm^{-3}

Longitudinal temp. = 5.4 K

Transverse temp. = 0.5 K
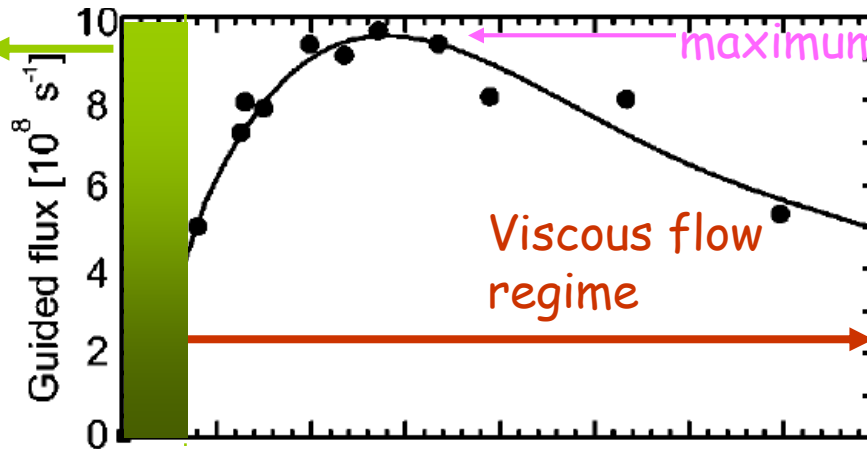
Viscous flow regime

Water (D₂O)

Dipole moment = 1.87 Debye

Rotational Constants :
A = 15.4 cm⁻¹
B = 7.3 cm⁻¹
C = 4.9 cm⁻¹

⇒ D₂O is an *asymmetric top*
   molecule
⇒ Dipole is along the "unstable"
   B axis
⇒ Lack of rotational degeneracy
⇒ In fact there are large
   separations in rot. levels
⇒ Quadratic Stark Shifts
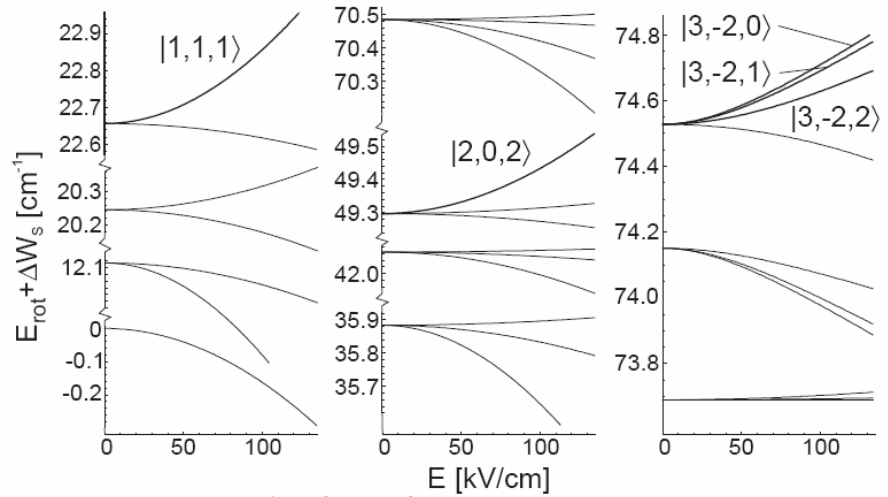
Stark shifts for D₂O
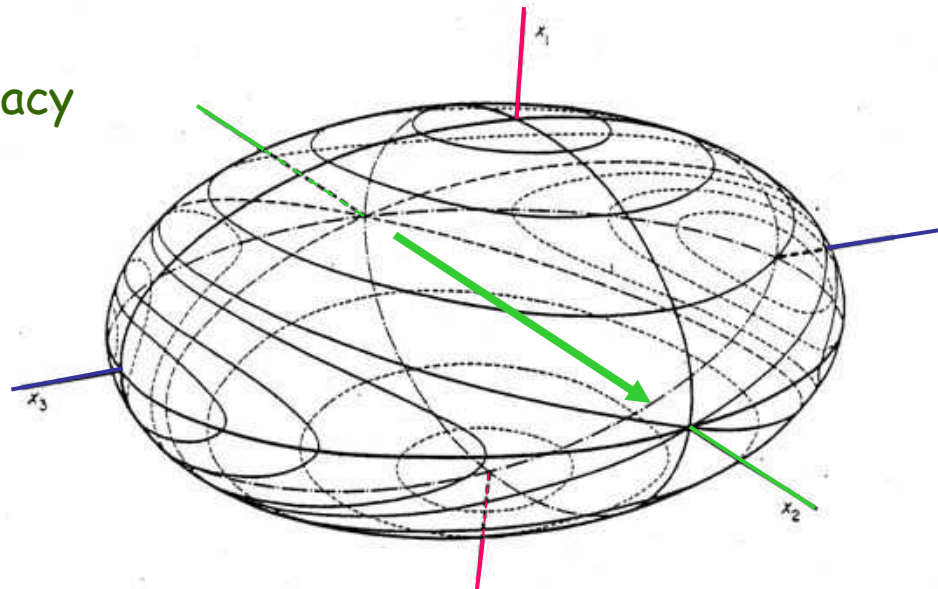
Experimental results (D_2O)
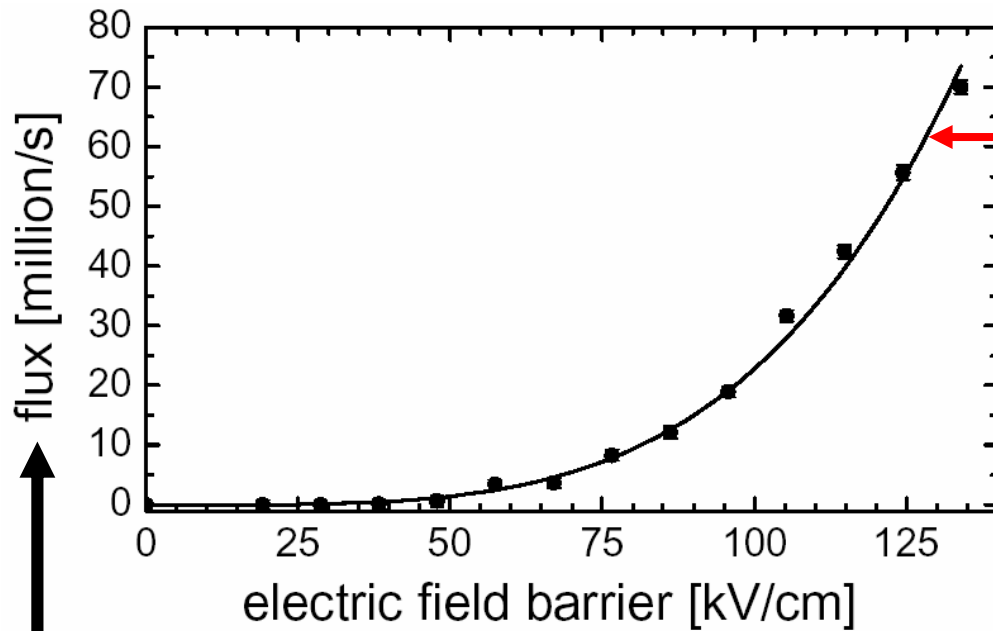
Quartic rise in flux as a func. Of appl. E field.

$$f(v_z)dv = \frac{2}{\sqrt{\pi\alpha^2}} v_z \exp(-\frac{v_z^2}{\alpha^2})dv_z$$

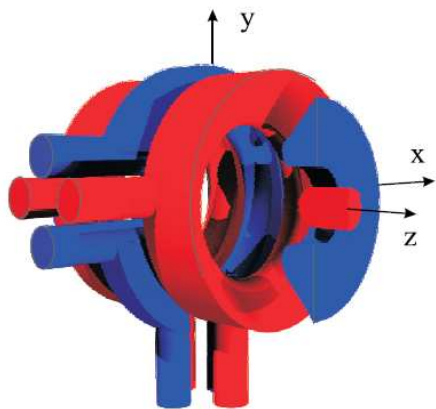$$\alpha = \sqrt{\frac{2k_B T}{m}} >> v_x, v_y, v_z; v_z > v_x, v_y$$

$$\Phi \propto \int_0^{v_{x\,max}} dv_x \int_0^{v_{y\,max}} dv_y \int_0^{v_{z\,max}} v_z dv_z \Rightarrow \Phi \propto v_x v_y v_z^2 \propto KE^2$$

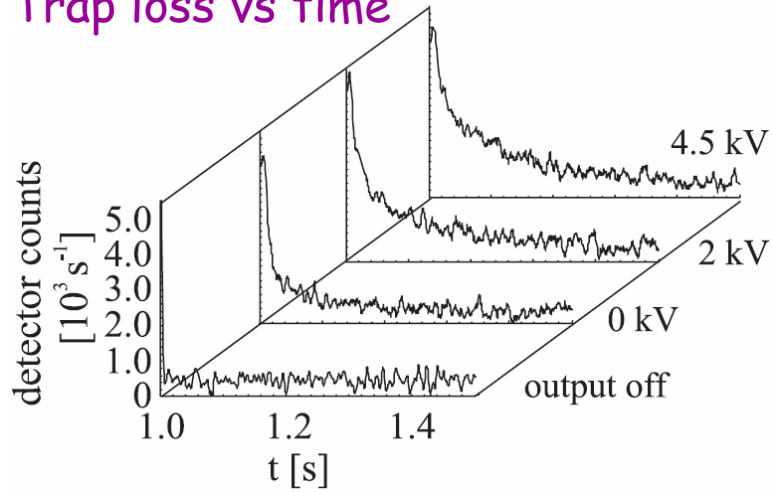Quad Stark Shifts => $KE \propto (W_s) \propto HV^2$

$$\Rightarrow \Phi \propto HV^4$$

Trap: Low Field Seeking States

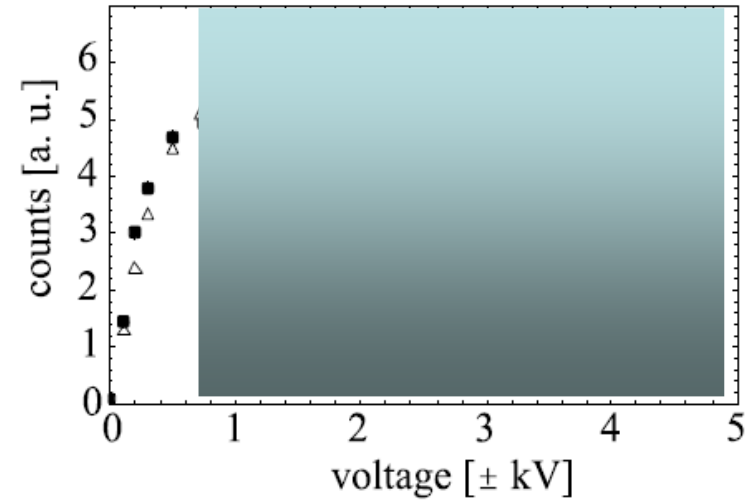To exploit the cold molecules created in the beam, we need to be able to trap them, for long interrogation.
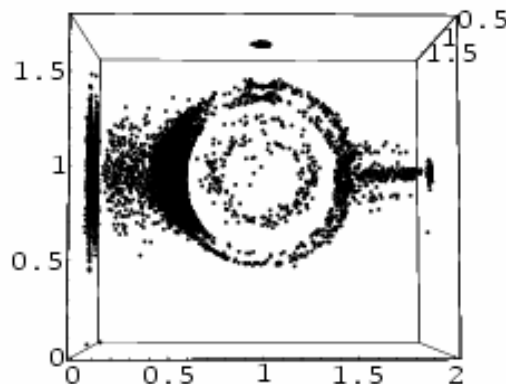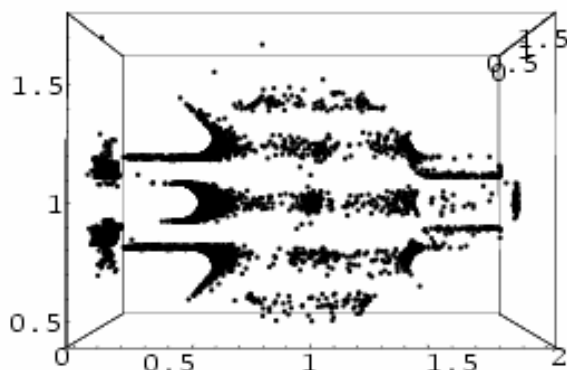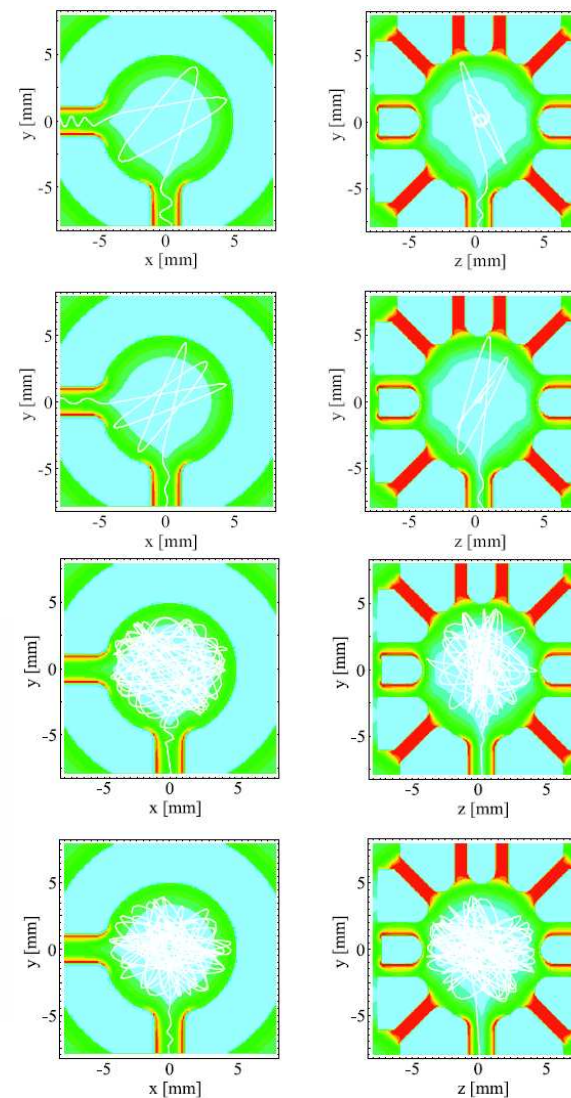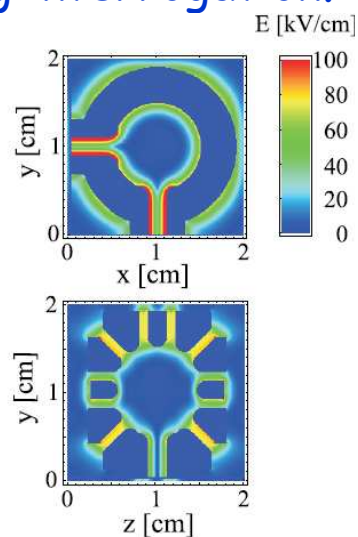
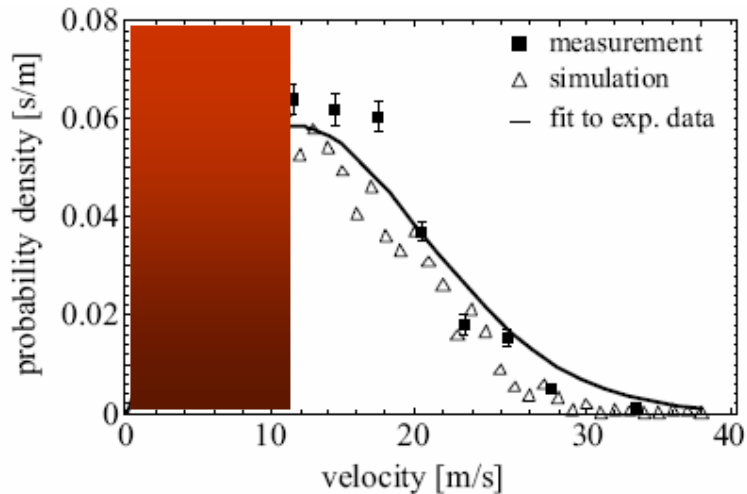# Results: Low Field Seeking States Trap
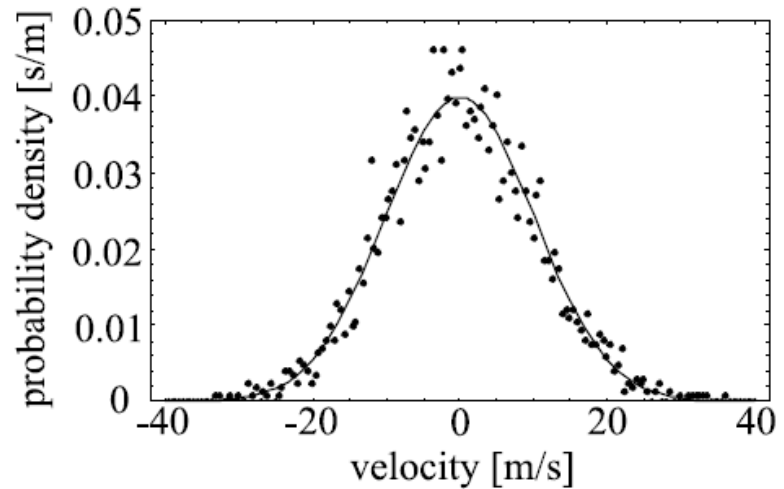
Trap loss vs time

Flux vs trap output guide voltage

Longitidunal velocity distribution of molecules from the trap

Transverse vel. distrib. in guide

Phys. Rev. Lett. **95**, 173002 (2005)

Combining Buffer Gas with E Guides

ionization volume of QMS

UV laser beam

electric guide 2

warm molecular gas line (•)   helium buffer-gas line (•)

5K shield

electric guide 1

Kapton foil

bend

buffer-gas cell at 5K

cell exit

adsorption pump

I_{cell}
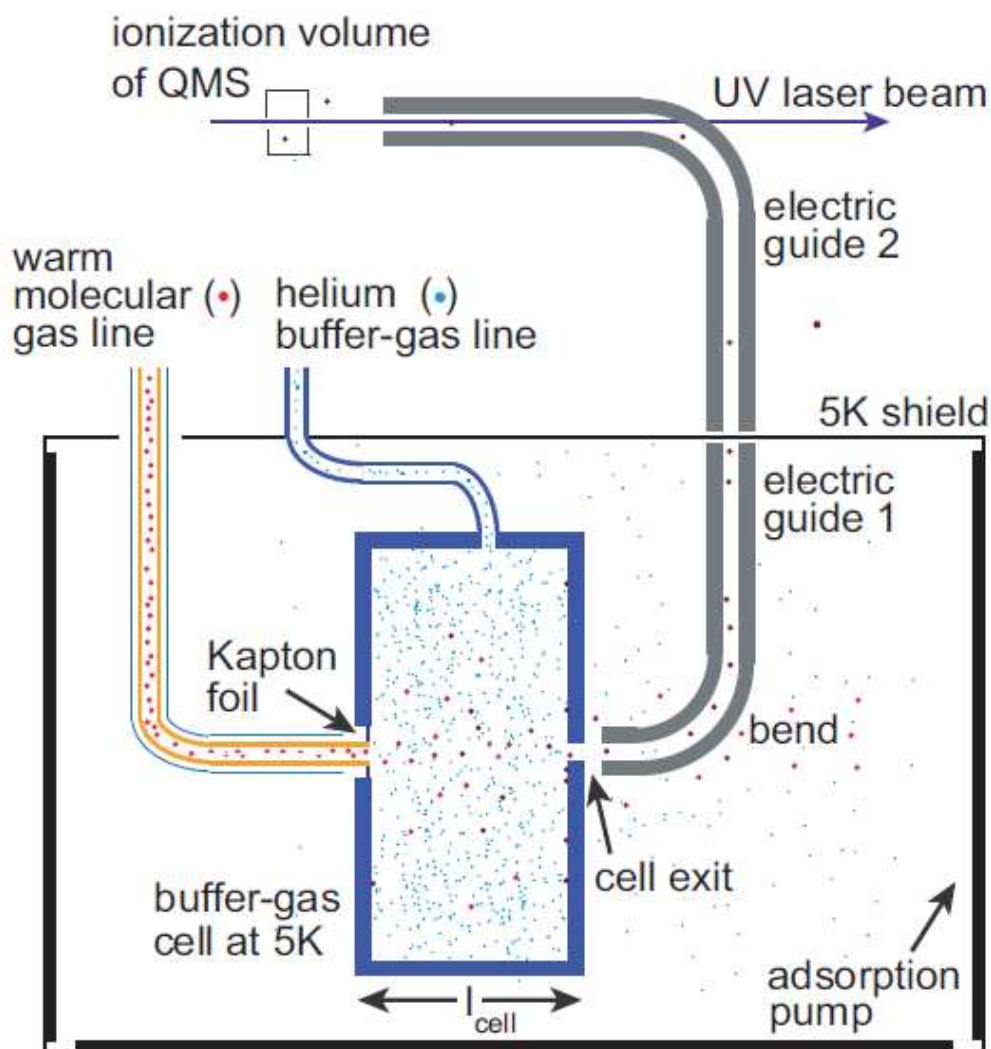
fluxes up to $(7\pm^{7}_{4}) \times 10^{10}$ molecules/s

Peak density
$$(1.0\pm^{1.0}_{0.6}) \times 10^{9} \text{ molecules/cm}^{3}$$

Need to guide with switching fields

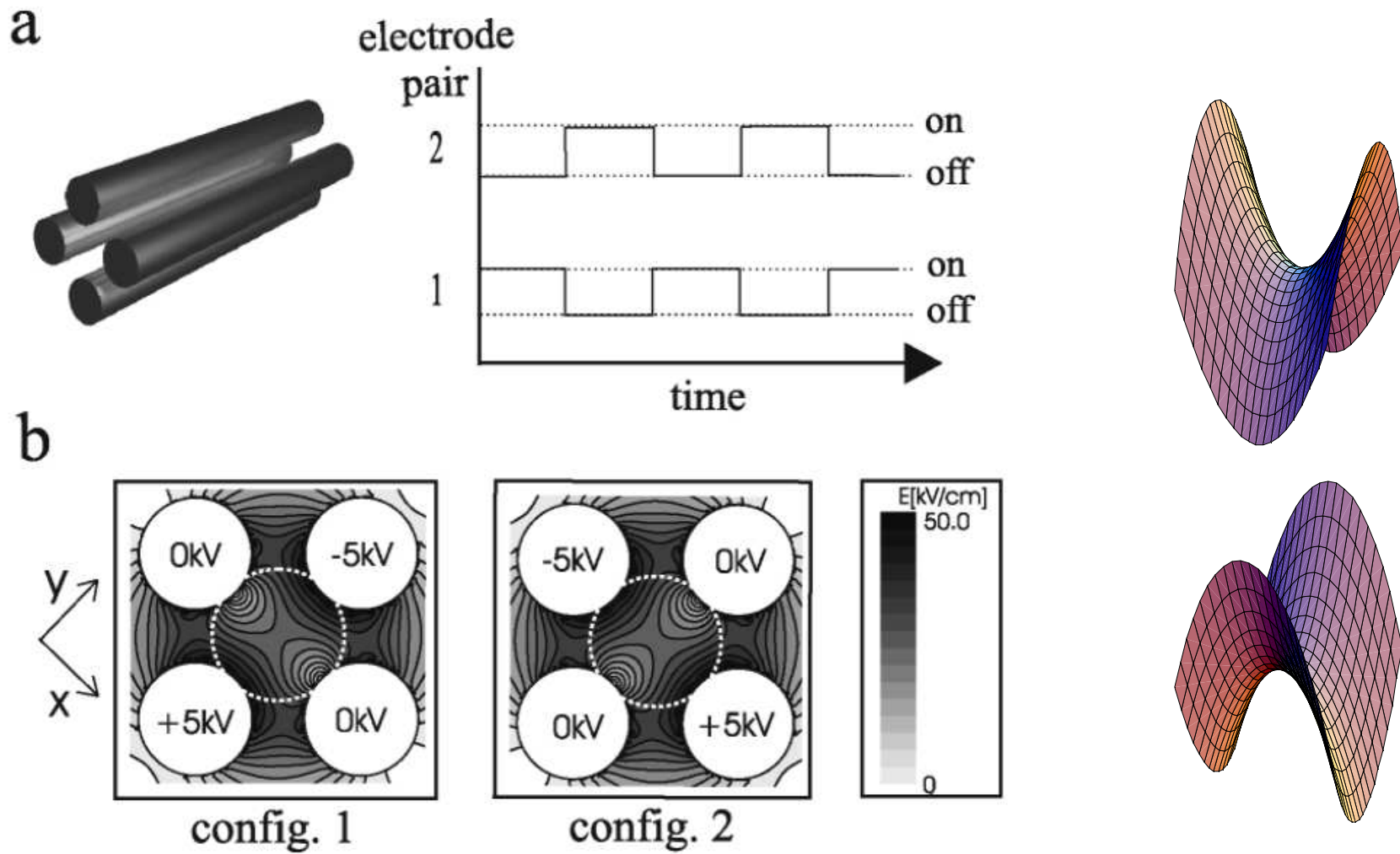Stark shift of the molecular ground state is always high field seeking

first order perturbation = 0

$$qE\langle e_0, v_0, J_0 \mid z \mid e_0, v_0, J_0 \rangle = 0$$

second order perturbation = -k E², k>=0

$$(qE)^2 \sum_{\forall i,j,k \neq 0} \frac{\left| \langle e_0, v_0, J_0 \mid z \mid e_i, v_j, J_k \rangle \right|^2}{E_{0,0,0} - E_{i,j,k}},$$

$$E_{0,0,0} - E_{i,j,k} < 0, \forall i, j, k \neq 0$$

Combined Cold Dipolar Beam: Low & High Field Seeking
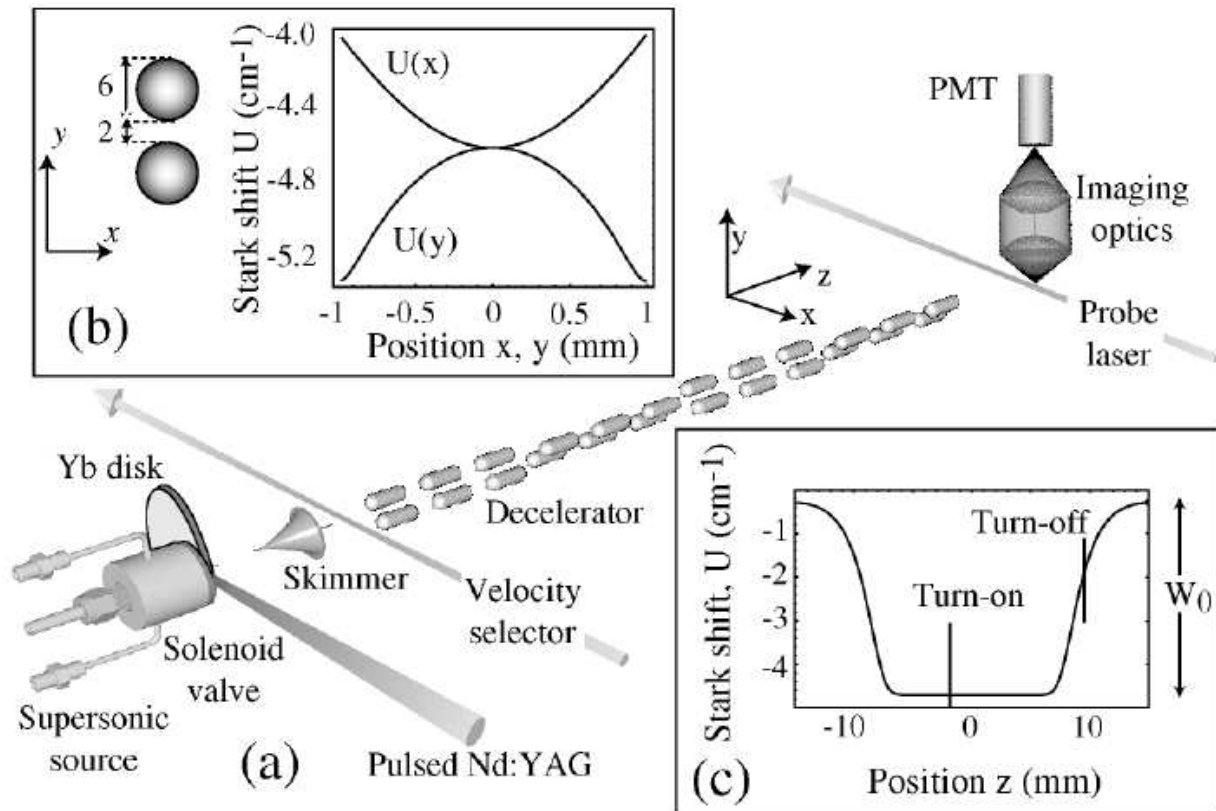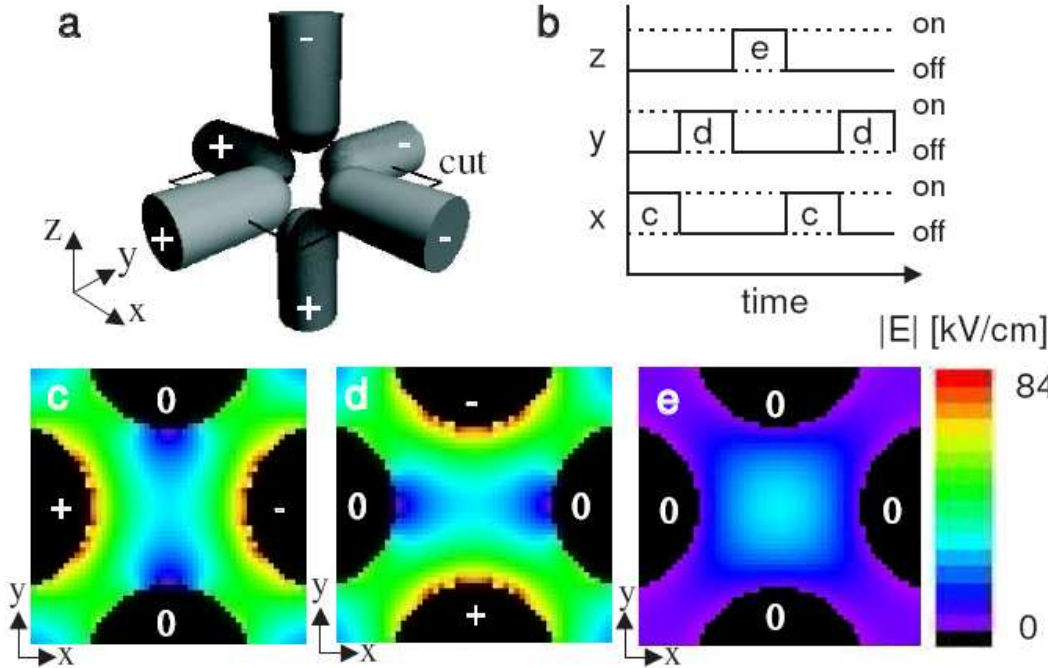
High Field Seeker Deceleration

FIG. 1. (a) The beam line. (b) Left: end view of one decelerator stage. Graph: Stark shift of ground state YbF within the stage versus x and y for electrode voltages of $\pm 10\,\text{kV}$. (c) Same Stark shift versus z, plotted for one stage.

The 3-phase Trap for Atoms
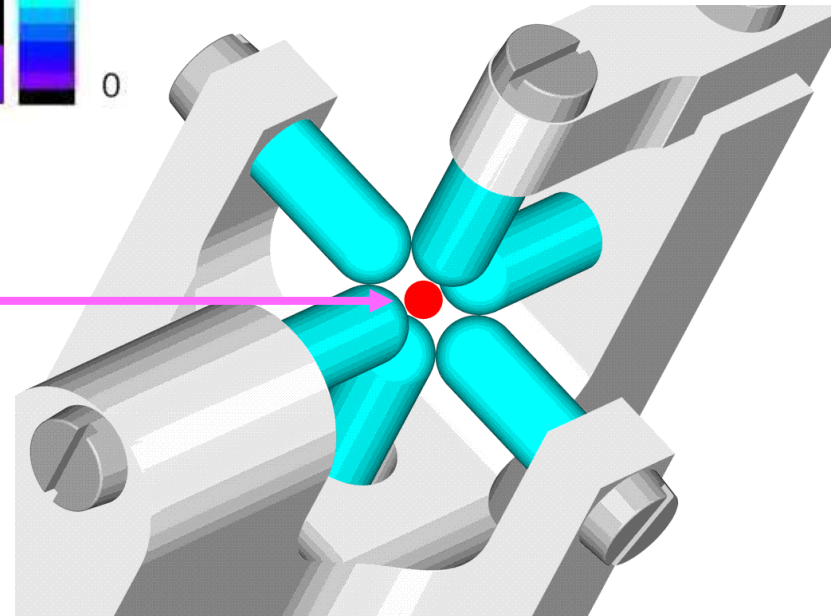

Atomic Species: Rubidium (Rb)

Atoms are High Field Seekers

Stark shift: atoms <<< molecules

Trap for atoms works for mol.

MOT… molasses…
optical pumping…
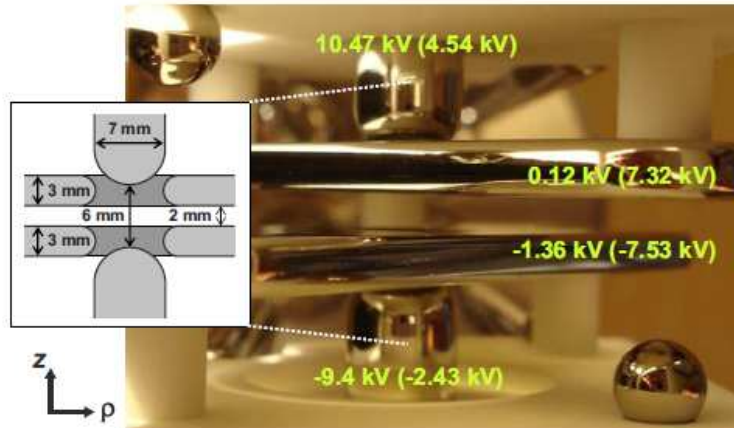magnetic trap…transport
to E trap

Another AC trap design

FIG. 1. (Color online) Photograph of the ac trap. The inset on the left shows a schematic of the trap where the dimensions of the electrodes and the distances between them are indicated. The voltages applied to the electrodes during the ρ-focusing (z-focusing) phase are written on each electrode.

FIG. 2. (Color online) Calculated electric field (in kV/cm) in the trap for the ρ-focusing (a) and z-focusing (b) configurations.

FIG. 6. (Color online) Lifetime measurement of the ac trapped atom cloud. The experiment is performed at 60 Hz, and all the data points are single-shot measurements. The solid line is a double-exponential fit to the data points, while the dashed curves show each exponential individually.
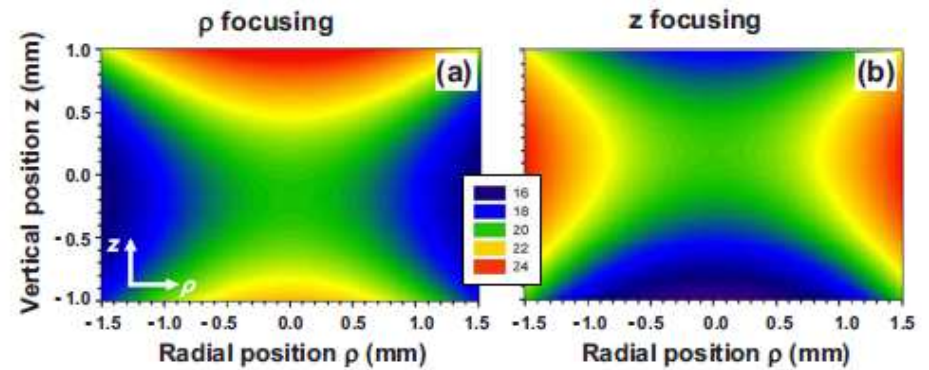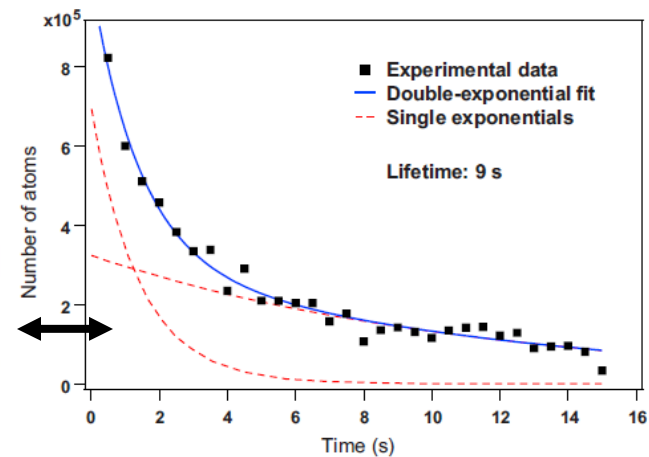
Kinematic Cooling using Inelastic Collisions

$$\mathbf{v}'_{NO} = \mathbf{v}_{cm} + \mathbf{u}'_{NO} \approx 0$$

As the molecules must be scattered in both the right direction (opposite to $\mathbf{v}_{cm}$) and with the correct speed, this cancellation occurs for only a small fraction of the molecules in the beam. Nevertheless, NO molecules with final velocities less than $15\,\mathrm{m\,s^{-1}}$ can be generated in a single quantum state at densities approaching 10^8 molecules $\mathrm{cm^{-3}}$ [176].
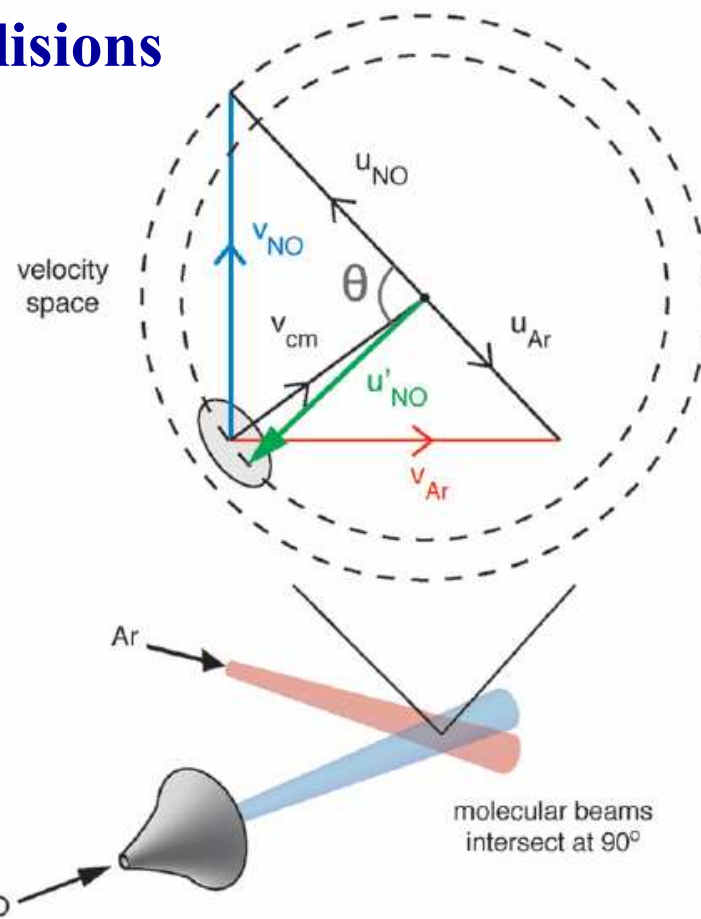
For beams intersecting at Right angles

$$\Delta E_{\mathrm{int}} = \left(1 - \frac{m_a}{m_b}\right) E_a$$

(c)
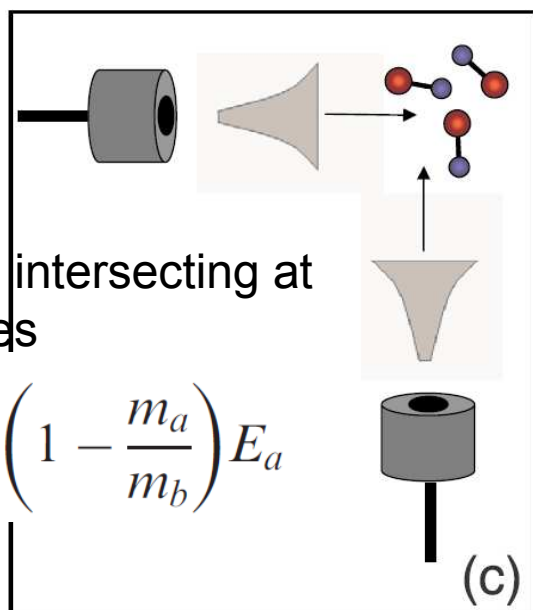
excess energy was taken up by rotation of the NO molecule through the inelastic transition NO ($^2\Pi_{1/2}$, $j = 1/2$) $\rightarrow$ NO ($^2\Pi_{1/2}$, $j' = 15/2$). Although most NO molecules are scattered into different quantum states, those remaining with very low velocities are produced in only a single rovibrational state.

Science **302**, 1940 (2003)

Rotating Nozzle: Harvard

Rotating nozzle

Slow Supersonic Beam

(b)
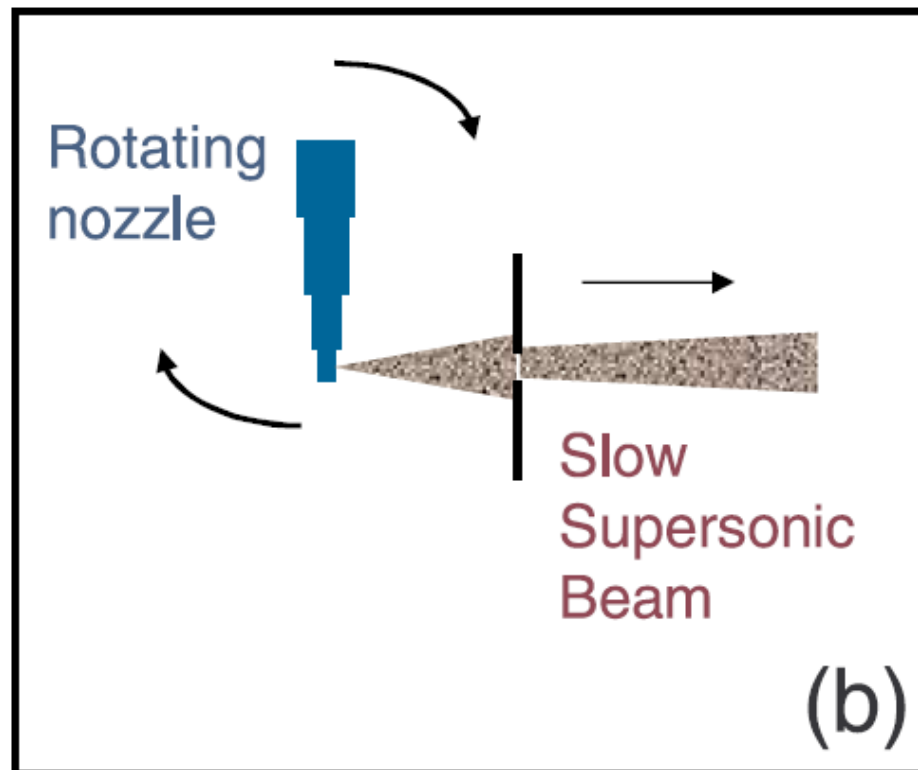
Contents

Table 1 Summary of experimental results for production of cold and ultracold polar molecules. Selected examples of the molecule species with its electric dipole moment (calculated or measured) and the achieved gas temperature, trapped number density and phase-space density are given

Method	Species (dipole/D)	T	Trapped density/cm^{-3}	PSD	Ref.
Buffer gas cooling	NH (1.39)	550 mK	10^8	10^{-14}	34
Stark deceleration	OH (1.67)	50 mK	10^6–10^7	10^{-13}	37 and 38
Photo-association (incoherent)	RbCs (1.3)	100 μK	10^4 (not trapped)	10^{-14}	52
	LiCs (5.5)	260 μK	10^3 (not trapped)	10^{-15}	56
Coherent population transfer starting from Feshbach molecules	KRb (0.566)	350 nK	10^{12}	0.02	13

Two excellent references

Taylor & Francis
Taylor & Francis Group

INVITED REVIEW ARTICLE

Ultracold molecules and ultracold chemistry

Martin T. Bell and Timothy P. Softley*

Department of Chemistry, University of Oxford, Chemistry Research Laboratory, Oxford, OX1 3TA, UK

Cold and ultracold molecules: science, technology and applications

Lincoln D Carr[1], David DeMille[2], Roman V Krems[3] and Jun Ye[4]

[1] Department of Physics, Colorado School of Mines, Golden, CO 80401, USA
[2] Department of Physics, Yale University, PO Box 208120, New Haven, CT 06520, USA
[3] Department of Chemistry, University of British Columbia, Vancouver, BC V6T 1Z1, Canada
[4] JILA, National Institute of Standards and Technology and University of Colorado, Department of Physics, University of Colorado, Boulder, CO 80309-0440, USA
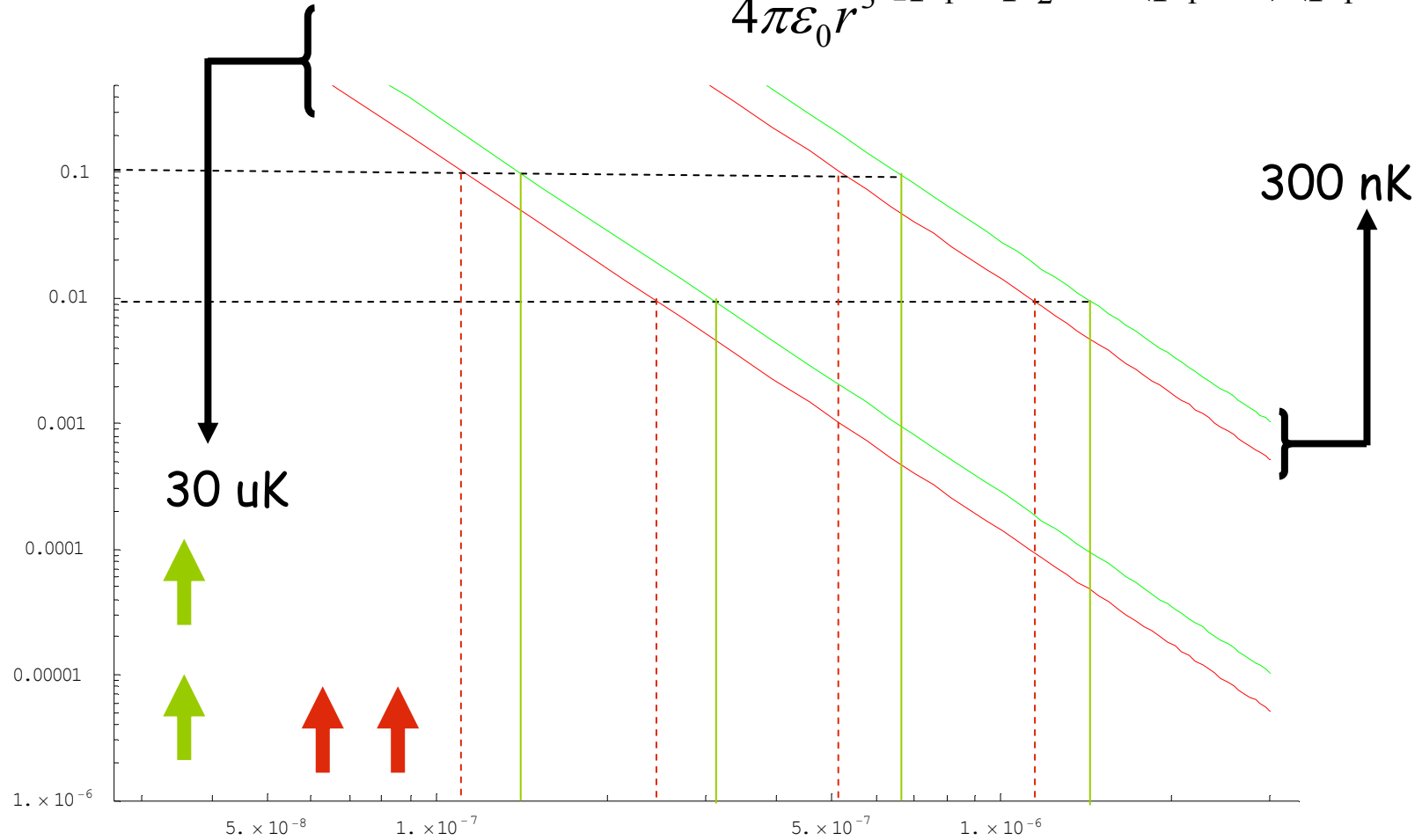
Contents

Contents

dipole-dipole interaction strength

$$U = \frac{1}{4\pi\varepsilon_0 r^3}[\vec{p}_1 \bullet \vec{p}_2 - 3(\vec{p}_1 \bullet \hat{r})(\vec{p}_1 \bullet \hat{r})]$$

300 nK

30 uK

Angular Momentum Couplings in Molecules
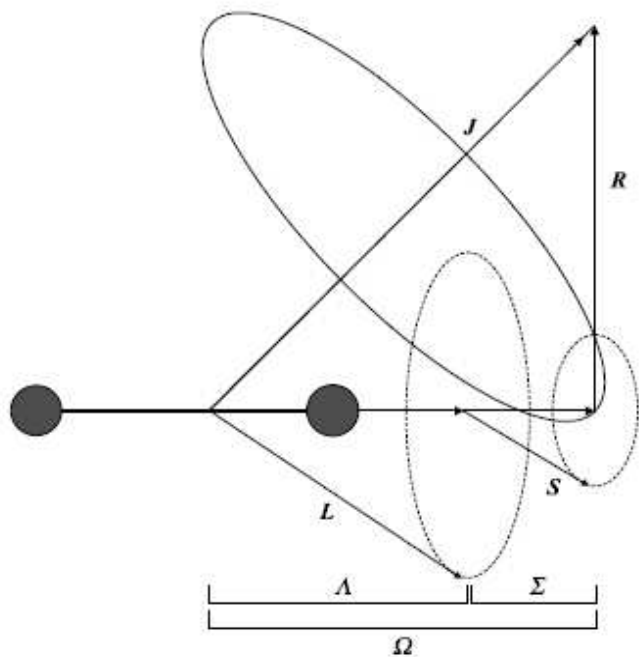
Vector coupling diagram for Hund's case (a).
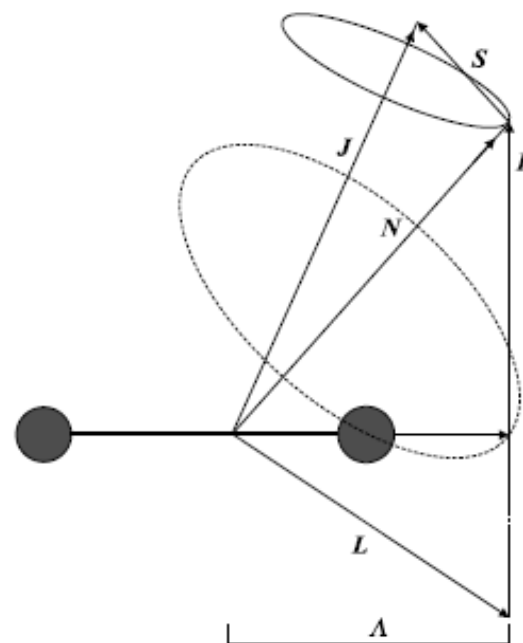
Vector coupling diagram for Hund's case (b).

Need to guide with switching fields

Stark shift of the molecular ground state is always high field seeking

first order perturbation = 0

$$qE\langle e_0, v_0, J_0 \mid z \mid e_0, v_0, J_0 \rangle = 0$$
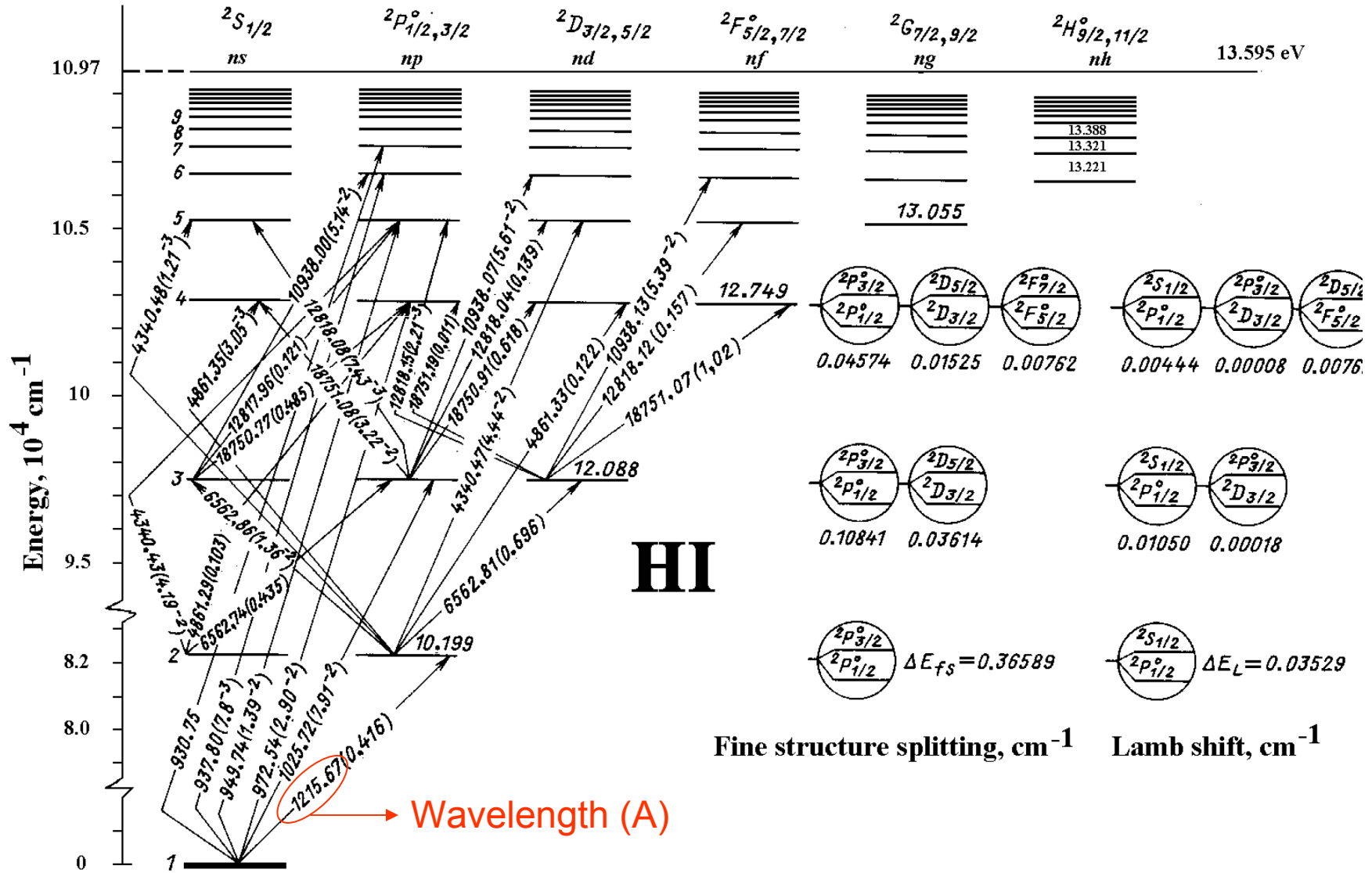
second order perturbation = -k E², k>=0

$$(qE)^2 \sum_{\forall i,j,k \neq 0} \frac{\left| \langle e_0, v_0, J_0 \mid z \mid e_i, v_j, J_k \rangle \right|^2}{E_{0,0,0} - E_{i,j,k}},$$

$$E_{0,0,0} - E_{i,j,k} < 0, \forall i, j, k \neq 0$$

Contents

Contents

Contents

Grotrian Diagram for the Hydrogen Atom

The organization of the material that follows

We first discuss some of the techniques used to produce ultracold molecules from ultracold atoms

We then go through a discussion of some techniques of how to go from hot molecules to cold molecules

We then try and assess where the experimental work is at the present with respect to the physics goals

We look at some problems that one could encounter along the way to the physics goals

Finally we discuss the consequences of achieving the physics goals

Contents